2010

Fast Parameter-Space Sweep of Wideband Electromagnetic Systems Using Bt-pod

Wei Wang
University of Massachusetts Amherst

FAST PARAMETER-SPACE SWEEP OF WIDEBAND ELECTROMAGNETIC SYSTEMS USING BT-POD

A Thesis Presented

by

WEI WANG

Submitted to the Graduate School of the
University of Massachusetts Amherst in partial fulfillment
of the requirements for the degree of

MASTER OF SCIENCE IN ELECTRICAL AND COMPUTER ENGINEERING

February 2010

Department of Electrical and Computer Engineering

FAST PARAMETER-SPACE SWEEP OF WIDEBAND ELECTROMAGNETIC SYSTEMS USING BT-POD

A Thesis Presented

by

WEI WANG

Approved as to style and content by:

Marinos N. Vouvakis, Chair

Daniel H. Schaubert, Member

Christopher V. Hollot, Member

Christopher V. Hollot, Department Chair
Department of Electrical and Computer Engineering

To my father and my mother.

ACKNOWLEDGMENTS

I have to start my acknowledgements with my advisor Prof. Marinos N. Vouvakis. I am grateful to him for his technical advice, encouragement, and support during my master program.

I would like to thank the members of the Antenna Propagation Laboratory at University of Massachusetts Amherst especially Georgios Paraschos who has made great help to me in this work. I would like to extend my thanks to Steven Holland, Seth Jackson, and Simon Tang for their help in my research.

Furthermore, I would like to thank my undergraduate thesis advisor, Prof. Zhong-Qing Zhang at Zhejiang University, China, for his support and introduced me into the computational electromagnetics area.

Thanks are extended to my friends especially Kan Fu, Zuo-Jing Chen and Jie Xu for their encouragement in study and help on my living in Amherst.

Last, but certainly not the least, I want to thank my father Jia-Pei Wang and my mother Hong-Yu Wei. I am so grateful to you for your constant support, patience, and love. Very special thanks should be extended to Zhen Zhao and Yu-Qi Qin, for their encouragement during my difficult times in the past.

ABSTRACT

FAST PARAMETER-SPACE SWEEP OF WIDEBAND ELECTROMAGNETIC SYSTEMS USING BT-POD

FEBRUARY 2010

WEI WANG

B.Sc, ZHEJIANG UNIVERSITY, P.R. CHINA, JUNE 2007

M.S.E.C.E., UNIVERSITY OF MASSACHUSETTS AMHERST

Directed by: Professor Marinos N. Vouvakis

Modeling and design of high frequency electronic systems such as antennas and microwave devices require the rigorous numerical solution of Maxwell's equations. The frequency-domain (time-harmonic) tangential vector finite element method (TVFEM) for Maxwell equations results in a second-order dynamical electromagnetic model that must be repeatedly solved for multiple frequencies, excitation or material parameters each design loop. This leads to extremely long design turnaround that often is not optimal. This work will propose an accurate, error controllable and efficient multi-parametric model order reduction scheme that significantly accelerate these parameters sweep. At the core of this work is the proper orthogonal decomposition (POD) sampling technique and balanced truncation (BT) algorithm that are used to reduce multi-parameter spaces that include frequency, material parameters and infinite array scan angles. The proposed methodology employs a novel computational scheme based on adaptive POD sampling and the singular value decomposition

(SVD) of the low-rank Hankel matrix. Numerical examples confirm the significant time savings and good accuracy of the method for a diverse set of high-frequency electromagnetic systems.

TABLE OF CONTENTS

LIST OF TABLES

Table **Page**

LIST OF FIGURES

Figure **Page**

NOMENCLATURE

P	Total number of EM waveports
Ω	Finite element truncated computational domain
ϵ_r	Material relative permittivity
$\hat{\mathbf{n}}$	Outward unit normal vector
μ_r	Material relative permeability
k_o	Freespace wave number
s	Laplace frequency
N	Finite element full model size
$\mathbf{A}$	LTI system linear maps
$\mathbf{C}$	Matrix map from electric field to output
$\mathbf{D}$	Finite element damping matrix
$\mathbf{E}$	Electric field
$\mathbf{M}$	Finite element mass matrix
$\mathbf{S}$	Finite element stiffness matrix
$\mathbf{e}$	Electric field unknown vector
$\mathbf{y}$	Finite element system output
$\tilde{\mathbf{S}}, \tilde{\mathbf{D}}, \tilde{\mathbf{M}}, \tilde{\mathbf{C}}$	Reduced FE matrices
n	Reduced model size
$\mathbf{H}$	Transfer function of linear system
$\mathbf{H}_a$	Transfer function of adjoint form of linear system
$\boldsymbol{\mathcal{P}}$	System reachability gramian
$\boldsymbol{\mathcal{Q}}$	System observability gramian

$\tilde{\boldsymbol{\mathcal{P}}}$	Approximated system reachability gramian
$\tilde{\boldsymbol{\mathcal{Q}}}$	Approximated system observability gramian
$\mathbf{L}$	Low-rank Choleski factor of observability gramian
$\mathbf{U}$	Low-rank Choleski factor of reachability gramian
$\mathbf{V}$	Right singular vectors of Hankel matrix
$\mathbf{W}$	Left singular vectors of Hankel matrix
$\boldsymbol{\Sigma}$	Singular values of Hankel matrix
$\boldsymbol{\mathcal{H}}$	Hankel matrix
$\mathbf{T}_L$	Left transformation matrix
$\mathbf{T}_R$	Right transformation matrix
ε	Truncation tolerance of Hankel singular values
tol_E	Global error estimate tolerance
tol_s	Iterative solution tolerance
E	Global residual error estimate
K	Number of POD sampling points
M	Number of sweep points
e	Local residual error estimate

CHAPTER 1

INTRODUCTION

1.1 Overview

This thesis work proposes a computational algorithm for the fast and error controllable *parameter-space* sweep for electromagnetic (EM) devices and systems. In the context of this work, the parameter-space consists of the operating frequency, material properties, and the scanning direction of an infinite antenna array. The fast parameter-space sweep is achieved via the model order reduction (MOR) paradigm, namely, the original computational model is approximated and replaced by a much smaller one (reduced model) that retains the dominant behavior of the original system. The fast parameter sweep is then achieved by repeatedly solving the reduced problem. At the core of this work is the proposed balanced truncation and proper orthogonal decomposition (BT-POD) algorithm. In this thesis, BT-POD has been used in conjunction with the tangential vector finite element method (TVFEM), to study the behavior of various EM systems such as antennas and microwave devices.

1.2 Motivation

Full-wave computational electromagnetics (CEM) methods such as the tangential vector finite element method have revolutionized the design and optimization of microwave devices, antennas and RF integrated circuits (RFICs). Instead of prototyping using textbook approximate theories, or "rules of thumb", modern high-frequency electronics design uses CEM algorithms for virtual prototyping. Such design cycles

usually consist of repeatedly updating and solving a parameterized model of the device or system, to find fields and other engineering figures-of-merit that meet desired specifications. Since the accuracy of CEM methods such as the finite element method (FEM) mostly relies on the three-dimensional meshing of the model, highly accurate modes result in system of equations with very high degrees of freedom (DoF), that requires miniutes or hours for each solve. Given that a typical design process could require hundreds or thousands of such solutions to the variation of various input parameters, the importance of a fast parameters sweep algorithm for CEM is paramount.

The proposed algorithmic developments will impact the design of antenna, RF and microwave system since they provide design tools that can help engineers design faster, and better devices or systems. Specifically, this work will impact the design of EM systems through:

- Fast frequency sweep of ultra-wide band systems.
- Fast parameters sweep and optimization of antenna scanning angles and material properties.

1.3 Review of Previous Work

The model order reduction paradigm was first proposed in the control community [1], [2], and since then has found many applications in areas such as structural engineering [3], [4], computational fluid dynamics (CFD) [5], [6], IC interconnect modeling [7], [8] and electromagnetics simulation [9], [10]. In general, the MOR techniques aim to present a compact computational model with significantly reduced DoF representation that retains the essential dynamic behavior of the original full order model.

Much of the theoretical developments in MOR have come from control [1] and applied mathematics community. The truncated balanced realization (TBR) of Moore [11] was among the first MOR method that provided an accurate low-order approxi-

mation of the state-space system. Later, Glover in [12] extended the work of Moore by introducing MOR based on the Hankel operator with rigorous error bounds. The proper orthogonal decomposition (POD) method [13], also known as Principal Component Analysis (PCA) [14] or Karhunen-Loeve (K-L) expansions [15], aims to obtain low-dimensional approximation of the full-order model and has been used by various engineering applications such as turbulence analysis [16] and structural vibrations [17]. For general references in MOR, the interested readers are encouraged to refer to several monographs [18], [19] and journal special issues [20], [21] devoted to this area.

Among all MOR methods, there are two broad categories: (1) Krylov based MOR, and (2) singular value decomposition (SVD) based MOR. The following sections review the work in these two categories.

1.3.1 Krylov-based MOR

An early development on model reduction of model based parameter estimation was the asymptotic waveform evaluation (AWE) algorithm of Pillage and Rohrer [22]. The AWE algorithm generates a Pade approximation of the output quantity through the explicit moment-matching of the transfer function. Although surprisingly successful, an efficient AWE lacks robustness due to poor conditioning of the Grahm matrix. In 1995, Freund and Feldmann [23] proposed the Pade via Lanczos (PVL) algorithm which altogether elliminates the explicit moment-matching of AWE by using the two-sided Lanczos algorithm [24]. PVL requires approximately similar computational cost as AWE but is more robust and leads to more broadband reduced models. Both PVL and AWE can produce non-passive reduced models. When the reduced model is used to co-simulate hybrid EM/active circuits systems, the non-passivity of the EM reduced model can lead to overall instabilities. To preserve the passivity of the reduced model, Odabasioglu and Celik proposed the PRIMA algorithm [7] which employs the Arnoldi process [25] to generate orthogonal basis for Krylov space.

Elfadel and Ling later extended the Arnoldi algorithm to multipoint passive model order reduction using rational Krylov subspace basis [26], where multiple frequency expansion points are used for the reduction thus leading to reduced models with wider frequency response. The Krylov MOR has been also extended to second-order dynamical system that is encountered in physical systems with loss or gain. Su et al. [27] applied Krylov vectors and parameter matching to analyze second-order damped structural dyanmical system, and Bai et al. [28] introduced a second-order Arnoldi method to solve quadratic eigenvalue problems.

Kyrlov MOR methods are numerically efficient, easy to integrate with various computational kernels such as finite difference method (FDM), boundary element method (BEM), FEM, etc. However, Krylov MOR methods have several drawbacks: (1) They do not have rigorous error bounds and estimation have been proven difficult or impossible to establish [19], (2) They are numercal unstable due to the break-down of the inherent Krylov subspace orthogonalization process, and (3) They are difficult to parallelize due to the global communication required for the orthogonalization process.

1.3.2 SVD-based MOR

SVD-based MOR has attracted the recent interests of researchers in applied mathematics, IC and structural dynamic community. The majority of the published work is based on the early development of Moore's work on truncated balanced realization (TBR) [11]. Although the TBR algorithm provides a solid theoretical foundation for SVD MOR that is based on the reachability and observability gramians resulting from the solution of the Lyapunov eqautions [19], the numerical computation of the approach is impossible for large-scale systems. Thus significant computational research has been devoted to developing numerically efficient SVD MOR methods for large-scale systems. Penzl in [29] was among the first to tackle this problem through

a cyclic low-rank Smith method. Penzl's method seeks the approximation of the low-rank system gramians resulting from large sparse Lyapunov equations. In aeronautics, Willcox and Peraire [30] proposed to combine the POD algorithm [16] with the concept of balancing realization [19] to obtain a low-rank approximation of system gramians. Li and White [31] presented the Cholesky factors-alternating direction implicit (CF-ADI) to approximate solution of Lyapunov equations. Phillips and Silveira proposed Poor Man's TBR [32] for IC interconnect systems, which approximates the frequency domain system gramians by a small set of frequency domain solutions of the system. Recently, Losse and Mehrmann [33] proposed to analyze system gramians conditions for second-order model.

In general, the central idea behind the SVD-based MOR is to seek a balanced reduction representation of the orignal system through the SVD of system gramians which requires the solution of Lyapunov equation. The exact SVD MOR methods are robust, have explicit error bounds and estimation and result to stable reduced system with minimal DoFs, but are numerically inefficient. The major challenge ahead is to develop SVD MOR methods that use approximate gramian computations, but lead to robust, optimal and stable reduced systems.

1.3.3 Full-wave Electromagnetic Analysis via MOR

In CEM community, much of the MOR work relies on the Krylov-based methods because of their numerical efficiency for very large-scale models (A typical EM model requires more than 10 thousand DoFs). Miller proposed model based parameter estimation (MBPE) [34, 35, 36] by using fitting models obtained from first-principle models or measured data. Cockrell and Beck [37] used the AWE technique to analyze frequency-domain EM problems using Method of Moments for radar cross section (RCS) applications. Slone et al. [38] proposed a multipoint Galerkin AWE (MGAWE) technique to simulate wideband EM systems, and later the well-conditioned AWE

(WCAWE) scheme [39] to overcome the ill-conditioning problems of AWE. Weile and Michielssen used generalized versions of single expansion point Krylov subspace termed rational Krylov MOR to analyze frequency selective surfaces [40]. Wu and Cangellaris applied the Krylov MOR to solve for the scattering parameters of microwave circuits [41]. It should be remarked that in constrast to the multipoint expansion strategy employed in [38], Weile et al. and Wu et al. applied the single point expansion Krylov MOR. The adavantage of this technique is the FE matrix needs to be factorized only once and all Krylov vectors are generated by forward-backward substitution. However, in most cases the optimal expansion location is a priori unknown. On the other hand, the multipoint expansion strategy offers flexibility in selecting expansion frequencies and therefore a better quality reduced model can be obtained to capture the system spectral response.

To mitigate the lack of error control of Krylov MOR methods [19], many researchers proposed the use of adaptive frequency sampling strategies in conjunction with rational multipoint Krylov MOR. Such methods do not require apriori knowledge of the expansion points used for the Krylov subspace, leading to broader bandwidth reduced systems, and have better error control. A early version of adaptive frequency sampling algorithm was developed in [42] where a rational fitting method to evaluate the system response with minimal samples. Recently, Schultschik et al. [43] proposed an adaptive multi-point fast frequency sweep technique based on Krylov subspace method.

Researchers in EM have used MOR to reduce systems for fast frequency sweep (single-parameter MOR), but also multi-parameter sweep that involve material properties. Weile and Michielssen proposed a generalized Krylov MOR method for two-paramete linear system [44]. In [45], they utilized the proposed method in [44] to analyze Frequency-Selective Surface (FSS) with parameters of frequency and incident

angle. Recently, Farle et al. applied a multi-dimensional Krylov MOR to perform fast sweep based on frequency and material properties [46].

1.4 Summary of Contributions

It will be beneficial to state the main contributions of this work and provide a clear distinction with previously published work.

The majority of the this research focuses on SVD based model reduction for fast frequency sweep of frequency domain models arising from FEM discretization. To the best of our knowledge, it is the first time in the CEM community to introduce the SVD based MOR technique for EM simulations of large-scale wideband devices and systems. The proposed BT-POD MOR method shares a similar flavor with low-rank POD of Willcox [30] and poor man's TBR method [32] since low-rank gramian representations are generated. However, unlike these methods that form the balancing transformations through eigenvalue decomposition or SVD of the POD snapshots, the present method forms the low-rank Hankel matrix from the POD snapshots, which is significantly smaller in size, therefore the balancing transformations are computed considerably more efficient.

This work is the first to use a multi-dimensional model reduction for infinite array problems in electromagnetics, and according to the author's knowledge, the first to extend SVD based methods to multi-parameter reduction.

Last but not least, the adaptive frequency sampling strategy proposed in this work differs from all the adaptive methods summarized in section 1.3.3. In contrast to finding error in each adaptive step based on interpolated scattering parameter [42] or error at every sweep point [43], the adaptive BT-POD uses goal-oriented indicators that are based on the error evaluation of recovered fields on the device ports, leading to a efficient process of seeking minimal number and optimal locations of the parameter samples.

1.5 Thesis Outline

This thesis is organized as follows. In chapter 2, we will summarize the frequency domain TVFEM model used for the model reduction and describe the theory and algorithic developments behind the BT-POD. Numerical results will demonstrate the validity and efficiency of the proposed methodology. In chapter 3, the BT-POD algorithm is extended to multiple parameters. The work is limited to frequency and material parameters and scan angles of infinite array TVFEM models. The BT-POD algorithm is extended via an adaptive POD sampling strategy proposed in chapter 4, and a microwave waveguide filter problem is shown to verify the algorithm.

CHAPTER 2

FAST FREQUENCY SWEEP WITH BALANCED TRUNCATION - PROPER ORTHOGONAL DECOMPOSITION

This chapter presents a frequency-domain model-order reduction scheme using the balanced truncation and proper orthogonal decomposition (BT-POD) for first-order dynamical systems resulting from tangential vector finite element method (TVFEM) [47]. Even though the theoretical developments assume first order or loss-less second order dynamical systems, the method is applicable to general second order systems arising from the TVFEM models of general EM systems. The proposed model reduction technique is capable of modeling wideband EM systems, which is considerably more challenging than that of narrowband or multiband systems, due to the large information capacity of the wideband systems. The proposed model reduction technique seeks the approximate (low-rank) reachability and observability gramian of the system through the POD sampling in frequency domain. The present approximation is equivalent to approximating the gramian computation by a numerical quadrature, over the frequency bandwidth of interest. This approach shares the similar flavor with method of snapshot POD [30] and Poor Man's TBR [32] since all methods seek for a balancing transformation through sampling in the frequency domain. However, the proposed method offers a significant computational adavantage because it attempts to generate the balancing transformation through the SVD of the low-rank Hankel matrix [19], instead of explicitly performing the eigenvalue decomposition (EVD) of the two gramians. Following such approach, the balanced transformation matrices are used in a Petrov-Galerkin (oblique) projection scheme to reduce the original sys-

tem. The numerical examples in this section include three different EM systems, a band-pass microstrip filter, a broadband BAVA antenna element and an infinite Vivaldi array. Through the careful analysis of these examples, various results are presented that validate the proposed method and demonstrate its numerical efficiency and accuracy.

2.1 Boundary Value Problem

The goal is to model the dynamical (frequency) behavior of broadband electromagnetic systems by using the time-harmonic (frequency-domain) TVFEM. Figure 2.1 shows such a general system where various materials, excitation and boundary conditions are present. Such physical models are encountered in electromagnetic radiation, wave-guided, or scattering problems. The time-harmonic representation boundary value problem (BVP) of Figure 2.1 reads as:

$$\textit{Seek } \mathbf{E} \in \mathbf{H}_0\left(\mathbf{curl}; \Omega\right) \textit{ such that}$$

$$\begin{aligned} \nabla \times \tfrac{1}{\mu_r} \nabla \times \mathbf{E} - \epsilon_r k_o^2 \mathbf{E} &= -j\omega\mu_0 \mathbf{J}^{imp}, && \text{in } \Omega, \\ \hat{\mathbf{n}} \times \mathbf{E} &= 0, && \text{on } \Gamma_{PEC}, \\ \hat{\mathbf{n}} \times \tfrac{1}{\mu_r} \nabla \times (\mathbf{E} - \mathbf{E}^i) + jk_o \sqrt{\tfrac{\epsilon_r}{\mu_r}} \hat{\mathbf{n}} \times (\mathbf{E} - \mathbf{E}^i) \times \hat{\mathbf{n}} &= 0, && \text{on } \partial\Omega, \end{aligned} \tag{2.1}$$

where Ω is a finite computational domain, $\mathbf{E}$ is the total electrical field inside Ω, $\mathbf{J}^{imp}$ is a given port excitation current, $\mathbf{E}^i = \mathbf{E}\, e^{-j\mathbf{k_i}\cdot\mathbf{r}}$ is the given incident field where $\mathbf{k_i}$ denotes the direction of the incident plane wave. The relative permittivty and relative permeability of the media are denoted by ϵ_r, μ_r, respectively, and $k_0 = 2\pi f\sqrt{\epsilon_0\mu_0}$ is the free-space wave-number at operational frequency f. The outward pointing unit vector normal to the bounding surface is denoted by $\hat{\mathbf{n}}$. It is noted that the last equation in Equation (2.1) refers to the first order absorbing boundary condition (ABC) [48] applied at the truncation surface $\partial\Omega$, and is used to eliminate unwanted reflection from $\partial\Omega$, in an attempt to emulate the behavior of unbounded free-space. It is also

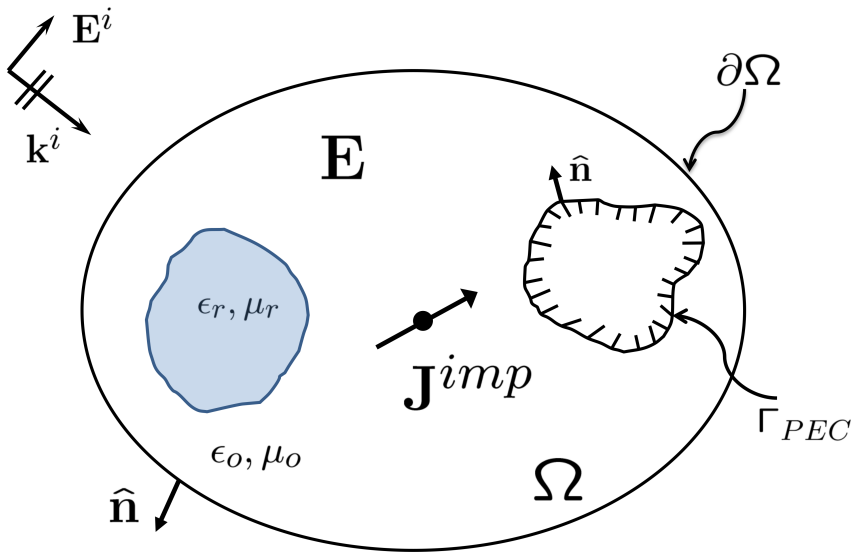

Figure 2.1. A generic EM system used for the developments in this chapter.

worth noting that the proposed BT-POD algorithm is not be restricted to the above boundary condtions as it will be demonstrated by the numerical examples in this chapter. In fact BT-POD has been used in conjunction with domain decomposition method that use Robin type transmission boundary conditions [49] and Floquet cell TVFEM that make use of periodic boundary condition [50].

The electrical field $\mathbf{E}$ is sought in the space of tangentially continuous fields defined by

$$\mathbf{H}_0(\mathbf{curl};\Omega) = \{\mathbf{u} \in \mathbf{H}_0(\mathbf{curl};\Omega) \ |\hat{\mathbf{n}} \times \mathbf{u} = 0 \ on \ \Gamma_{PEC}, \mathbf{u} \in \mathbf{H}(\mathbf{curl};\Omega)\}, \tag{2.2}$$

where

$$\mathbf{H}(\mathbf{curl};\Omega) = \{\mathbf{u} \in \mathbf{H}(\mathbf{curl};\Omega) \ | \ \nabla \times \mathbf{u} \in (\mathcal{L}_2(\Omega))^3, \mathbf{u} \in (\mathcal{L}_2(\Omega))^3\}, \tag{2.3}$$

where $\mathcal{L}_2(\Omega)$ is the set of square integrable functions over computational domain Ω.

2.1.1 Variational (Weak) Statement

The BVP statement in 2.1 will be solved via the finite element method which is based on a variational reformulation of the BVP. This section will breafly outline the procedure, used to arrive at a continuous variational statement.

From the partial differential equation in (2.1), a residual functional can be formed as

$$\mathbf{r}\left(\mathbf{E}\right) = \nabla \times \frac{1}{\mu_r} \nabla \times \mathbf{E} - k_o^2 \epsilon_r \mathbf{E} + j\omega\mu_0 \mathbf{J}^{imp} \quad \in \quad \mathbf{H}_0\left(\mathbf{div}; \Omega\right), \tag{2.4}$$

which belongs to the normally continuous vector function space defined by

$$\mathbf{H}_0\left(\mathbf{div}; \Omega\right) = \{\mathbf{u} \in \mathbf{H}_0\left(\mathbf{div}; \Omega\right) \mid \hat{\mathbf{n}} \cdot \mathbf{u} = 0 \; on \; \Gamma_{PEC}, \mathbf{u} \in \mathbf{H}\left(\mathbf{div}; \Omega\right)\}, \tag{2.5}$$

where

$$\mathbf{H}\left(\mathbf{div}; \Omega\right) = \{\mathbf{u} \in \mathbf{H}\left(\mathbf{div}; \Omega\right) \mid \nabla \cdot \mathbf{u} \in \left(\mathcal{L}_2\left(\Omega\right)\right)^3, \mathbf{u} \in \left(\mathcal{L}_2\left(\Omega\right)\right)^3\}. \tag{2.6}$$

Instead of searching for electrical field $\mathbf{E}$ that satisfies (2.1), the goal will be to find an electric field $\mathbf{E}$ that makes residual functional $\mathbf{r}\left(\mathbf{E}\right)$ zero. A systematic approach of achieving this goal is to try various functions $\mathbf{E} \in \mathbf{H}(\mathbf{curl}, \Omega)$ into $\mathbf{r}(\mathbf{E})$ and then test each residual functional $\mathbf{r}\left(\mathbf{E}\right)$ with appropriately chosen functions $\mathbf{v}$ through an appropriately defined duality-paring. The result of such procedure leads to

$$\left\langle \mathbf{r}\left(\mathbf{E}\right), \; \mathbf{v} \right\rangle_{\mathbf{H(div)} \times \mathbf{H(curl)}} = 0,$$

where

$$\left\langle \mathbf{r}\left(\mathbf{E}\right), \; \mathbf{v} \right\rangle_{\mathbf{H(div)} \times \mathbf{H(curl)}} = \int_{\Omega} \mathbf{r}\left(\mathbf{E}\right) \cdot \mathbf{v} \, dV.$$

After some algebraic manipulations that involve integration by parts and enforcement of the absorbing boundary condition (2.1), results the following variational statement

$$\textit{Seek } \mathbf{E} \in \mathbf{H}_0\left(\mathbf{curl};\Omega\right) \textit{ s.t.}$$

$$b\left(\mathbf{E},\mathbf{v}\right) = g\left(\mathbf{v}\right), \quad \forall \ \mathbf{v} \in \mathbf{H}_0(\mathbf{curl};\Omega), \tag{2.7}$$

where the bilinear form b and the linear from g are given by

$$\begin{aligned} b\left(\mathbf{E},\mathbf{v}\right) &= \int_\Omega \nabla\times\mathbf{v}\cdot\frac{1}{\mu_r}\nabla\times\mathbf{E}\,dr^3 - k_o^2\int_\Omega \mathbf{v}\cdot\epsilon_r\mathbf{E}\,dr^3 \\ &\quad + jk_0\oint_{\partial\Omega}\hat{\mathbf{n}}\times\mathbf{v}\cdot\hat{\mathbf{n}}\times\mathbf{E}\,dr^2, \\ g\left(\mathbf{v}\right) &= \oint_{\partial\Omega}\hat{\mathbf{n}}\times\mathbf{v}\cdot\hat{\mathbf{n}}\times\left(jk_o\mathbf{E}^i - \hat{\mathbf{n}}\times\frac{1}{\mu_r}\nabla\times\mathbf{E}^i\right)dr^2 \\ &\quad - j\omega\mu_0\int_\Omega \mathbf{J}^{imp}\cdot\mathbf{v}\,dr^3. \end{aligned}$$

2.1.2 Discrete Variational (Galerkin) Statement and TVFEM

The solution of the variational statement (2.7) is sought via the Galerkin discretization procedure of the continuous function space $\mathbf{H}_0\left(\mathbf{curl};\Omega\right)$ in (2.2). The solution of the original problem is sought through defining sequences of similar problems over finite dimensional subspaces $\mathbf{V}_h \subset \mathbf{H}\left(\mathbf{curl};\Omega\right)$. The discrete variational (Galerkin) statement reads as

$$\textit{Seek } \mathbf{E}_h \in \mathbf{V}_h \subset \mathcal{H}_0\left(\mathbf{curl};\Omega\right) \textit{ s.t.}$$

$$b\left(\mathbf{E}_h,\mathbf{v}_h\right) = g\left(\mathbf{v}_h\right), \quad \forall \ \mathbf{v}_h \in \mathbf{V}_h \subset \mathcal{H}_0(\mathbf{curl};\Omega) \tag{2.8}$$

where

$$\mathbf{V}_h = \{\mathbf{u} \in \mathbf{H}_0\left(\mathbf{curl};\Omega\right) |u|_\kappa \in \mathbf{ND_1}\left(\kappa\right), \kappa \in K\},$$

where $\mathbf{ND}_1$ denotes first Nedelec family of tangentially continuous finite element spaces [51], where κ is a tetrahedron in the mesh K of the geometry ($K = \cup_i \kappa_i$).

2.1.3 Finite Element Discretization

The finite element basis $\mathbf{ND}_1(\kappa)$ used in this work is characterized by the triplet $(\mathbf{K}\ \mathbf{P}_\kappa\ \mathbf{\Sigma}_\kappa)$, where

$$
\begin{aligned}
\mathbf{K} &= \text{tetrahedrons}, \\
\mathbf{P}_\kappa &= \left(\tilde{P}_1\right)^3 \oplus \mathbf{S}_2, \\
\mathbf{\Sigma}_\kappa &= \{\mathbf{\Sigma}_e \cup \mathbf{\Sigma}_f\},
\end{aligned}
\tag{2.9}
$$

where $\mathbf{K}$ is the set of the elements, $\mathbf{P}_\kappa$ is the set of polynomials and $\mathbf{\Sigma}$ is the set of degrees-of-freedom. In (2.9) $\tilde{P}_k$ is the space of k^{th} order homogeneous polynomials, $\mathbf{S}_k = \{\mathbf{u} \in (\tilde{P}_k)^3 \,|\, \mathbf{x} \cdot \mathbf{u} = 0\}$ and the FEM DoFs on tetrahedron edges $\mathbf{e}$ and faces $\mathbf{f}$ are linear functionals given by:

$$
\mathbf{\Sigma}_e = \{ \bigcup_{e \in \kappa, p \in [0,1]} \ell_{e,p}(\mathbf{u}), \text{where } \ell_{e,p}(\mathbf{u}) = \frac{1}{|e|} \int_e q_{e,p}\, \mathbf{u} \cdot \hat{\mathbf{t}}\, dt, \forall q_{e,p} \in P_1(e)\},
$$

and

$$
\mathbf{\Sigma}_f = \{ \bigcup_{f \in \kappa, p \in [0,1]} \ell_{f,p}(\mathbf{u}), \text{where } \ell_{f,p}(\mathbf{u}) = \frac{1}{|f|} \int_{\mathbf{f}} q_{f,p} \cdot \mathbf{u} \times \hat{\mathbf{n}}_f\, dS, \forall q_{p,f} \in (P_0(f))^2\},
$$

where $|e|$ is the edge length and $|f|$ is the face area. The vector $\hat{\mathbf{n}}_f$ is the outward pointing unit normal on the face f. The physical meaning of the above degrees-of-freedom is that they represent the moments of the circulation of the electric field across the tetrahedron edges, or the surface moments of the tangential fields across a face. Using the above FEM triplet, the FEM basis $\mathbf{w}_i \in \mathbf{ND}_1(\kappa)$ is constructed, the fields on the trial function space $\mathbf{V}_h$ are expanded as

$$
\mathbf{E}_h = \sum_{n=1}^{N} e_i \mathbf{w}_i, \tag{2.10}
$$

where the test function space

$$
\mathbf{V} \in \text{span}\{\mathbf{w}_1, \mathbf{w}_2, \cdots, \mathbf{w}_N\}. \tag{2.11}
$$

Substituing (2.10) and (2.11) into the discrete variational statement the following TVFEM matrix equation can be obtained

$$\begin{aligned} \left(s^2\mathbf{M} + s\mathbf{D} + \mathbf{S}\right)\mathbf{e} &= \mathbf{b}, \\ \mathbf{y} &= \mathbf{C}^T\mathbf{e}, \end{aligned} \tag{2.12}$$

where $\mathbf{e} = [e_1, e_2, \cdots, e_N]^T \in \mathbb{C}^N$, $s = j\omega$ is the Laplace frequency

$$\begin{aligned} \mathbf{S}_{ij} &= \int_\Omega \nabla \times \mathbf{w}_j \cdot \frac{1}{\mu_r} \nabla \times \mathbf{w}_i \, dr^3, \\ \mathbf{D}_{ij} &= \frac{1}{c} \oint_{\partial\Omega} \hat{\mathbf{n}} \times \mathbf{w}_j \cdot \hat{\mathbf{n}} \times \mathbf{w}_i \, dr^2, \\ \mathbf{M}_{ij} &= \frac{1}{c^2} \int_\Omega \mathbf{w}_j \cdot \epsilon_r \mathbf{w}_i \, dr^3, \\ \mathbf{b}_j &= \oint_{\partial\Omega} \hat{\mathbf{n}} \times \mathbf{w}_j \cdot \hat{\mathbf{n}} \times \left(\frac{s}{c}\mathbf{E}^i - \hat{\mathbf{n}} \times \frac{1}{\mu_r} \nabla \times \mathbf{E}^i \right) dr^2 \\ &\quad - s\mu_0 \int_\Omega \mathbf{w}_j \cdot \mathbf{J}^{imp} \, dr^3, \\ \mathbf{C}_{ij} &= s\mu_0 \int_\Omega \mathbf{w}_i \cdot \mathbf{J}_j^{mode} \, dr^3, \end{aligned} \tag{2.13}$$

where c denotes the speed of light in free space. $\{\mathbf{S}, \mathbf{D}, \mathbf{M}\} \in \mathbb{C}^{N \times N}$ where N denotes the total number of DoF in the TVFEM model, $\mathbf{e} \in \mathbb{C}^{N \times 1}$ is a vector with the electric fields DoFs, and $\mathbf{C} \in \mathbb{C}^{N \times P}$ is a matrix that maps the electric field to the engineering quantity of interest, where in this specific case it has been chosen to be the scattering parameter at each port in the model. Here we have assumed that there are P ports in the EM model, and $\mathbf{y} \in \mathbb{C}^{P \times 1}$ represents the system outputs that often are the reflection coefficients or scattering parameters at each port. Note that equation (2.12) is the frequency (dynamical) representation of the TVFEM model that includes lossy or active linear media, conductors, wave ports, and ABC boundary condition. This general form remains unchanged when driven infinitely periodic problems such as infinite antenna arrays or frequency selective surfaces, where the explicit form of $\mathbf{M}$ and $\mathbf{S}$ must be modified.

Within the context of this work, we only consider the EM radiation problems which implies $\mathbf{E}^i = 0$, thus the right-hand-side $\mathbf{b}$ could also be written as

$$\mathbf{b} = \mathbf{C}\,\mathbf{f},$$

where $\mathbf{f} = [f_1, f_2, \cdots, f_P]^T \in \mathbb{C}^{P\times 1}$ is the excitation coefficient vector of EM system ports. Finally, the TVFEM model considered in this work is given as follows

$$\begin{aligned} \left(s^2\mathbf{M} + s\mathbf{D} + \mathbf{S}\right)\mathbf{e} &= \mathbf{C}\,\mathbf{f}, \\ \mathbf{y} &= \mathbf{C}^T\mathbf{e}. \end{aligned} \tag{2.14}$$

2.2 First-order Linear Time Invariant System Gramians

Before developing the proposed algorithm, we first review some theory for the general first-order dynamical time systems of the form:

$$\begin{aligned} \tfrac{d}{dt}\mathbf{x}(t) &= \mathbf{A}\mathbf{x}(t) + \mathbf{B}\mathbf{u}(t), \\ \mathbf{y}(t) &= \mathbf{C}\mathbf{x}(t) + \mathbf{D}\mathbf{u}(t), \end{aligned} \tag{2.15}$$

where $\mathbf{A} \in \mathbb{R}^{N\times N}, \mathbf{B} \in \mathbf{R}^{N\times P}, \mathbf{C} \in \mathbb{R}^{P\times N}, \mathbf{D} \in \mathbb{R}^{P\times P}$ are the constant linear maps of a P-input, P-output linear system. $\mathbf{x} \in \mathbb{R}^{N\times 1}$ is the *state* of the system, while $\mathbf{u} \in \mathbb{R}^{P\times 1}$ is the input function and $\mathbf{y} \in \mathbb{R}^{P\times 1}$ is the output function.

The frequency domain representation of (2.15) is obtained via the Laplace transform,

$$\begin{aligned} s\mathbf{x} &= \mathbf{A}\mathbf{x} + \mathbf{B}\mathbf{u}, \\ \mathbf{y} &= \mathbf{C}\mathbf{x} + \mathbf{D}\mathbf{u}. \end{aligned} \tag{2.16}$$

In control theory, a set of positive definite matrices called gramians are associated with the first-order LTI system of (2.16) [19]. These gramians play an important role

in system input-output manipulation. Namely, the *reachability* gramian $\boldsymbol{\mathcal{P}} \in \mathbb{R}^{N\times N}$ allows to identify the extent to which a state of the system $\mathbf{x}$ can be manipulated through the input $\mathbf{u}$, whereas the *observability* gramian $\boldsymbol{\mathcal{Q}} \in \mathbb{R}^{N\times N}$ encodes the information of state-to-output. Physically, system gramians are related to the energy that can be coupled to the system and from the system, for a given set of inputs and outputs. More specifically, the reachability gramian $\boldsymbol{\mathcal{P}}$ and observability gramian $\boldsymbol{\mathcal{Q}}$ define the following energy inner products,

$$\begin{aligned} E_r &= \mathbf{x}^*\boldsymbol{\mathcal{P}}^{-1}\mathbf{x}, \\ E_o &= \mathbf{x}^*\boldsymbol{\mathcal{Q}}\mathbf{x}, \end{aligned} \tag{2.17}$$

where E_r *denotes the minimum energy required to steer the system from state* $\mathbf{0}$ *to* $\mathbf{x}$*, while* E_o *is the maximum energy that could be obtained by observing the system output at state* $\mathbf{x}$ *with zero excitation.* Implicitly, the above definition implies that the eigenvalue decomposition (EVD) of the gramian could identify the modes (states) that do not contribute a lot of energy in the output or are not "energized" by the input. In the words of mode analysis, this addresses that such low energy modes can be eliminated all together leading to a reduced model representation of the original system model. This fundamental concept is behind any SVD-based MOR technique. The present work will follow the same principle for MOR.

The two gramians of a first order LTI system satisfy the continuous-time Lyapunov equations [19],

$$\begin{aligned} \mathbf{A}\boldsymbol{\mathcal{P}} + \boldsymbol{\mathcal{P}}\mathbf{A}^* + \mathbf{B}\mathbf{B}^* &= 0, \\ \mathbf{A}^*\boldsymbol{\mathcal{Q}} + \boldsymbol{\mathcal{Q}}\mathbf{A} + \mathbf{C}^*\mathbf{C} &= 0. \end{aligned} \tag{2.18}$$

Since Lyapunov equations are matrix-matrix linear equations and the gramians are dense matrices even when $\mathbf{A}, \mathbf{B}$ and $\mathbf{C}$ are sparse, solving such system to obtain

$\boldsymbol{\mathcal{P}}$ and $\boldsymbol{\mathcal{Q}}$ is impractical for large-scale problems (e.g. $N > 10^3$). Therefore obtaining the gramians from (2.18) is a major computational bottleneck for SVD-MOR.

This work will attempt to an alternative computation of gramians that is based on the following lemma.

Lemma 2.2.1 (Frequency-domain representation of gramians) *If $\boldsymbol{\mathcal{P}}$ and $\boldsymbol{\mathcal{Q}}$ are the continuous-time gramians of a stable first order LTI system given by (2.16) that satisfy (2.18), then they can be represented in the following frequency-domain form*

$$\begin{aligned} \boldsymbol{\mathcal{P}} &= \frac{1}{j2\pi} \int_{-j\infty}^{j\infty} (s\mathbf{I} - \mathbf{A})^{-1} \mathbf{B}\mathbf{B}^* (-s\mathbf{I} - \mathbf{A}^*)^{-1} \, ds, \\ \boldsymbol{\mathcal{Q}} &= \frac{1}{j2\pi} \int_{-j\infty}^{j\infty} (-s\mathbf{I} - \mathbf{A}^*)^{-1} \mathbf{C}^*\mathbf{C} (s\mathbf{I} - \mathbf{A})^{-1} \, ds. \end{aligned} \tag{2.19}$$

Proof Left multiply with $(s\mathbf{I} - \mathbf{A})^{-1}$ and right multiply with $(-s\mathbf{I} - A^*)^{-1}$, the first equation of (2.18) becomes

$$\boldsymbol{\mathcal{P}} (-s\mathbf{I} - \mathbf{A}^*)^{-1} + (s\mathbf{I} - \mathbf{A})^{-1} \boldsymbol{\mathcal{P}} = (s\mathbf{I} - \mathbf{A})^{-1} \mathbf{B}\mathbf{B}^* (-s\mathbf{I} - \mathbf{A}^*)^{-1}.$$

Thus a complex s-plane integration is obtained as

$$\oint_C \boldsymbol{\mathcal{P}} (-s\mathbf{I} - \mathbf{A}^*)^{-1} \, ds + \oint_C (s\mathbf{I} - \mathbf{A})^{-1} \boldsymbol{\mathcal{P}} \, ds = \oint_C (s\mathbf{I} - \mathbf{A})^{-1} \mathbf{B}\mathbf{B}^* (-s\mathbf{I} - \mathbf{A}^*)^{-1} \, ds, \tag{2.20}$$

where integral contour $C = C_I + C_\infty$ is shown in Figure 2.2. In this figure, the poles of $(s\mathbf{I} - \mathbf{A})^{-1}$, i.e., the eigenvalues of $\mathbf{A}$ are denoted by crosses, whereas the poles of $(-s\mathbf{I} - \mathbf{A}^*)^{-1}$ which corresponds to the adjoint system, i.e., the eigenvalues of $-\mathbf{A}^*$ are denoted by dots. The integration contour C is defined such that it includes all the poles of the system while all the poles of the adjoint system are exlucded. According to Cauchy-Goursat theorem and Cauchy integral formula [52],

$$\oint_C \boldsymbol{\mathcal{P}} (-s\mathbf{I} - \mathbf{A}^*)^{-1} \, ds = \mathbf{0},$$

$$\begin{aligned}
&\oint_C (s\mathbf{I}-\mathbf{A})^{-1}\boldsymbol{\mathcal{P}}\,ds \\
&= j2\pi\sum_{i=1}^{n}(s\mathbf{I}-\mathbf{A})^{-1}\boldsymbol{\mathcal{P}}\,(s-s_i) \\
&= j2\pi\boldsymbol{\mathcal{P}}
\end{aligned}$$

where $\{s_i, i=1,2,\cdots,n\}$ are the eigenvalues of $\mathbf{A}$.

The right-hand-side of (2.20) is further written as

$$\begin{aligned}
&\oint_C (s\mathbf{I}-\mathbf{A})^{-1}\mathbf{B}\mathbf{B}^*(-s\mathbf{I}-\mathbf{A}^*)^{-1}\,ds \\
&= \int_{C_I}(s\mathbf{I}-\mathbf{A})^{-1}\mathbf{B}\mathbf{B}^*(-s\mathbf{I}-\mathbf{A}^*)^{-1}\,ds + \int_{C_\infty}(s\mathbf{I}-\mathbf{A})^{-1}\mathbf{B}\mathbf{B}^*(-s\mathbf{I}-\mathbf{A}^*)^{-1}\,ds.
\end{aligned}$$

At C_∞, $s\to\infty$, thus

$$\lim_{s\to\infty}(s\mathbf{I}-\mathbf{A})^{-1}\mathbf{B}\mathbf{B}^*(-s\mathbf{I}-\mathbf{A}^*)^{-1} = \mathbf{0}.$$

Therefore,

$$\oint_C (s\mathbf{I}-\mathbf{A})^{-1}\mathbf{B}\mathbf{B}^*(-s\mathbf{I}-\mathbf{A}^*)^{-1}\,ds = \int_{-j\infty}^{j\infty}(s\mathbf{I}-\mathbf{A})^{-1}\mathbf{B}\mathbf{B}^*(-s\mathbf{I}-\mathbf{A}^*)^{-1}\,ds,$$

and this leads to

$$\boldsymbol{\mathcal{P}} = \frac{1}{j2\pi}\int_{-j\infty}^{j\infty}(s\mathbf{I}-\mathbf{A})^{-1}\mathbf{B}\mathbf{B}^*(-s\mathbf{I}-\mathbf{A}^*)^{-1}\,ds. \tag{2.21}$$

The observability gramian can be obtained in the similar way. ∎

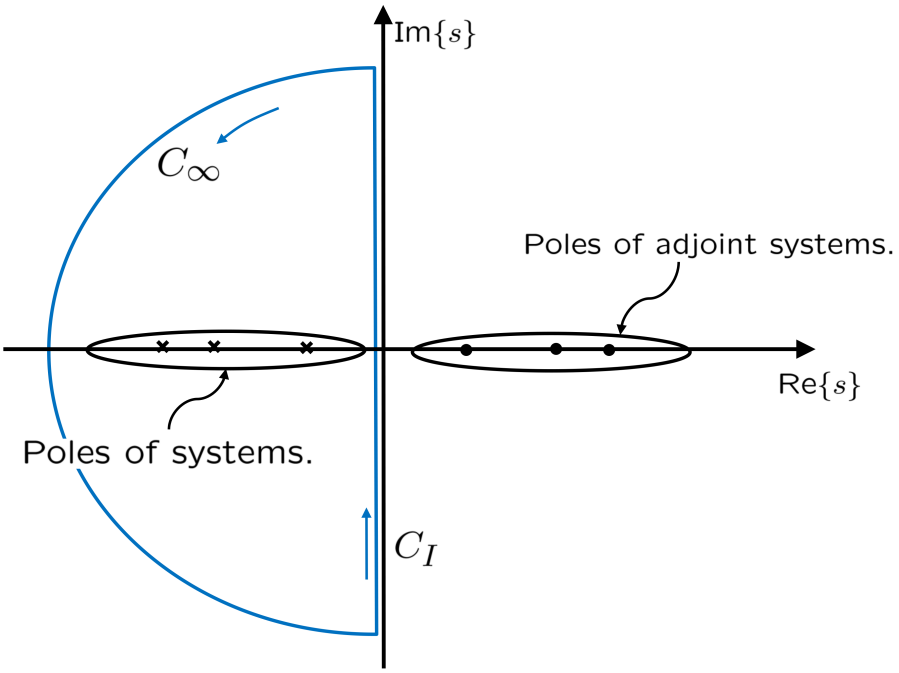

Figure 2.2. Contour integration over s-plane.

Alternatively, the two gramians in (2.19) can be rewritten in terms of system transfer functions as,

$$\begin{aligned} \boldsymbol{\mathcal{P}} &= \frac{1}{j2\pi} \int_{-j\infty}^{j\infty} \mathbf{H}(s)\mathbf{H}^*(s)\, ds, \\ \boldsymbol{\mathcal{Q}} &= \frac{1}{j2\pi} \int_{-j\infty}^{j\infty} \mathbf{H}_a^*(s)\mathbf{H}_a(s)\, ds, \end{aligned} \tag{2.22}$$

where the transfer function $\mathbf{H}$ is that of the forward form and $\mathbf{H}_a$ that of the adjoint form are given as

$$\begin{aligned} \mathbf{H}(s) &= (s\mathbf{I} - \mathbf{A})^{-1}\mathbf{B}, \\ \mathbf{H}_a(s) &= \mathbf{C}\,(-s\mathbf{I} - \mathbf{A}^*)^{-1}. \end{aligned} \tag{2.23}$$

The frequency domain representation of the gramians in (2.26) suggests an alternative computation that bypass altogether the expensive solution of the Lyapunov equations. It is noted that this is the key observation that is exploited in this work.

2.3 TVFEM System Gramians Approximation

Equation (2.14) describes the dyanmical behavior of an EM system formulated by TVFEM with input $\mathbf{f}$, output $\mathbf{y}$ and the electric field $\mathbf{e}$, i.e., system internal state variables. This equation describes a second-order system which tends to be more difficult and expensive to solve than first-order system. In the following derivation, we assume that the dissipation term in (2.14) denoted by $s\mathbf{D}$ is only perturbative, which means that the losses is considerablly small thus the form of first-order gramians will be assumed valid. Although this assumption is not strictly true for radiation and scattering problems, it has been found through numerical observations to give sufficiently good results. It must be highlighted here that although the form of the gramian is approximated to be first order, the full second order transfer function has been used for the computation of the gramians from a number of numerical experiments. Therefore approximating (2.14) to the first-order LTI form:

$$\begin{aligned} (s'\mathbf{M} + \mathbf{S})\mathbf{e} &= \mathbf{C}\,\mathbf{f}, \\ \mathbf{y} &= \mathbf{C}^T\mathbf{e}, \end{aligned} \tag{2.24}$$

where $s' = s^2$.

The benefit of (2.24) is we can numerically solve the TVFEM system gramians through applying the LTI system gramians formulation in terms of system transfer functions, which is given in (2.19) and (2.23). Thus two transfer functions for forward and adjoint form of the original TVFEM system (2.14) are introduced by

$$\begin{aligned}\mathbf{H}(s) &= \left(s^2\mathbf{M} + s\mathbf{D} + \mathbf{S}\right)^{-1}\mathbf{C} \in \mathbb{C}^{N\times P} \\ \mathbf{H}_a(s) &= \mathbf{C}^*\left(s^2\mathbf{M} - s\mathbf{D} + \mathbf{S}\right)^{-1} \in \mathbb{C}^{P\times N}\end{aligned} \tag{2.25}$$

It is observed that the integration range for system gramians found in (2.19) covers the entire complex imaginary axis which is not reasonable for real computations. An intuitive way to tackle this problem is to convert the integration along only the postive complex imaginary axis. Consider the quantity,

$$\mathbf{H}'(s) = \mathbf{H}(s)\mathbf{H}^*(s),$$

and

$$\begin{aligned}\mathbf{H}'(-s) &= \mathbf{H}(-s)\mathbf{H}^*(-s) \\ &= \left(s^2\mathbf{M} - s\mathbf{D} + \mathbf{S}\right)^{-1}\mathbf{C}\mathbf{C}^*\left(s^2\mathbf{M} + s\mathbf{D} + \mathbf{S}\right)^{-1} \\ &= \mathbf{H}^*(s)\mathbf{H}(s) \\ &= \mathbf{H}'(s).\end{aligned}$$

Therefore for all casual systems, $\mathbf{H}'(s) = \mathbf{H}(s)\mathbf{H}^*(s)$ is an even function over the s-plane. Similarly, the same conclusion to the adjoint quantity $\mathbf{H}'_a(s) = \mathbf{H}^*_a(s)\mathbf{H}_a(s)$. Thus system gramians integration in (2.19) can be elegantly written as

$$\begin{aligned}\boldsymbol{\mathcal{P}} &= \frac{1}{\pi j}\int_0^{j\infty}\mathbf{H}(s)\mathbf{H}^*(s)\,ds, \\ \boldsymbol{\mathcal{Q}} &= \frac{1}{\pi j}\int_0^{j\infty}\mathbf{H}^*_a(s)\mathbf{H}_a(s)\,ds.\end{aligned} \tag{2.26}$$

As mentioned before, this work will attempt to compute system gramians by the complex integration over the imaginary Laplace axis instead of solving the Lyapunov

equations. This integration problem can be tackled through the use of numerical quadratures. It is apparant to observe that thse quadratures would require the evalution of integrant matrix $\mathbf{H}(s)\mathbf{H}^*(s)$ at each discrete sampling frequency s_i, therefore require the solution of a TVFEM model at that frequency. In this chapter, the simplest integration rule based on the Riemannian sum will be used. Following such approach, based on the infinite gramians expression in (2.26), system gramians over $[s_{min}, s_{max}]$ can be approximated as

$$\begin{aligned} \tilde{\boldsymbol{\mathcal{P}}} &= \frac{s_{max} - s_{min}}{jK\pi} \sum_{k=1}^{K} \mathbf{H}(s_k)\mathbf{H}^*(s_k), \\ \tilde{\boldsymbol{\mathcal{Q}}} &= \frac{s_{max} - s_{min}}{jK\pi} \sum_{k=1}^{K} \mathbf{H}_a^*(s_k)\mathbf{H}_a(s_k), \end{aligned} \tag{2.27}$$

where K is the total number of sampling points. Figure 2.3 briefly illustrates the Riemannian sum approximation of system reachability gramian.

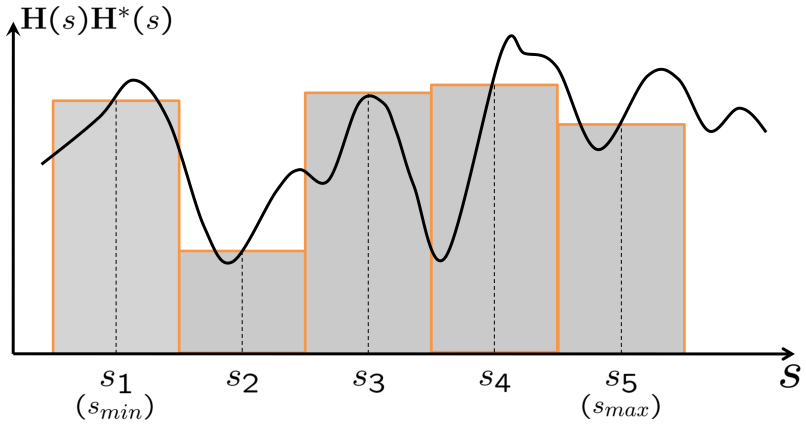

Figure 2.3. System reachability gramian approximation via Riemannian sum.

It should be remarked that such approach is considered as Proper Orthogonal Decomposition (POD) method [53] which is a powerful and elegant way to obtain

a low-dimensional descriptions of high-dimensional system. A careful observation of (2.27) results that the gramians can be expressed in the following matrix form,

$$\begin{aligned} \tilde{\boldsymbol{\mathcal{P}}} &= \mathbf{U}\mathbf{U}^*, \\ \tilde{\boldsymbol{\mathcal{Q}}} &= \mathbf{L}^*\mathbf{L}, \end{aligned} \tag{2.28}$$

where

$$\mathbf{U} = \sqrt{\frac{s_{max} - s_{min}}{jK\pi}}[\mathbf{H}(s_1)\ \mathbf{H}(s_2)\ \cdots\ \mathbf{H}(s_K)] \in \mathbb{C}^{N\times KP}$$

and

$$\mathbf{L} = \sqrt{\frac{s_{max} - s_{min}}{jK\pi}}[\mathbf{H}_a(s_1)\ \mathbf{H}_a(s_2)\ \cdots\ \mathbf{H}_a(s_K)] \in \mathbb{C}^{N\times KP}$$

where P is the total number of ports inside the EM system. It is worth noting that (2.28) is the most important step of the proposed BT-POD algorithm. (2.28) suggests a low-rank Choleski factorization of the gramians. The factorized form of (2.28) resembles the Choleski factorization of the gramian matrices, thus $\mathbf{L}$ and $\mathbf{U}$ are the low-rank Choleski factors of system gramians. More importantly, the low-rank factors contain the same information as the gramians, but require significantly lower memory for storage ($N \times KP$ instead of $N \times N$) since $KP \ll N$ due to the rank deficient nature of the system gramians.

As can be seen, the computation of the low-rank Choleski factors require the solution of the full model at a set of discrete sampling frequency points in the entire bandwidth for each port excitation. As will be explained later, this part of computation is the most time consuming step in the proposed BT-POD algorithm. However, the efficiency can be significantly improved by performing a parallel computation for different frequency points and port excitation without any communication between different processor nodes.

2.4 Model Balancing and Truncation

Many model order reduction techniques perform the reduction by observing the input and the output separately thus leading to a reduced model that is not optimal. In a balanced MOR technique like BT-POD, system states that are simultaneously difficult to reach and observe are identified and discarded at the truncation step. Here the main question is how to find a transformation that identifies such states.

In contrast to previous work [30], [32] that attempts to perform the EVD of $\boldsymbol{\mathcal{P}}$ and $\boldsymbol{\mathcal{Q}}$, this work will attempt a computationally more efficient approach based on the low-rank Hankel matrix [19]. The Hankel matrix is given in terms of the Choleski factors,

$$\boldsymbol{\mathcal{H}} = \mathbf{U}^*\mathbf{L}, \tag{2.29}$$

where in the case of low rank $\mathbf{U}$ and $\mathbf{L}$, the dimension of Hankel matrix $\boldsymbol{\mathcal{H}}$ is $KP \times KP$. The Hankel matrix is in general non-symmetric and its diagonalization

$$\boldsymbol{\mathcal{H}} = \mathbf{W}\boldsymbol{\Sigma}\mathbf{V}^* \tag{2.30}$$

are the Hankel singular values (HSVs) and $\mathbf{W}$ and $\mathbf{V}$ are the left and right singular vectors. To further reduce the size of the reduced model, a truncation strategy based on the HSVs is considered. The HSVs and vectors are partitioned as

$$\boldsymbol{\Sigma} = \begin{bmatrix} \boldsymbol{\Sigma}_1 & \\ & \boldsymbol{\Sigma}_\epsilon \end{bmatrix}, \tag{2.31}$$

and

$$\mathbf{W} = [\mathbf{W}_1 \ \mathbf{W}_\epsilon], \qquad \mathbf{V}^* = [\mathbf{V}_1 \ \mathbf{V}_\epsilon]^*. \tag{2.32}$$

In (2.31) and (2.32), the singular values and vectors have been partitioned into two groups denoted by subscripts 1 and ϵ. Subscript ϵ is to denote singluar values (and

corresponding singular vectors) that are below a user defined, small truncation value, which is used to discard low energy modes (system states). It should be emphasized that the HSVs rapidly decay to zero, with a decay rate which heavily depends on the information capacity of the system. Only the modes with large singular values carry enough energy and that will be the modes that are used to form the reduced system. Some research work about estimating the bounds of Hankel singular values have been done in the past, and those can be found in [19].

A typical decay of Hankel singular values from an EM model is given in Figure 2.4 where a truncation tolerence $\epsilon = 10^{-4}$ leads to a reduced model with $n = 12$ significant modes. It is also worth noting the above process closely resembles the Karhunen-Loeve (K-L) expansion [15] of stochastic systems or principal component analysis (PCA) [54].

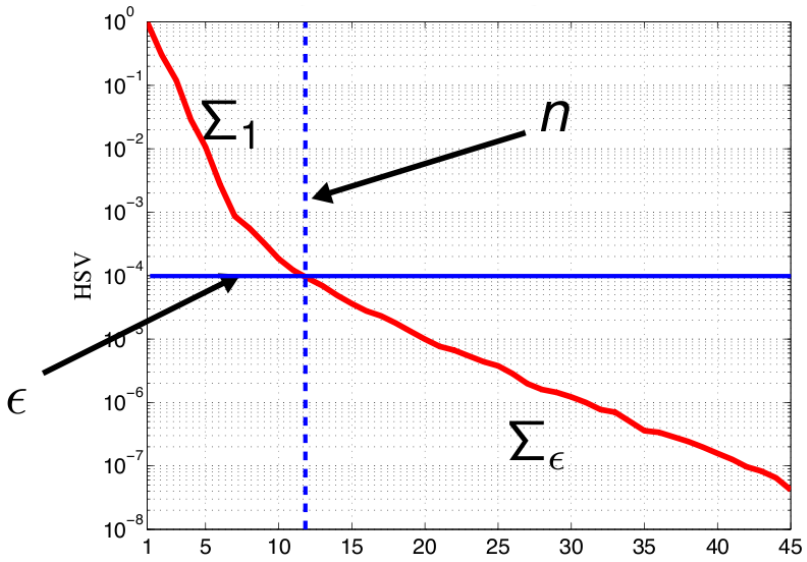

Figure 2.4. Truncation on Hankel singular values.

In LTI system theory, the system is reachable or observable only if the reachability or observability gramian matrices are diagonalizable via Shure decomposition as

follows

$$\mathbf{D}_{\boldsymbol{\mathcal{P}}} = \mathbf{T}\,\boldsymbol{\mathcal{P}}\,\mathbf{T}^*, \qquad \mathbf{D}_{\boldsymbol{\mathcal{Q}}} = \mathbf{T}^{-*}\,\boldsymbol{\mathcal{Q}}\,\mathbf{T}^{-1}, \tag{2.33}$$

where $\mathbf{D}_{\boldsymbol{\mathcal{P}}}$ and $\mathbf{D}_{\boldsymbol{\mathcal{Q}}}$ are diagonal matrices. The concept of balancing is to find such non singular transformation $\mathbf{T}$ that minimizes the following quantity,

$$\min_{\mathbf{T}} \ \text{trace}\left[\mathbf{T}\,\boldsymbol{\mathcal{P}}\,\mathbf{T}^* + \mathbf{T}^{-*}\,\boldsymbol{\mathcal{Q}}\,\mathbf{T}^{-1}\right]$$

Or in other words, to find $\mathbf{T}$ such that $\mathbf{D}_{\boldsymbol{\mathcal{P}}} = \mathbf{D}_{\boldsymbol{\mathcal{Q}}}$.

The balancing transformation is achieved through the following theorem.

Theorem 2.4.1 (Balancing transformation) *Given the reachable, observable and stable first order LTI system in (2.16), and the corresponding gramian $\boldsymbol{\mathcal{P}}$ and $\boldsymbol{\mathcal{Q}}$, the transformation*

$$\begin{aligned} \mathbf{T} \equiv \mathbf{T}_L &= \mathbf{V}_1^*\mathbf{L}^*, \\ \mathbf{T}^{-1} \equiv \mathbf{T}_R &= \mathbf{U}\mathbf{W}_1 \end{aligned} \tag{2.34}$$

is a balancing transformation.

Proof

$$\begin{aligned} \mathbf{D}_{\boldsymbol{\mathcal{P}}} &= \mathbf{T}\,\boldsymbol{\mathcal{P}}\,\mathbf{T} \\ &= \mathbf{T}_L\,\boldsymbol{\mathcal{P}}\,\mathbf{T}_L^* \\ &= (\mathbf{V}^*\mathbf{L}^*)\ \mathbf{U}\mathbf{U}^*\ (\mathbf{L}\mathbf{V}) \\ &= \mathbf{V}^*\,(\mathbf{L}^*\mathbf{U})\,(\mathbf{U}^*\mathbf{L})\,\mathbf{V} \\ &= \mathbf{V}^*\,(\mathbf{V}\boldsymbol{\Sigma}\mathbf{W}^*)\,(\mathbf{W}\boldsymbol{\Sigma}\mathbf{V}^*)\,\mathbf{V} \\ &= (\mathbf{V}^*\mathbf{V})\,\boldsymbol{\Sigma}\,(\mathbf{W}^*\mathbf{W})\,\boldsymbol{\Sigma}\,(\mathbf{V}^*\mathbf{V}) \\ &= \boldsymbol{\Sigma}^2 \end{aligned}$$

$$
\begin{aligned}
\mathbf{D}_{\boldsymbol{\mathcal{Q}}} &= \mathbf{T}^{-*}\,\boldsymbol{\mathcal{P}}\,\mathbf{T}^{-1} \\
&= \mathbf{T}_R^{*}\,\boldsymbol{\mathcal{Q}}\,\mathbf{T}_R \\
&= \left(\mathbf{W}^{*}\mathbf{U}^{*}\right)\,\mathbf{L}^{*}\mathbf{L}\,\left(\mathbf{U}\mathbf{W}\right) \\
&= \mathbf{W}^{*}\left(\mathbf{U}^{*}\mathbf{L}\right)\left(\mathbf{L}^{*}\mathbf{U}\right)\mathbf{W} \\
&= \mathbf{W}^{*}\left(\mathbf{W}\boldsymbol{\Sigma}\mathbf{V}^{*}\right)\left(\mathbf{V}\boldsymbol{\Sigma}\mathbf{W}^{*}\right)\mathbf{W} \\
&= \left(\mathbf{W}^{*}\mathbf{W}\right)\boldsymbol{\Sigma}\left(\mathbf{V}^{*}\mathbf{V}\right)\boldsymbol{\Sigma}\left(\mathbf{W}^{*}\mathbf{W}\right) \\
&= \boldsymbol{\Sigma}^{2}
\end{aligned}
$$

Therefore $\mathbf{D}_{\boldsymbol{\mathcal{P}}} = \mathbf{D}_{\boldsymbol{\mathcal{Q}}}$, it is a balancing transformation. ∎

2.5 TVFEM Model Reduction

The reduced TVFEM model through a Petrov-Galerkin projection with the transformation matrices in (2.34) is obtained as

$$
\begin{aligned}
\left(s^2\tilde{\mathbf{M}} + s\tilde{\mathbf{D}} + \tilde{\mathbf{S}}\right)\tilde{\mathbf{e}} &= \tilde{\mathbf{B}}\,\tilde{\mathbf{f}}, \\
\tilde{\mathbf{y}} &= \tilde{\mathbf{C}}\,\tilde{\mathbf{e}},
\end{aligned}
\tag{2.35}
$$

where

$$
\begin{aligned}
\tilde{\mathbf{S}} &= \mathbf{T}_{\mathbf{L}}\,\mathbf{S}\,\mathbf{T}_{\mathbf{R}} \in \mathbb{C}^{n\times n} \\
\tilde{\mathbf{M}} &= \mathbf{T}_{\mathbf{L}}\,\mathbf{M}\,\mathbf{T}_{\mathbf{R}} \in \mathbb{C}^{n\times n} \\
\tilde{\mathbf{D}} &= \mathbf{T}_{\mathbf{L}}\,\mathbf{D}\,\mathbf{T}_{\mathbf{R}} \in \mathbb{C}^{n\times n} \\
\tilde{\mathbf{B}} &= \mathbf{T}_{\mathbf{L}}\,\mathbf{C} \in \mathbb{C}^{n\times P} \\
\tilde{\mathbf{C}} &= \mathbf{C}^{T}\,\mathbf{T}_{\mathbf{R}} \in \mathbb{C}^{P\times n}
\end{aligned}
\tag{2.36}
$$

Having reduced the full TVFEM model to that of (2.35), a full bandwidth sweep of system response can be performed very fast through a direct solver since the size of

the reduced system n satisfies

$$n \leq KP$$

while in most of the situations, $KP < 50$.

2.6 Algorithm Summary and Complexity Analysis

To better understand the BT-POD approach for frequency parameter sweep, an algorithm description (Algorithm 1) is provided that includes the most important steps.

Algorithm 1 : BT-POD MOR for TVFEM

INPUT:
ε: HSVs truncation tolerance
tol_s: iterative solution tolerence
K: expansion points number on system Gramian integral dimension
s_{min} s_{max}: minimum and maximum frequency
M: sweep number ($M \gg K$)

OUTPUT:
n: dimension of reduced-order system
$\tilde{\mathbf{y}}$: output parameter of interests

DEFINITIONS:
$\mathbf{U}^{N\times KP}$: matrix concatenated by $\mathbf{H}^i$, for i: $1 \to KP$
$\mathbf{L}^{KP\times N}$: matrix concatenated by $\mathbf{H}_a^i$, for i: $1 \to KP$
P: total number of ports
$s = j\omega$: Laplace frequency

1: Assemble global FEM matrices $\mathbf{M}$, $\mathbf{D}$, $\mathbf{S}$ and excitation matrix $\mathbf{B}$, $\mathbf{C}$.

2: POD sampling
for s_k $(k : 1 \to K)$
Find uniformly distributed s_k
for port $p : 1 \to P$
Find excitation coeff. f_p
Solve iteratively $(s^2\mathbf{M} + s\mathbf{D} + \mathbf{S})\mathbf{e} = \mathbf{B}\mathbf{f}_p$, $\mathbf{H}^{(k-1)P+p} = \mathbf{e}$
[Solve adjoint problem iterative $(s^2\mathbf{M} - s\mathbf{D} + \mathbf{S})\mathbf{e} = \mathbf{C}\mathbf{f}_p$, $\mathbf{H}_a^{(k-1)P+p} = \mathbf{e}$]
end for
Concatenate $\mathbf{H}_{k,p}$ on $\mathbf{U}$ and $\mathbf{H}_a^{k,p}$ on $\mathbf{L}$ files, update $\mathbf{U}^*\mathbf{L}$
end for

3: Perform SVD on Hankel Matrix
$\mathbf{U}^*\mathbf{L}$=$\mathbf{W}\mathbf{\Sigma}\mathbf{V}^*$

4: Truncate SVD ($\mathbf{W}$, $\mathbf{\Sigma}$, $\mathbf{V}^*$):
$\mathbf{\Sigma_1}^{n\times n}$: $\sigma_i > \varepsilon$, for $i : 1 \to n$
$\mathbf{W} = [\mathbf{W}_1\ \mathbf{W}_\varepsilon]$, $\quad \mathbf{V}^* = [\mathbf{V}_1\ \mathbf{V}_\varepsilon]^*$

5: Construct balancing transformation matrices
$\mathbf{T}_L = \mathbf{V_1}^*\mathbf{L}^* \quad \mathbf{T}_R = \mathbf{U}\mathbf{W_1}$

6: Construct reduced system matrices $\tilde{\mathbf{M}}$, $\tilde{\mathbf{D}}$, $\tilde{\mathbf{S}}$, $\tilde{\mathbf{B}}$ and $\tilde{\mathbf{C}}$ by
$\tilde{\mathbf{M}} = \mathbf{T}_L\,\mathbf{M}\,\mathbf{T}_R \quad \tilde{\mathbf{D}} = \mathbf{T}_L\,\mathbf{D}\,\mathbf{T}_R \quad \tilde{\mathbf{S}} = \mathbf{T}_L\,\mathbf{S}\,\mathbf{T}_R \quad \tilde{\mathbf{B}} = \mathbf{T}_L\,\mathbf{B} \quad \tilde{\mathbf{C}} = \mathbf{C}^T\,\mathbf{T}_R$

7: Perform frequency sweep
for s_m $(m : 1 \to M)$ Solve reduced system via a direct solver
$(s_m^2\tilde{\mathbf{M}} + s_m\tilde{\mathbf{D}} + \tilde{\mathbf{S}})\tilde{\mathbf{e}} = \tilde{\mathbf{B}}\,\tilde{f_m}$
$\tilde{\mathbf{y}} = \tilde{\mathbf{C}}\,\tilde{\mathbf{e}}$
end for

Some issues with the proposed algorithm are still open. All sampling frequencies are chosen as uniformly distributed over the entire frequency band, and the total number of POD samples is empircally deduced since the priori knowledge of the system response is unknown. One possible solution to tackle this is to employ the adaptive sampling strategy which will be presented in Chapter 4.

The computational complexity of the proposed BT-POD algorithm are briefly discussed here. The computational cost for the POD sampling is the dominant part, and is estimated to be $2KP \cdot O(N^{1.1-1.3})$ since the iterative solver pMUS [55] is used to solve the forward and adjoint problem for each port and frequency sample. Table 2.1 shows the computational complexity both in time and memory for the most important steps of proposed algorithm.

Table 2.1. BT-POD computational time & memory complexity.

	POD Sampling	SVD	Reduction	Sweep
Time	$2KP\cdot\mathrm{O}(N^{1.3})$	$\mathrm{O}(K^3)$	$K^2\cdot\mathrm{O}(N)+nK^2\cdot\mathrm{O}(N)$	$\mathrm{O}(n^3)$
Memory	$P\mathrm{O}(N)+\gamma\cdot\mathrm{O}(N)$	$\mathrm{O}(K^2)$	$n\cdot\mathrm{O}(N)$	$\mathrm{O}(n^2)$

Electromagnetic information theory suggests that the sampling number $K \propto kD$ where k is the wave number and D denotes the size of TVFEM domain. For three-dimensional problems, the relation between sampling number K (or truncated size n) and the number of DoFs N is

$$K \propto \alpha N^{\frac{1}{3}}$$

$$n \propto \beta N^{\frac{1}{3}}$$

where α, β are very small constant. Therefore the algorithm worst case scaling is $O(N^{1.66})$ in time and $O(N^{1.3})$ in memory.

Although the POD sampling is the dominant time-consuming part, fortunately this part is embarrassingly parallel and without any communication required between different cores. This advantage and the resulting time saving will be presented and verified in the following numerical examples.

2.7 Numerical Results

In this section the numerical results for the wideband frequency parameter sweep via the BT-POD MOR of various TVFEM models will be presented. To illustrate the validity of proposed method, systems with different operation bandwidth and EM boundary conditions will be used. The three representative examples include a narrowband two-port printed microwave filter, a wideband antenna and a wideband infinite array. Alongside to the frequency response, various intermediate algorithm quantities and parameters will be presented to verify the controllable error and numerical efficiency (e.g. serial v.s. parallel run time) of BT-POD.

Throughout this section, the point-by-point TVFEM refers to the direct TVFEM solution at each frequency point with iterative solution tolerence chosen as $\epsilon = 10^{-3}$ except when stated otherwise. The TVFEM iterative solver is based on a hierarchical multigrid (pMUS) method [55]. All serial computations were performed in a PC with 3.2 GHz Intel Pentium dual-core processor and 2 GB RAM. Parallel simulations were performed on a 11 node (88 processor) MacPro cluster with ten 2.8 GHz Xeon quad-core processors and 4 GB RAM per core. All codes were implemented in C++, `gcc` 4.3.3 and the openMPI library on double precision complex arithmetic.

2.7.1 Microstrip Low-pass Filter

The first problem is a microstrip low pass filter that has been numerically and experimentally studied in [56]. This is a classic example, and is used to validate the accuracy of proposed algorithm. Apart from demonstrating the validity of BT-POD,

a study of the effect of HSV truncation tolerance on the overall accuracy will be presented.

The two-port microstrip filter is shown in Figure 2.5 along with the dimensional parameters. The filter is printed on a dielectric with $\epsilon_r = 2.2$ and its response combines both wideband and notch characteristics. The problem is modeled with $80,332$ second-order TVFEM unknowns and first-order absorbing boundary conditions on the top and side boundaries. The s-parameter frequency response of the filter computed by BT-POD are given in Figures 2.6(a) (b) and 2.7(a) (b) when ten uniformly distributed sampling points in the desired frequency range are used. The BT-POD results are compared with the point-by-point TVFEM sweep which is considered the reference. As seen in Figures 2.6-2.7, the results show very good agreement, not only with the point-by-point sweep, but with measurements as well. The measurements deviate from both methods only at the higher frequency region, but such deviation is not surprising since both measurements and simulations have their own limitations in that frequency region (e.g. connectors, discretization, etc). The downward arrows on the horizontal axis indicate the POD frequency sampling (expansion) points used in the integral approximation of the gramians. Embeded in these plots is the result obtained via an adaptive multipoint Krylov algorithm [10]. To study the truncation tolerence effects on the s-parameter error are shown in Figure 2.8, two different tolerences are used ($\epsilon_1 = 10^{-3}$ and $\epsilon_2 = 10^{-7}$). The two cases are plotted in Figure 2.8 where (a) shows the Hankel singular values and respective reduced order size where as (b) depicts the $|s_{11}|$ error v.s. frequency. It is obvious that smaller truncation threshold yields more accurate reduced-order model, thus lower s-parameter errors. The important point in this plot is that the truncation tolerence ϵ is approximately of same order as the error on $|s_{11}|$, which indicates that ϵ can be used as an error indicator. The computational statistics for this simulation is listed in Table 2.2. It

is worth noting that BT-POD is as fast as the adaptive Krylov, but the former does not utilize a adaptive algorithm, that could potentially speed-up the computation.

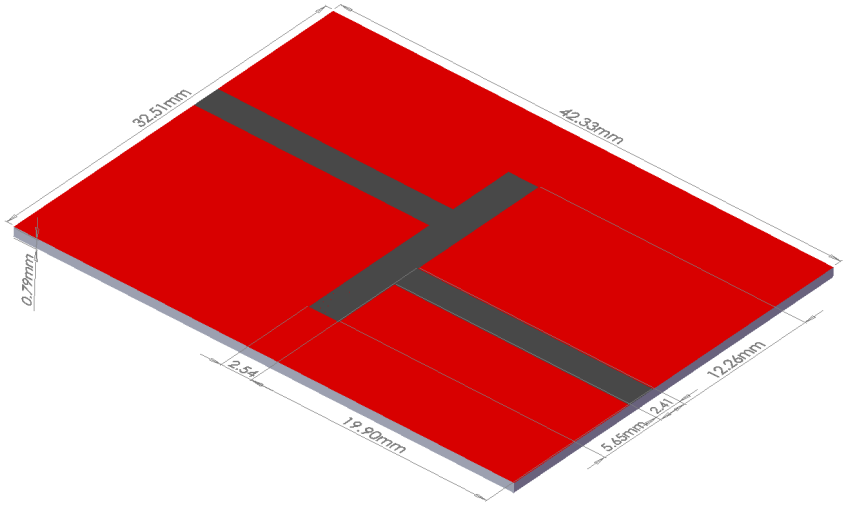

Figure 2.5. 3D geometry and dimensions of microstrip low-pass filter.

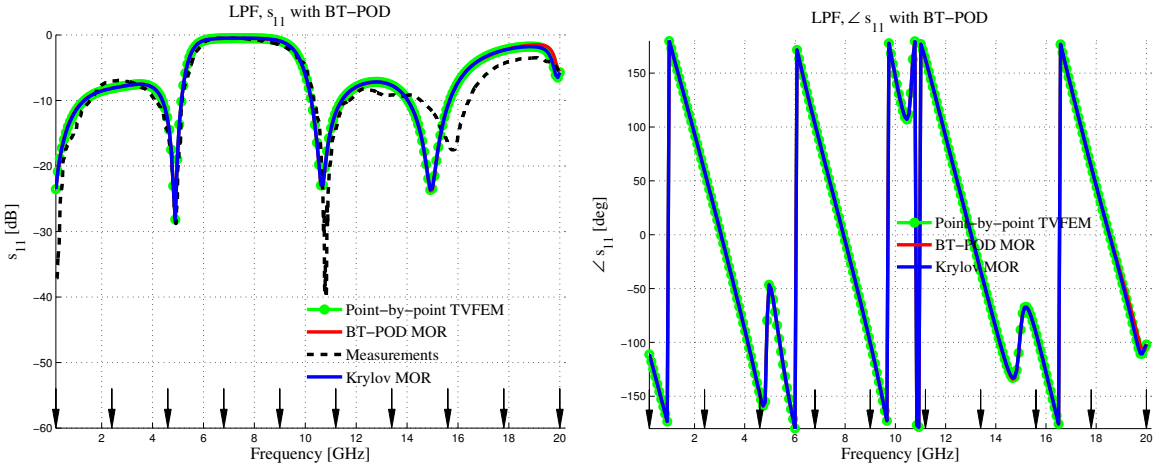

(a) (b)

Figure 2.6. s_{11} frequency response comparison of BT-POD with point-by-point TVFEM sweep, a Krylov MOR and measurements [56]; (a) magnitude; (b) phase.

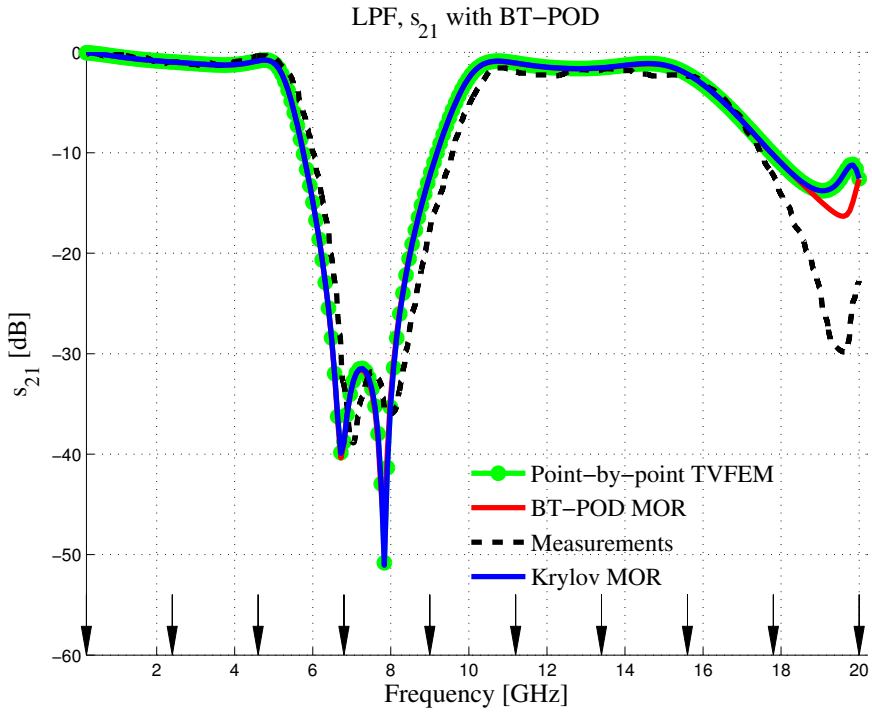

(a)

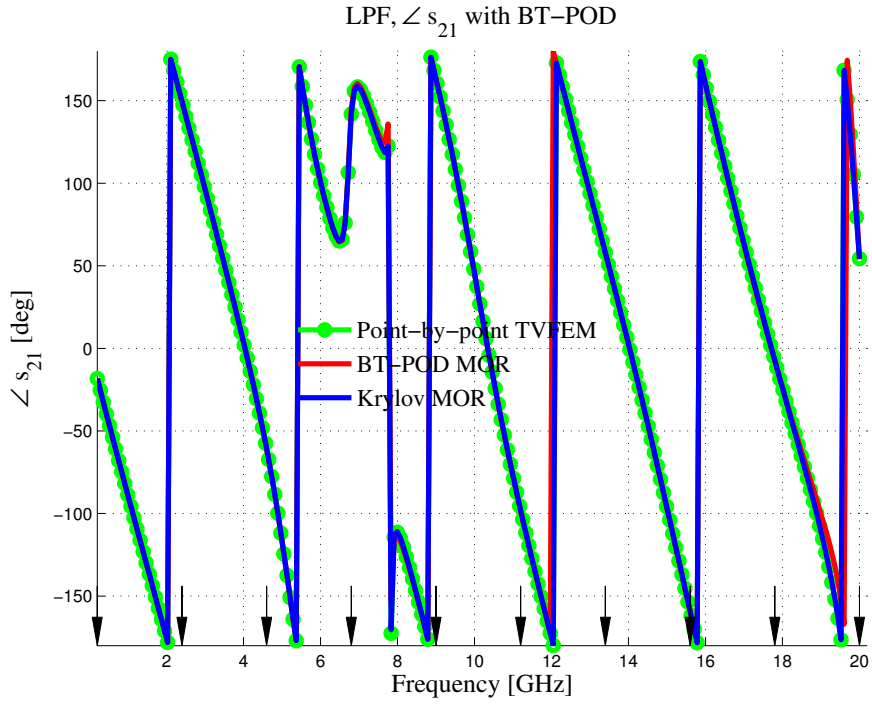

(b)

Figure 2.7. s_{21} frequency response comparison of BT-POD with point-by-point TVFEM sweep, a Krylov MOR and measurements for Microwave low-pass filter in Figure 2.5; (a) magnitude; (b) phase.

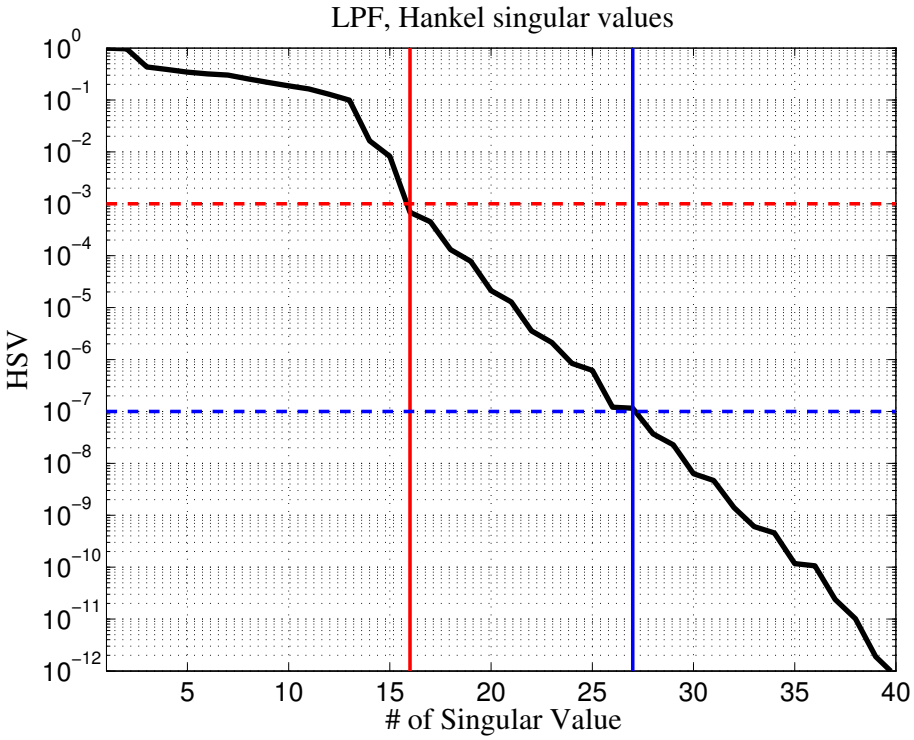

(a)

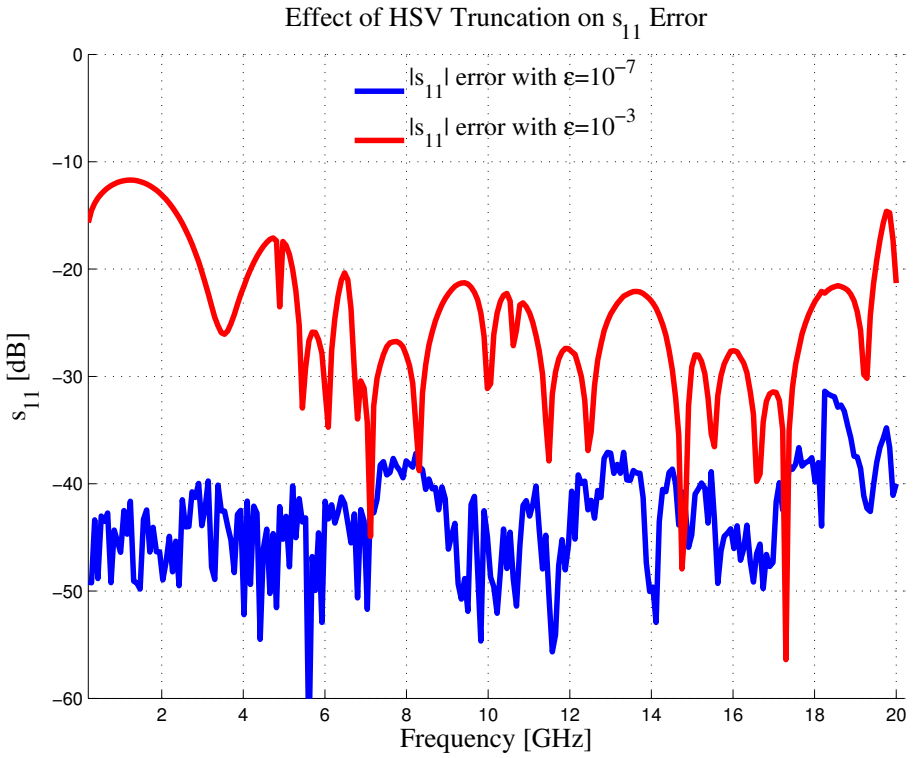

(b)

Figure 2.8. Effects of HSV truncation tolerence on the $|s_{11}|$ error of the microstrip low-pass filter in Figure 2.6(a); (a) Hankel singular values truncation with different tolerence; (b) corresponding $|s_{11}|$ error vs frquency.

Table 2.2. Computational statistics for low-pass filter problem.

Method	Sweep #	Time(hh:mm:ss)	Speedup	Memory
Point-by-point TVFEM	250	0:50:12	-	125 MB
Krylov MOR	250	0:4:59	10.07	75 MB
Serial BT-POD	250	0:4:54	10.24	125 MB

2.7.2 Isolated BAVA Element

In this example, an isolated element of a broadband Balanced Antipodal Vivaldi Antenna (BAVA) is used to demonstrate the numerical performance of BT-POD for radiation problems and to study the effects of different number of POD frequency sampling points on s-parameter error. The simulated structure is adopted from [57] and its geometry and dimensions and material parameters are shown in Figure 2.9. For simulation environment, this antenna is excited by a wave port from the back of the ground plane, and is enclosed by a first-order ABC terminated air box placed at least 2λ away from the element, where λ is the wavelength in free space at highest frequency 8.5 GHz. The entire computational domain is discretized with 462,298 second-order TVFEM unknowns. The s_{11} frequency response of the antenna is given in Figure 2.10(a) and (b), where the point-by-point computation superimposed with the BT-POD results for two different POD sampling (frequency expansion) numbers. It is noted that for only six expansion frequency points the BT-POD is able to capture accurately the response in the entire band $1.5 - 8.5$ GHz. It is worth noting that the peak memory for BT-POD never exceed that required by the point-by-point TVFEM sweep, while the time savings are approximately two orders-of-magnitude. Figure 2.11(a) shows that six POD sampling points can maintain -20dB s_{11} error over the entire 8:1 band. Figure 2.11(b) depicts s_{11} relative error in Hankel norm $\mathcal{H}_2$ vs. POD sampling number, it is observed that the relative error stagnates when the POD sampling number reaches 10, this is believed to be due to the finite tolerance $tol_s = 10^{-3}$ employed in the iterative solution. Detailed computational statistics for

this example are listed in Table 2.3, where both serial and parallel implementations of BT-POD are compared. These results have been obtained using 100 frequency sweep points within the band for both methods. From this table two important conclusions can be drawn (a) BT-POD is orders of magnitude faster than the point-by-point (discrete) sweep, and (b) the parallel scalability for this problem is above 90% for 6 processors.

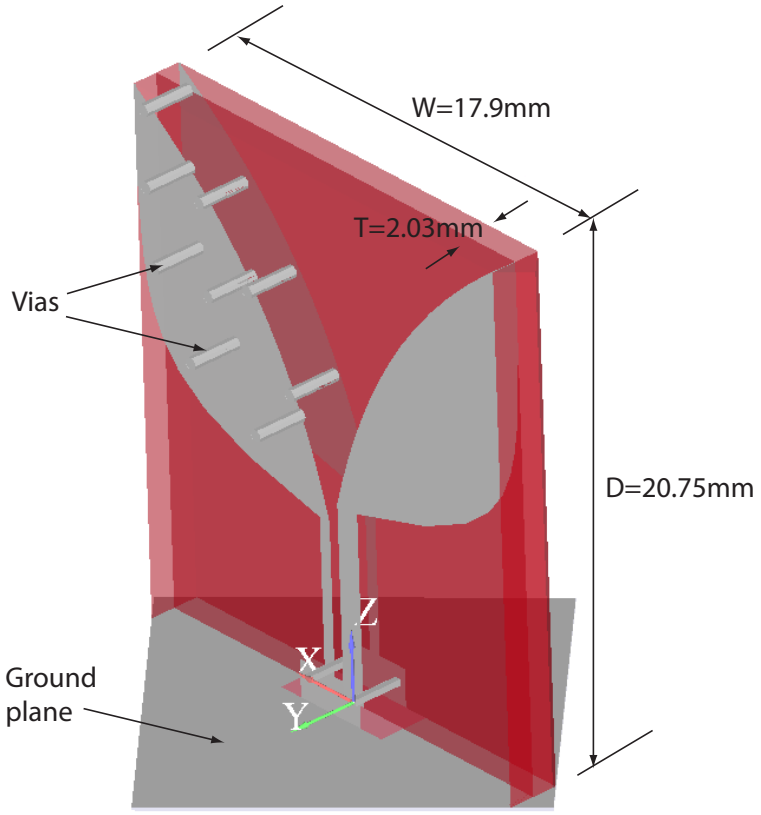

(a)

Figure 2.9. 3D geometry and dimensions of the BAVA

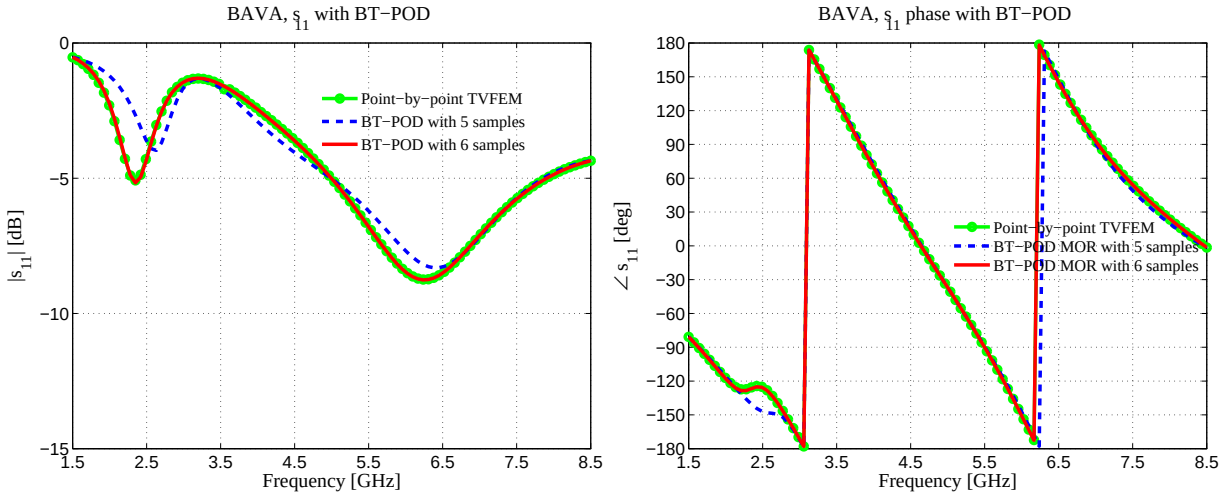

(b) (c)

Figure 2.10. Effect of POD sampling number for an isolated BAVA element example; (a) $|s_{11}|$ vs frquency; (b) BT-POD s_{11} phase vs. frequency.

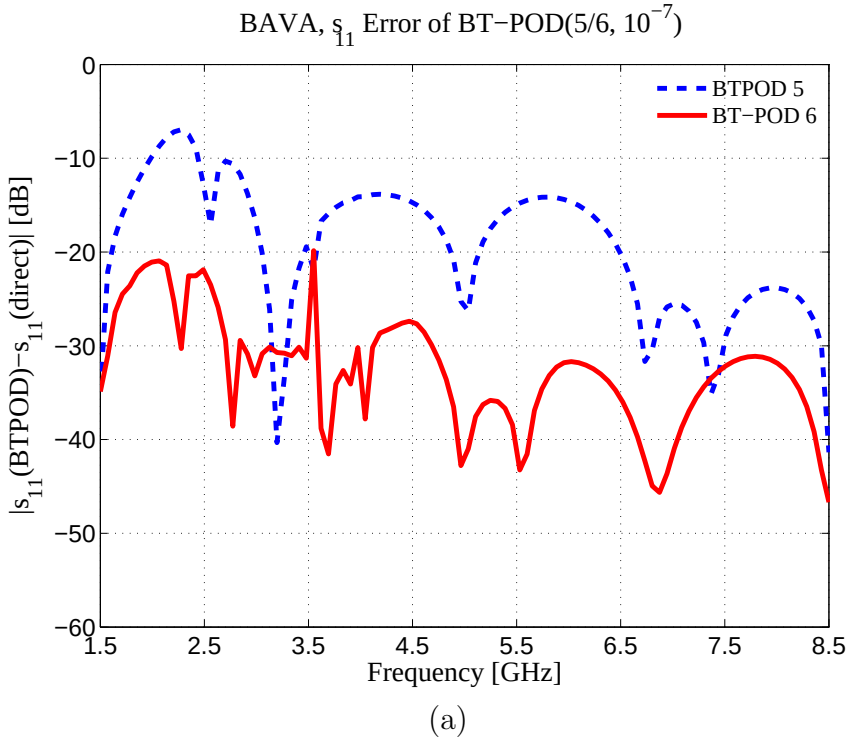

(a)

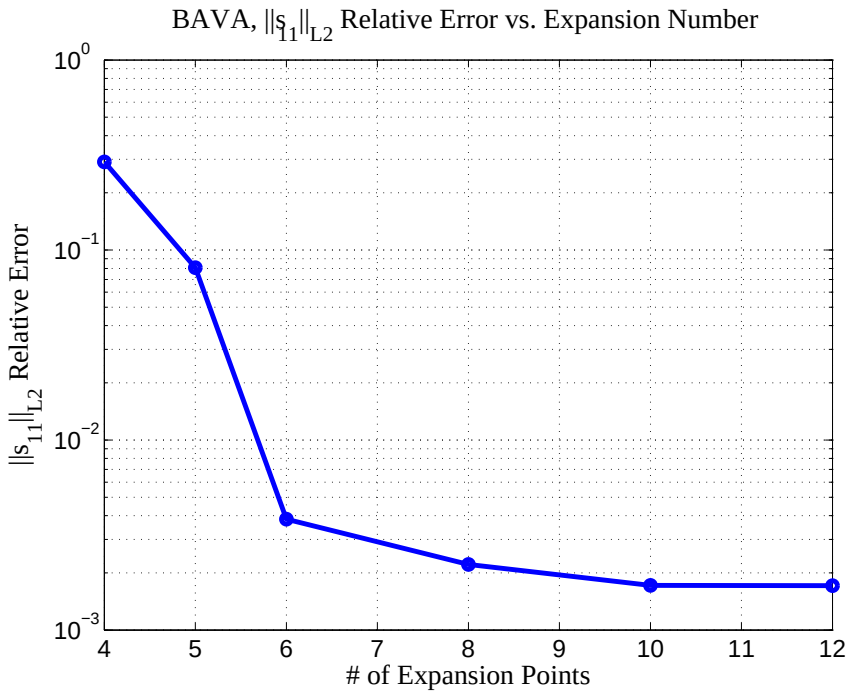

(b)

Figure 2.11. Effect of POD sampling number for an isolated BAVA element; (a) $|s_{11}|$ error vs. frequency; (b) BT-POD $\mathcal{H}_2$ error of $|s_{11}|$ vs. sample point number.

Table 2.3. Computational statistics for BAVA problem.

Method	Time(hh:mm:ss)	Speedup	Memory
Point-by-point TVFEM Sweep	t_{FEM} = 11:38:40	-	825MB
Serial BT-POD	t_s = 00:42:05	$t_{FEM}/t_s = 16.60$	825MB
Parallel BT-POD	t_p = 00:07:41	$t_s/t_p = 5.48$	825MB×6

2.7.3 Infinite Vivaldi Array

The final example is used to demonstrate the versatility of BT-POD to various EM boundary conditions and non-LTI systems through the simulation of the radiation by an infinite Vivaldi array. In this problem, the effects of the iterative solver tolerance and POD sampling points choice on the s_{11} error will be studied. To the best of our knowledge, this is the first time that MOR is used to speed-up simulations of 3D infinite periodic structures. An infinite periodic problem is modeled using periodic boundary conditions that are highly dispersive [50] and do not comply with the LTI system theory, thus traditional MOR methods fail to predict the dynamic behavior of such systems. On the other hand, BT-POD appears to work very well on such system because of its simple POD sampling approach and its reliance on system gramians and Hankel singular values instead of system eigenvalues.

The simulated array structure is shown in Figures 2.12(a) and (b). The infinite array is modeled with non-conforming mesh periodic boundary conditions adopted from [50]. The total number of second-order TVFEM unknowns in the computational domain is 158,024 and ABC BCs is used at the top boundary. A number of experiments are presented to demonstrate the benefits of proposed methodology. A plot of the active reflection coefficient versus frequency is plotted over three octaves of bandwidth in Figure 2.13(a). The figure shows the reference response along with two 8 POD samples results, one obtained via iterative tolerence chosen as $tol_s = 10^{-3}$ and the other with $tol_s = 10^{-2}$. It is noted that very good accuracy is achieved with only eight expansion (sample) frequency points and iterative solver tolerance of 10^{-3}. The

fact that even high iterative solver tolerance values, e.g. 10^{-2}, are able to predict the response at most of the frequency band was a pleasant surprise, that will be further explored in future studies. A similar error study of s_{11} relative error on $\mathcal{H}_2$ vs. POD sampling number was also performed as shown in Figure 2.13(b). Figures 2.14(a) and (b) show the effects of the iterative solver tolerance and number of sampling points on the decay rate of Hankel singular values (HSVs), where the reference result was obtained with iterative tolerance 10^{-4} and 20 POD sampling points. These figures indicate that approximately eight sampling points are enough to produce stable HSVs above 10^{-3}, which is in agreement with the conclusions of Figure 2.13(b). This hinges on the fact that the decay of the Hankel singular values, that are available before the reduction process, can be used as error estimators in an adaptive sampling approach. Computational statistics from this section are listed in Table 2.4, for a 100 point frequency sweep. It should be remarked that the parallel scalability reduces to 63% whereas the results of the BAVA example (Table 2.3) gave 91%. This is because at low frequency ($1 - 2$ GHz) the employed iterative method takes longer time to converge at desired tolerence, therefore the parallel load balancing is disturbed.

Table 2.4. Computational statistics for infinite Vivaldi array problem.

Method	Time(hh:mm:ss)	Speedup	Memory
Point-by-point TVFEM Sweep	t_{FEM} = 03:36:04	-	729MB
Serial BT-POD	t_s = 00:19:21	$t_{FEM}/t_s = 11.7$	729MB
Parallel BT-POD	t_p = 00:03:49	$t_s/t_p = 5.06$	729MB × 8

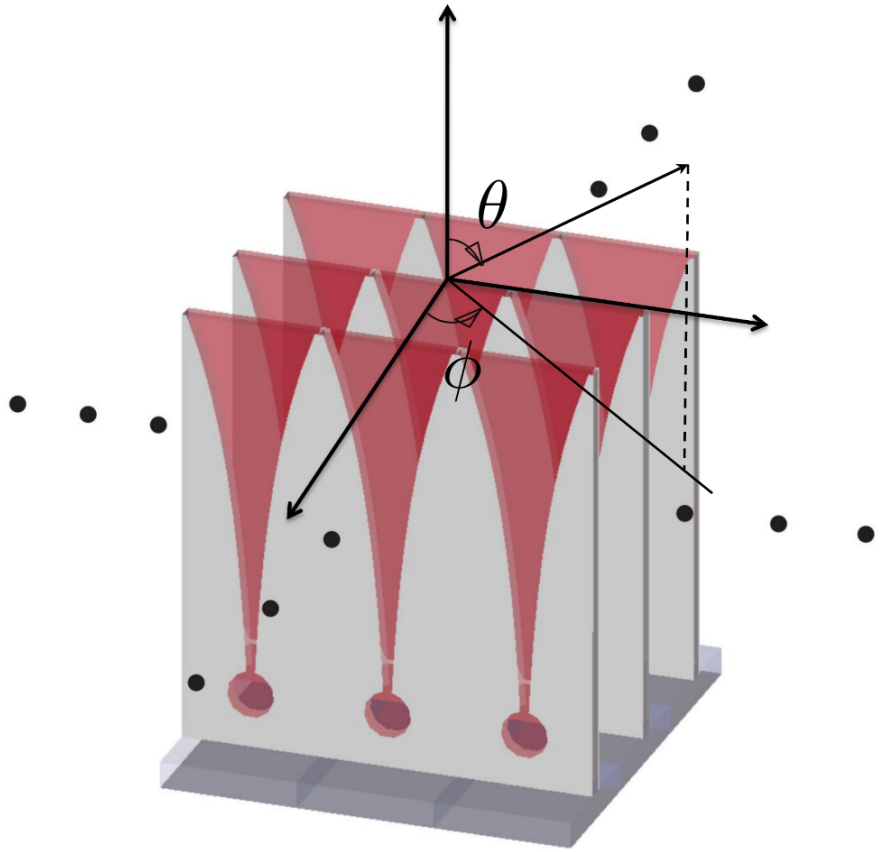

(a)

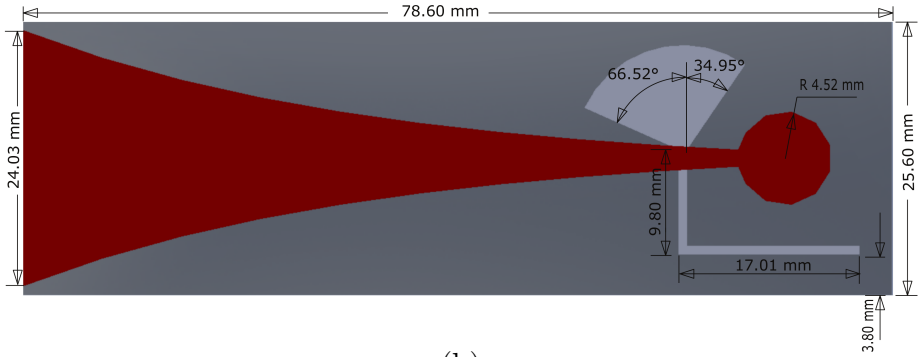

(b)

Figure 2.12. Infinite single-polarized Vivaldi array geometry adopted from [58]; (a) 3D array and scanning arrangement; (b) element geometry and dimensions.

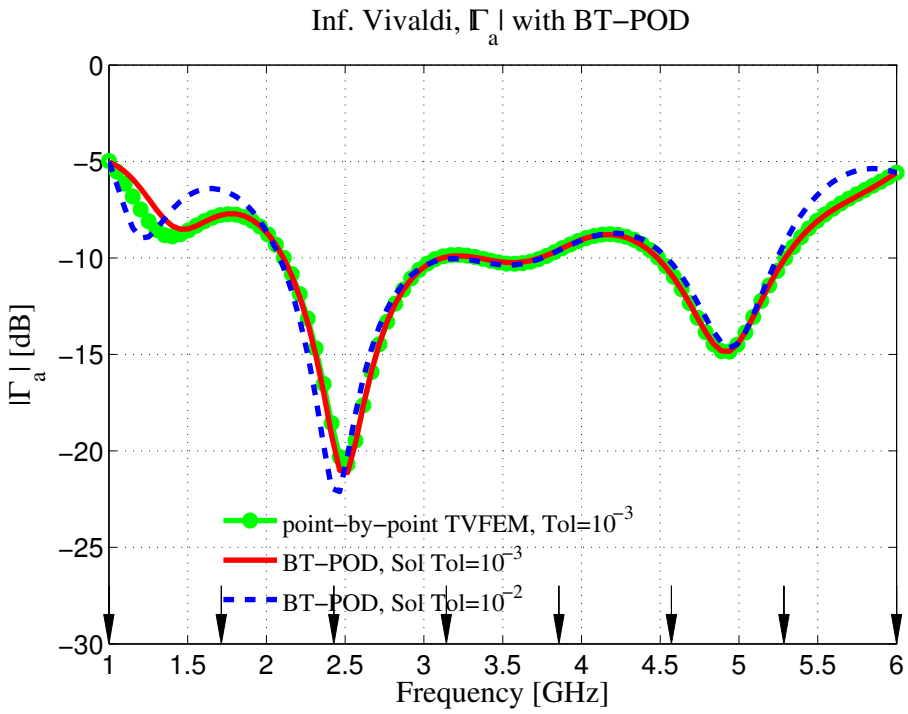

(a)

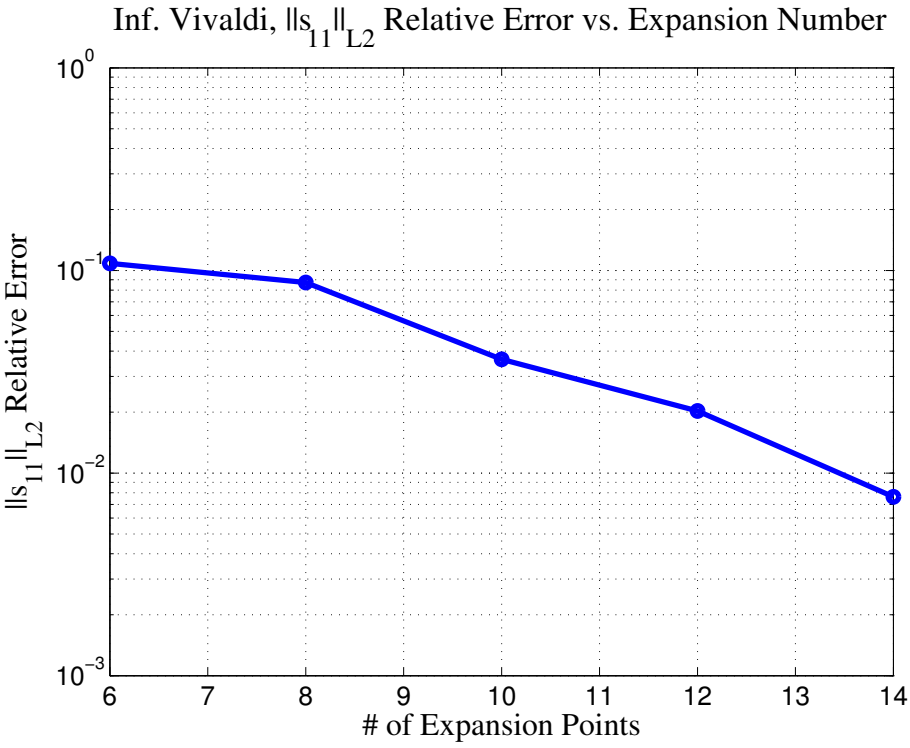

(b)

Figure 2.13. BT-POD accuracy on the infinite single-polarized Vivaldi array; (a) Comparison of $|\Gamma_a|$ vs. frequency; (b) $\|\Gamma_a\|_{\mathcal{H}2}$ relative error vs. expansion points.

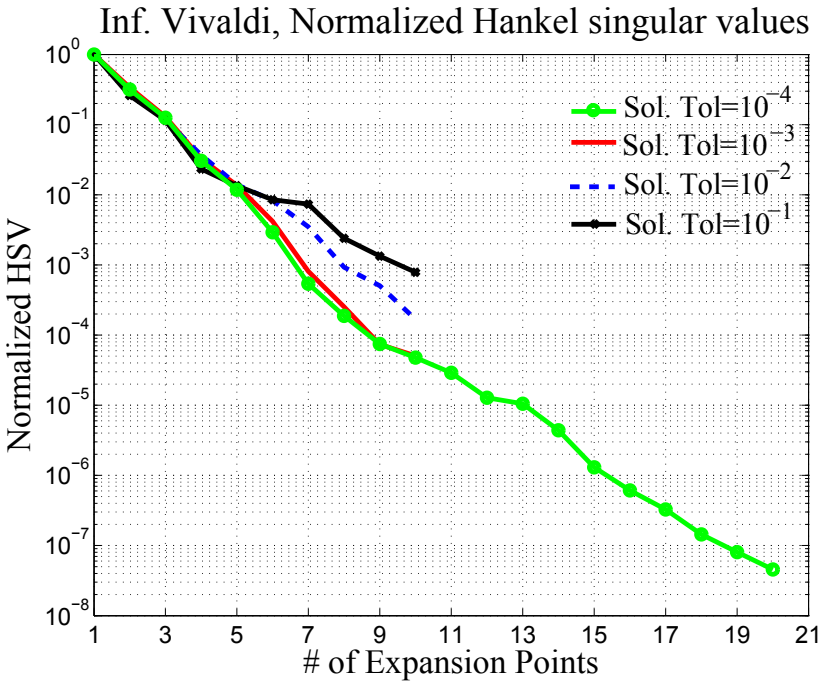

(a)

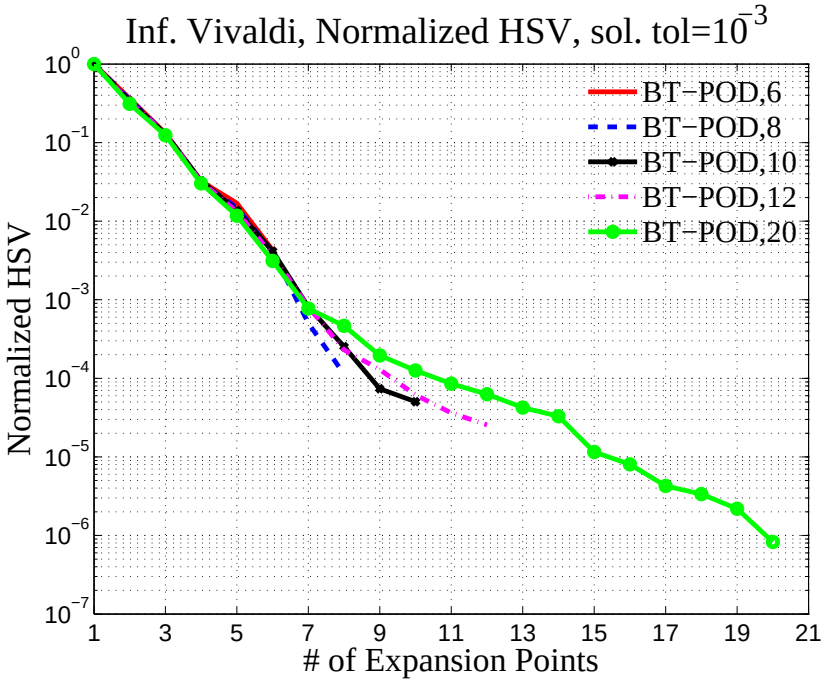

(b)

Figure 2.14. Hankel singular values (HSV) of the infinite Vivaldi array example; (a) effect of iterative solver tolerance on HSVs; (b) effect of sample point number on HSVs.

CHAPTER 3

MULTI-PARAMETER BT-POD

In the design and optimization of microwave/RF systems such as antennas or microwave circuits, various design parameters including material permittivity and permeability, or antenna excitation parameters such as scan angles are used to meet design specifications. This design and optimization process usually involves repeatedly solving the EM system with many different parameter values which will tremendously prolong the simulation time.

In this chapter, the BT-POD algorithm will be extended to accomodate multi-parameter models where frequency, materials and scan angles are varied concurrently. The multi-parameter space sweep is achieved in a two step process: (1) An off-line stage where coarse parameters space sampling is used to produce the multi-dimensional balancing transformations, and (2) an on-line stage that parameters space sweep via the solution of the reduced model. It is believed that the multi-parametric BT-POD MOR technique will significantly speed-up engineers to design and optimize high-frequency electromagnetic systems.

Multi-parameter model reduction in EM has been an active research area. In [44], Weile et al proposed a two-parameter sweep technique that is based on Krylov MOR. In [45], they utilized this method to analyze frequency-selective surface with frequency and incident angle parameters. Farle et al. applied a multi-dimensional Krylov MOR [46] to perform frequency and material spaces sweep.

In this work, a sharp contrast from previous multi-parameter MOR is that, the reduction process will be translated into a numerical integration over a multi-dimensional

space. Therefore this MOR paradigm can be extended to multi-dimensional spaces through the use of simple or specialized numerical quadratures in high dimensions. For example, some advanced multi-dimensional numerical integration methods such as Monte-Carlo [59] or sparse grid integration rules [60] can be incorporated with the multi-parametric BT-POD technique thus tremendously enhance its performance.

In this chapter, only simple tensor product numerical quadratures will be used for POD sampling. Numerical experiments will include an infinite Vivaldi array problem and an infinite PUMA array problem to demonstrate the validity and efficiency of the multi-parameter BT-POD.

3.1 Multi-Parametric BT-POD Model Reduction

3.1.1 Parameterized TVFEM Model

The TVFEM model presented in Chapter 2 is parameterized with respect to frequency (s) multiplying constant matrices, therefore it can not be used for excitation angle (θ, ϕ) and material (ϵ, μ) sweeps. In order to perform multi-parametric sweep, all TVFEM matrices become parameters independent, therefore one must consider the model,

$$[\mathbf{M}(s, \boldsymbol{\epsilon}') + \mathbf{D}(s, \boldsymbol{\epsilon}'') + \mathbf{S}(\boldsymbol{\mu}) + \mathbf{T}(s, \boldsymbol{\beta})]\, \mathbf{e}(s, \boldsymbol{\epsilon}', \boldsymbol{\epsilon}'', \boldsymbol{\mu}, \boldsymbol{\beta}) = \mathbf{C}(s, \boldsymbol{\epsilon}')\, \mathbf{f}, \tag{3.1}$$

where $\boldsymbol{\epsilon}'$, $\boldsymbol{\epsilon}''$, $\boldsymbol{\mu}$, and $\boldsymbol{\beta}$ are the parameter space,

$$\begin{aligned}
\boldsymbol{\epsilon}' &= \{\epsilon'_1, \epsilon'_2, \cdots, \epsilon'_M\} \\
\boldsymbol{\epsilon}'' &= \{\epsilon''_1, \epsilon''_2, \cdots, \epsilon''_M\} \\
\boldsymbol{\mu} &= \{\mu_1, \mu_2, \cdots, \mu_M\} \\
\boldsymbol{\beta} &= \{\theta, \phi\}
\end{aligned}$$

where M is the number of material regions where the material permittivity and permeability of that region is $\epsilon_m = \epsilon'_m - j\epsilon''_m$ and μ_m, $m = 1, 2, \cdots, M$. $\boldsymbol{\beta}$ is the scanning direction of an infinite phased array. It is being noted that the periodic boundary conditions of the periodic TVFEM [50] has been added ($\mathbf{T}$) to takes account of periodic structure EM modeling problems, an explicit form of $\mathbf{T}$ can be found in [50].

Therefore, a parameterized TVFEM model is achieved as

$$\left[s^2 \sum_{m=1}^{M} \epsilon'_m \mathbf{M}_m + s \sum_{m=1}^{M} \epsilon''_m \mathbf{D}_m + \sum_{m=1}^{M} \frac{1}{\mu_m} \mathbf{S}_m + e^{\pm s\,\boldsymbol{\beta}\cdot\mathbf{d}}\, \mathbf{T} \right] \mathbf{e}(s, \boldsymbol{\epsilon'}, \boldsymbol{\epsilon''}, \boldsymbol{\mu}, \boldsymbol{\beta}) = \mathbf{C}(s, \boldsymbol{\epsilon'})\, \mathbf{f}, \tag{3.2}$$

where

$$\begin{aligned}
(\mathbf{M}_m)_{ij} &= \frac{1}{c^2} \int_{\Omega_m} \mathbf{w}_j \cdot \mathbf{w}_i \, dr^3, \\
(\mathbf{D}_m)_{ij} &= \frac{1}{c} \oint_{\partial\Omega_m} \hat{\mathbf{n}_m} \times \mathbf{w}_j \cdot \hat{\mathbf{n}_m} \times \mathbf{w}_i \, dr^2, \\
(\mathbf{S}_m)_{ij} &= \int_{\Omega_m} \nabla \times \mathbf{w}_j \cdot \nabla \times \mathbf{w}_i \, dr^3,
\end{aligned}$$

where Ω_m is the region occupied by material (ϵ_m, μ_m). $\mathbf{d}$ is the displacement of two adjacent domains along the direction of the infinite periodicity. Figure 3.1 briefly illustrates the partition of the FE mass matrix $\mathbf{M}$ when $M = 3$. Following such approach, instead of performing reduction on FE matrices $\mathbf{S}, \mathbf{D}, \mathbf{M}$ in previous chapter, each FE matrix in (3.2) need to be reduced such that a multi-parametric sweep can be achieved.

3.1.2 Multi-Parameter Space System Gramians Approximation

As stated in chapter 2, TVFEM system gramians are approximated through numerical quadratures over the frequency bandwidth of interest which can be found in (2.26)-(2.28). In the previous chapter, this integration is performed in 1D Laplace

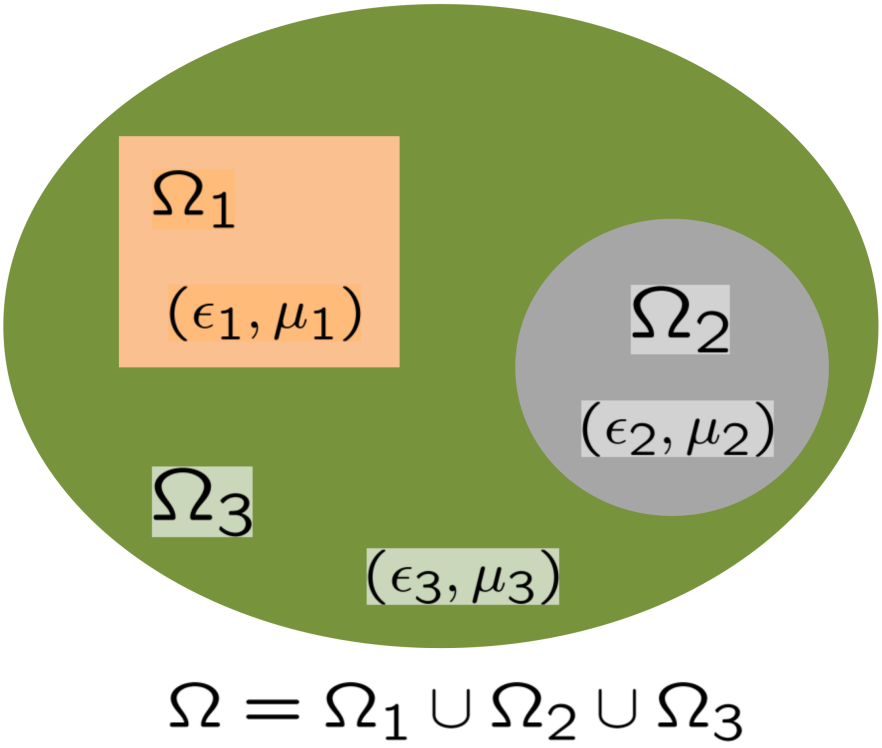

(a)

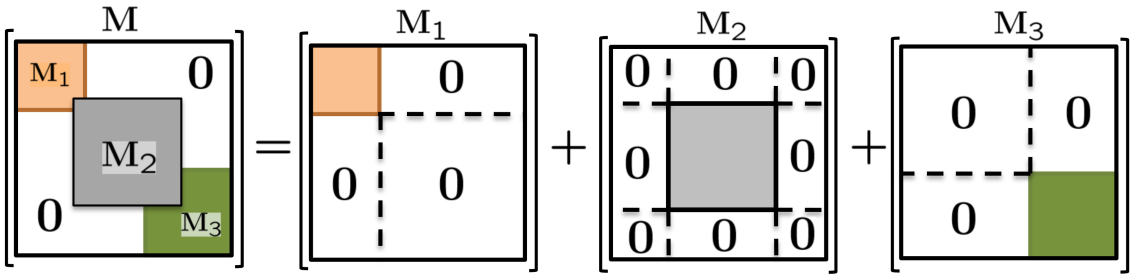

(b)

Figure 3.1. A computational domain Ω partitioned by three material regions $\Omega_i (i = 1, 2, 3)$ and the corresponding partition of the mass matrix $\mathbf{M}$ in the parameterized model; (a) domain partition; (b) mass matrix partition.

frequency s-domain as shown in Figure 3.2(a). This concept can be extended to multiple dimensions through the use of simple tensor product. A multi-dimensional quadratures as shown in Figures 3.2(b) and (c) over the range of parameters of interests.

Based on Lemma 2.2.1, the system gramians in a 3D parameter space of interest (s, ζ, η) can be defined as

$$\begin{aligned} \boldsymbol{\mathcal{P}} &= k \int_0^{\infty} \int_0^{\infty} \int_0^{j\infty} \mathbf{H}(s,\zeta,\eta)\mathbf{H}^*(s,\zeta,\eta)\, ds\, d\zeta\, d\eta, \\ \boldsymbol{\mathcal{Q}} &= k \int_0^{\infty} \int_0^{\infty} \int_0^{j\infty} \mathbf{H}_a^*(s,\zeta,\eta)\mathbf{H}_a(s,\zeta,\eta)\, ds\, d\zeta\, d\eta \end{aligned} \tag{3.3}$$

where k is a constant scalar, ζ, η can be the material parameters or scan angles. $\mathbf{H}(s, \zeta, \eta)$ and $\mathbf{H}_a(s, \zeta, \eta)$ are the transfer functions from the forward and adjoint form of the original problems. Similar to Chapter 2, the integrations are evaluated with simple Reimannian quadratures, but in the tensor product form. These quadratures require the evaluation of $\mathbf{H}(s,\zeta,\eta)\mathbf{H}^*(s,\zeta,\eta)$ and $\mathbf{H}_a^*(s,\zeta,\eta)\mathbf{H}_a(s,\zeta,\eta)$ at each discrete parameter spaces position $(s_k, \zeta_i, \eta_j), k = 1, 2, \cdots, K, i = 1, 2, \cdots, I, j = 1, 2, \cdots, J$, where K, I, J are the total number of POD sampling points along each parameter space. Therefore, the multi-parameter TVFEM system gramians $\tilde{\boldsymbol{\mathcal{P}}}$ and $\tilde{\boldsymbol{\mathcal{Q}}}$ in (3.3) are

$$\begin{aligned} \tilde{\boldsymbol{\mathcal{P}}} &= k\Delta V \sum_{k=1}^{K} \sum_{i=1}^{I} \sum_{j=1}^{J} \mathbf{H}(s_k,\zeta_i,\eta_j)\mathbf{H}^*(s_k,\zeta_i,\eta_j) \\ \tilde{\boldsymbol{\mathcal{Q}}} &= k\Delta V \sum_{k=1}^{K} \sum_{i=1}^{I} \sum_{j=1}^{J} \mathbf{H}_a^*(s_k,\zeta_i,\eta_j)\mathbf{H}_a(s_k,\zeta_i,\eta_j) \end{aligned} \tag{3.4}$$

where $\Delta V = \Delta s\, \Delta\zeta\, \Delta\eta$, Δs, $\Delta\zeta$ and $\Delta\eta$ are the discretization grid length over parameter space s, ζ, and η, respectively.

Figures 3.2(a)-(c) briefly illustrate the integration strategy employed in this approach, where 1D frequency expansion locations in Figure 3.2(a) are denoted by red arrows, 2D frequency-material expansion points with red arrows shown in Figure 3.2(b), and dots in Figure 3.2(c) mean the (s, ζ, η) expansion location in 3D space. For the purpose of visibility, dots in the same ζ-η plane are marked with the same color.

Similar to (2.28), the approximated gramians in (3.4) are expressed in the matrix form

$$\begin{aligned} \tilde{\boldsymbol{\mathcal{P}}} &= \mathbf{U}\mathbf{U}^* \\ \tilde{\boldsymbol{\mathcal{Q}}} &= \mathbf{L}^*\mathbf{L} \end{aligned} \tag{3.5}$$

where the low-rank Choleski factor $\mathbf{U}$ and $\mathbf{L}$ are given by

$$\mathbf{U} = \sqrt{k\Delta V}[\mathbf{H}(s_1, \zeta, \eta)\ \ \mathbf{H}(s_2, \zeta, \eta)\ \ \cdots\ \ \mathbf{H}(s_K, \zeta, \eta)] \in \mathbb{C}^{N\times(KP\cdot I\cdot J)},$$

and

$$\mathbf{L} = \sqrt{k\Delta V}[\mathbf{H}_a(s_1, \zeta, \eta)\ \ \mathbf{H}_a(s_2, \zeta, \eta)\ \ \cdots\ \ \mathbf{H}_a(s_K, \zeta, \eta)] \in \mathbb{C}^{N\times(KP\cdot I\cdot J)},$$

where

$$\begin{aligned} \mathbf{H}(s_k, \zeta, \eta) &= [\mathbf{H}(s_k, \zeta_1, \eta_1)\ \mathbf{H}(s_k, \zeta_1, \eta_2)\ \cdots \mathbf{H}(s_k, \zeta_2, \eta_1)\ \cdots \mathbf{H}(s_k, \zeta_I, \eta_J)], \\ \mathbf{H}_a(s_k, \zeta, \eta) &= [\mathbf{H}_a(s_k, \zeta_1, \eta_1)\ \mathbf{H}_a(s_k, \zeta_1, \eta_2)\ \cdots \mathbf{H}_a(s_k, \zeta_2, \eta_1)\ \cdots \mathbf{H}_a(s_k, \zeta_I, \eta_J)]. \end{aligned}$$

for $k = 1, 2, \cdots, K$. Therefore the Hankel matrix with respect to parameter spaces (s, ζ, η) is constructed through

$$\boldsymbol{\mathcal{H}} = \mathbf{U}^*\mathbf{L} \in \mathbb{C}^{(K\cdot P\cdot I\cdot J)\times(K\cdot P\cdot I\cdot J)}$$

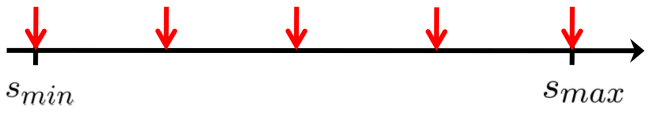

(a)

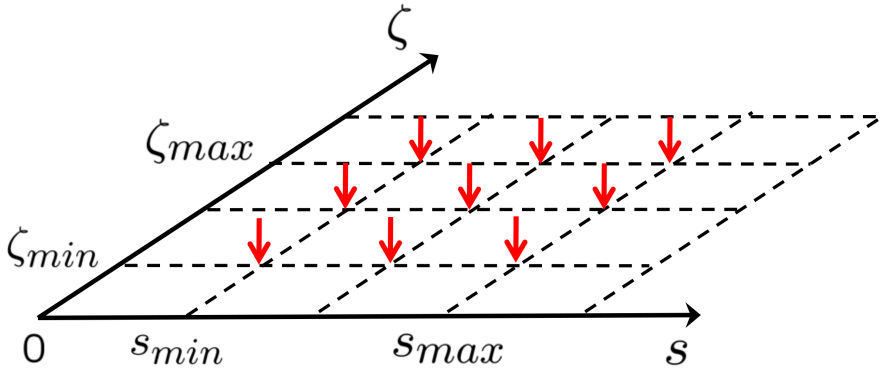

(b)

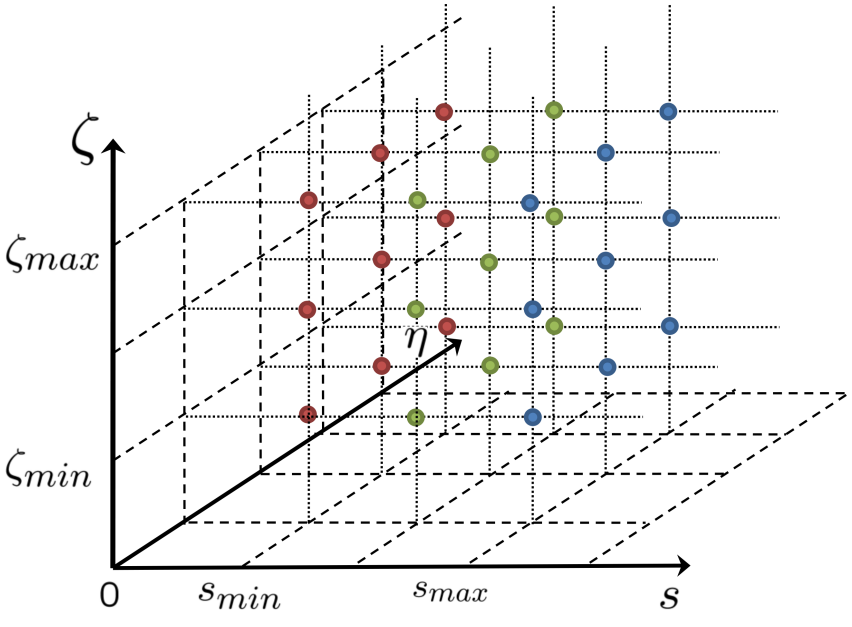

(c)

Figure 3.2. Illustration of the POD sampling over (a) 1D frequency axis; (b) 2D (f, ϵ) parameter spaces; (c) 3D (s, ζ, η) paramters spaces.

With this Hankel matrix the balanced truncation (2.31) and reduction steps described in sections 2.4 are used to obtain the reduced matrices $\tilde{\mathbf{S}}$, $\tilde{\mathbf{D}}$, $\tilde{\mathbf{M}}$, and $\tilde{\mathbf{C}}$. The final multiparametric reduced model used in the sweep part is given by

$$\left[s^2 \sum_{m=1}^{M} \epsilon'_m \tilde{\mathbf{M}}_m + s \sum_{m=1}^{M} \epsilon''_m \tilde{\mathbf{D}}_m + \sum_{m=1}^{M} \frac{1}{\mu_m} \tilde{\mathbf{S}}_m + e^{\pm s\,\boldsymbol{\beta}\cdot\mathbf{d}}\, \tilde{\mathbf{T}} \right] \tilde{\mathbf{e}}(s, \boldsymbol{\epsilon}', \boldsymbol{\epsilon}'', \boldsymbol{\mu}, \boldsymbol{\beta}) = \tilde{\mathbf{C}}(s, \boldsymbol{\epsilon}')\, \tilde{\mathbf{f}} \tag{3.6}$$

3.2 Numerical Results

In this section, two illustrative numerical examples of the multi-parameter BT-POD algorithm are presented. The first example involves the frequency and scan angles (f, θ, ϕ) multi-parametric sweep of an infinite Vivaldi array model, while the second one involves the multiple material and frequency $(\epsilon_{r1}, \epsilon_{r2}, f)$ sweep of a planar ultra wideband array model. Through this section the reference result will be the point-by-point periodic TVFEM sweep that requires an individual solution at every combination point in the 2D parameter space (f, ϵ) or 3D space (f, θ, ϕ). All serial computation were performed in a PC with 3.2GHz Intel Pentium dual-core processor with 2GB RAM, while the parallel computing were performed on an Apple MacPro cluster with eleven nodes of two 3.2GHz Xeon quad-core processors and 352GB distributed RAM. All codes were implemented in C++ and compiled by `gcc` 4.3.3.

3.2.1 Infinite Vivaldi Array

This section will describe the performence of the multiparameter BT-POD when frequency and θ and ϕ angles of the infinite Vivaldi array problem which has been described in the previous chapter is considered. The operating bandwidth of interest is 1-6 GHz, and the scanning varies from $\phi = 0^\circ$ to 90° and $\theta = 0^\circ$ to 60°. The POD expansion points for all the three parameters are uniformly distributed in a tensor product fashion along the ranges of interest, and the number of samples along each dimension are given in Table 3.1. The decay of Hankel singular values (HSVs) is

shown in Figure 3.3. In this simulation, the HSVs truncation tolerance was chosen as $\epsilon = 10^{-8}$, and it is observed that the dominant modes from HSVs are retained in the reduced model (reduced size=128). The H-plane ($\phi = 0°$) VSWR and the active reflection coefficient phase results from the fast parametric sweep are shown in Figures 3.4(a)-(b), while the point-by-point periodic-cell TVFEM results performed as $\Delta\theta = 5°$ are plotted in Figures 3.4(c)-(d). As shown in the figures, the multi-dimensional BT-POD accurately predicts the active reflection coefficient of the array over the entire frequency and angle spectrum. To verify this, the absolute error compared with the point-by-point periodic-cell TVFEM is plotted in Figure 3.5. It should be noted that BT-POD captures the sharp H-plane resonance at 4.5GHz (Figure 3.4(a)), since no vias were used across the fins of the Vivaldi model. This was intentionally done so evaluate the accuracy of BT-POD in cases where sharp resonances are present. The VSWR and the phase of active reflection coefficient of the Vivaldi array at $\phi = 30°$, $45°$ and $90°$ are shown in Figure 3.6. The computational statistics of the serial BT-POD compared with the traditional point-by-point periodic TVFEM method are shown in Table 3.2. It is worth noting that three orders of magnitude speed improvement was achieved. It is also observed that the achieved speedup from parallel computing is quite small in terms of the total number of cores, this is because the construction of transformation matrices and system reduction are not performed by parallel computing while these two steps take most of the time of the entire simulation. It should be remarked that the wall time for point-by-point simulation is only estimated from a smaller simulation of (θ, f) (see Figure 3.4(a)).

Table 3.1. BT-POD sampling parameters for the infinite Vivaldi array example.

	f	θ	ϕ
# of POD samples	8	4	5
# of sweep points	101	61	91

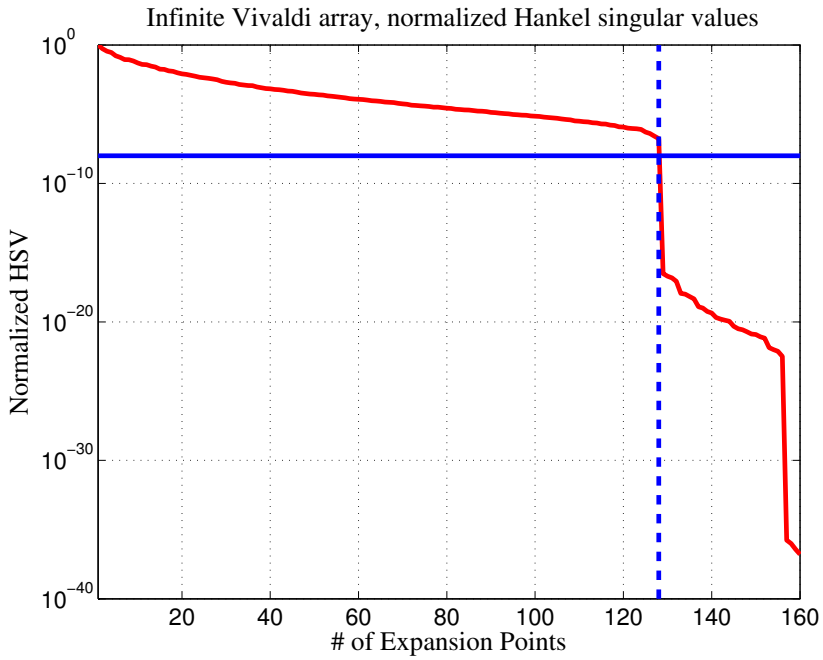

Figure 3.3. Normalized Hankel singular values (HSVs) of infinite Vivaldi array, HSVs truncation tolerance $\varepsilon = 10^{-8}$.

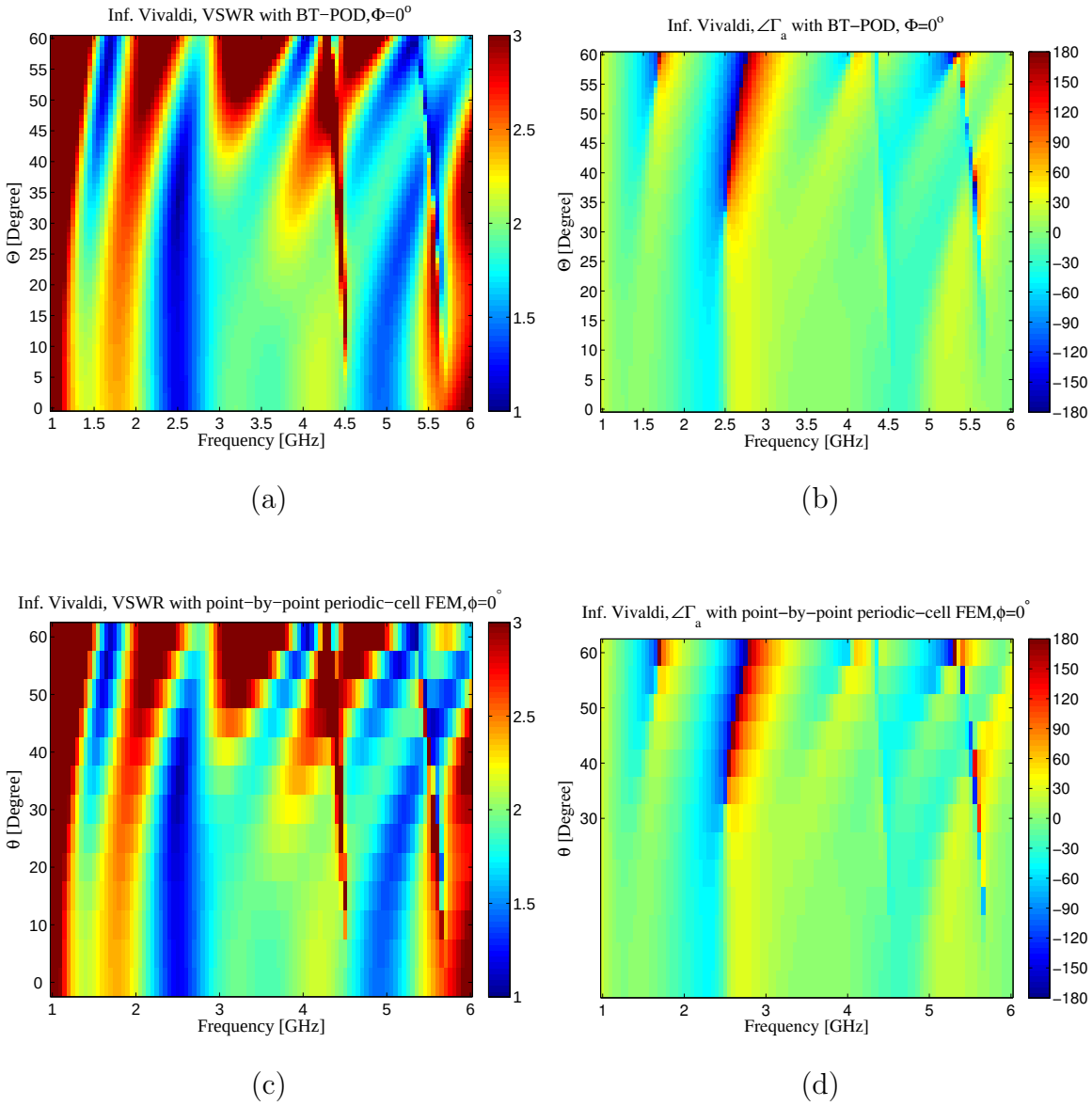

Figure 3.4. Comparison of (f, θ) sweep between the multi-parameter BT-POD and point-by-point periodic-cell TVFEM for the infinite Vivaldi array example at $\phi = 0°$; (a) VSWR vs.(f, θ) via BT-POD; (b) Phase vs.(f, θ) via BT-POD (c) VSWR vs (f, θ) via point-by-point periodic-cell TVFEM ; (d) Phase vs. (f, θ) via point-by-point periodic-cell TVFEM.

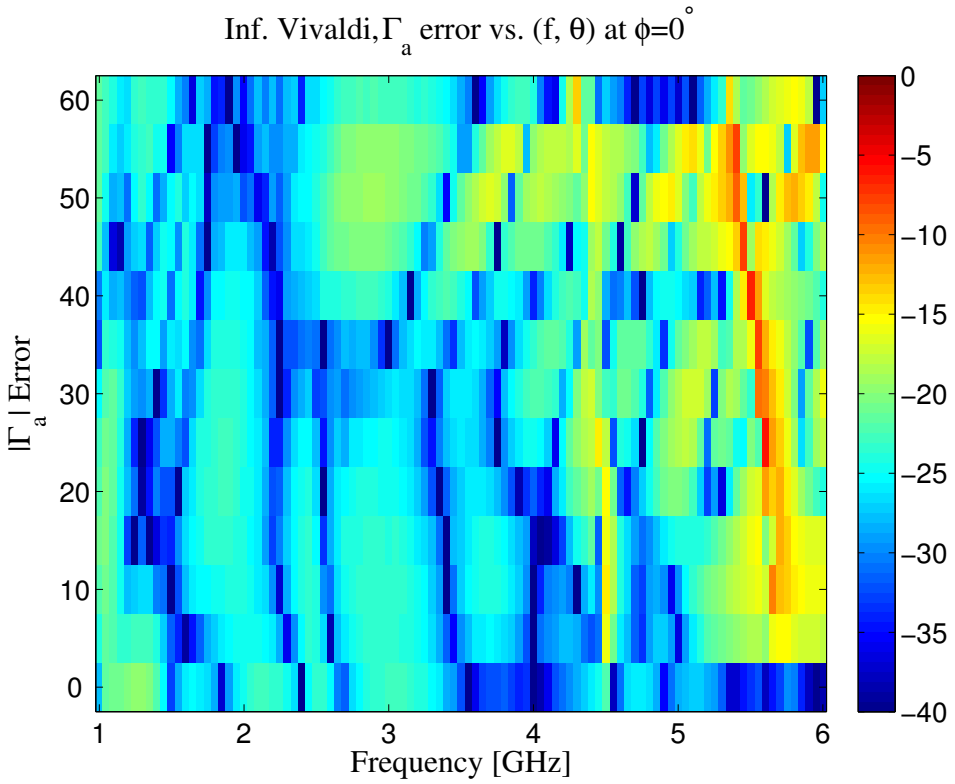

Figure 3.5. Active reflection coefficient $|\Gamma_a|$ error [dB] vs. (f, θ) with Δf=50 MHz, $\Delta\theta = 5°$ for the infinite Vivaldi array example.

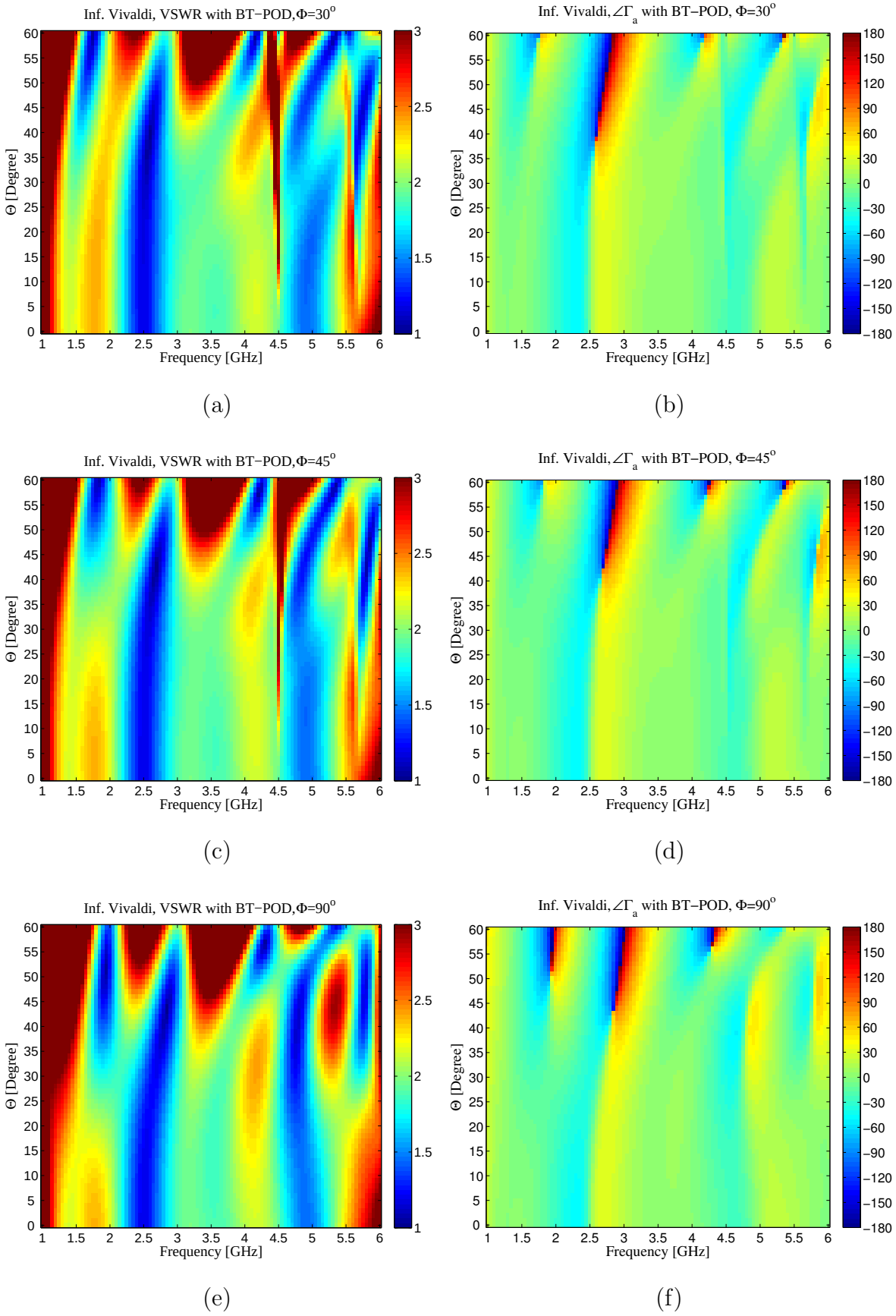

Figure 3.6. Three-parameter BT-POD sweep on (f, θ, ϕ) for the infinite Vivaldi array example; (a) VSWR at $\phi = 30°$; (b) Γ phase at $\phi = 30°$; (c) VSWR at $\phi = 45°$; (d) Γ_a phase at $\phi = 45°$; (e) VSWR at $\phi = 90°$; (f) Γ_a phase at $\phi = 90°$.

Table 3.2. Computational statistics of BT-POD for infinite Vivaldi array example.

Solution Method	Size	Wall Time	Peak Memory	Time Speed Up
Point-by-point Periodic TVFEM	$158,024$	$\approx$ 778 days[1]	729 MB	-
Multi-dimensional BT-POD (serial)	128	t_s=06:52:57	729 MB	$t_{FEM}/t_s = 2667.4$
Multi-dimensional BT-POD (parallel)	128	t_p=00:32:31	729 MB	$t_s/t_p = 12.7$

3.2.2 Infinite PUMA Array

This example considers the system response of the two-port PUMA infinite antenna array, shown in Figure 3.7, when frequency and two material property parameters are considered. As shown in Figure 3.7 , the antenna unit cell consists of a multi-layer structure with different relative permittivity ϵ_r values. The behavior of the antenna is quite sensitive to the dielectric properties of the substrate ϵ_{r2} and the superstrate ϵ_{r1}. In this example the operating bandwidth is 6-20 GHz, and both permitivities of the material layers vary from $\epsilon_r = 1 - 7$. The periodic TVFEM unit cell is discretized with $152,360$ second-order TVFEM unknowns. The POD expansion points used to generate the reduced-order model for the 3D parametric sweep form a tensor product in the parametric space. The total number of expansion and sweep points in each parameter-space dimension are listed in Table 3.3. The decay of normalized Hankel singular values is shown in Figure 3.8 with a HSVs truncation tolerance $\varepsilon = 7 \times 10^{-6}$, thus the size of the reduced model is 158. The results of this simulation are shown in figure 3.9 where a comparison of the active reflection coefficient of the proposed multi-dimensional BT-POD versus the point-by-point periodic TVFEM is given. The two results agree quite well over the entire space which is also

[1]Estimated.

verified by the error study in Figure 3.10. It is noted that the point-by-point simulation was performed over a 2D parameter space $(\epsilon_{r1}, \epsilon_{r2})$ with coarser discretization $(\Delta\epsilon_r = 0.4)$ on both axises. To further illustrate the versatility of the 3D parameter simulation, the active reflection coefficient versus $(\epsilon_{r1}, \epsilon_{r2})$ is plotted at frequencies $f = 10$, 14 and 20 GHz in Figure 3.11. The computational statistics from this section are listed in Table 3.4 for a $71 \times 61 \times 61$ sweep. It is being noted that the memory cost of BT-POD exceeds the point-by-point TVFEM, this is because to speed up the process of constructing transformation matrices $\mathbf{T}_L$ and $\mathbf{T}_R$, multiple columns of $\mathbf{U}$ and $\mathbf{L}$ are stored in memory. It also should be remarked that the wall time for point-by-point unit cell TVFEM simulation is only estimated, based on a 2D parametric sweep.

Table 3.3. BT-POD sampling parameters for the infinite PUMA array example.

	f	ϵ_{r1}	ϵ_{r2}
# of POD samples	10	5	5
# of sweep points	71	61	61

Table 3.4. Computational statistics of BT-POD for the infinite PUMA array.

Solution Method	Size	Wall Time	Peak Memory	Speed-up
Point-by-point Periodic-cell FEM	$152,360$	$\approx$ 214 days[1]	708 MB	-
Multi-dimensional BT-POD	158	t_s=07:15:40	1050 MB	$t_{FEM}/t_s = 708$

[1]Estimated.

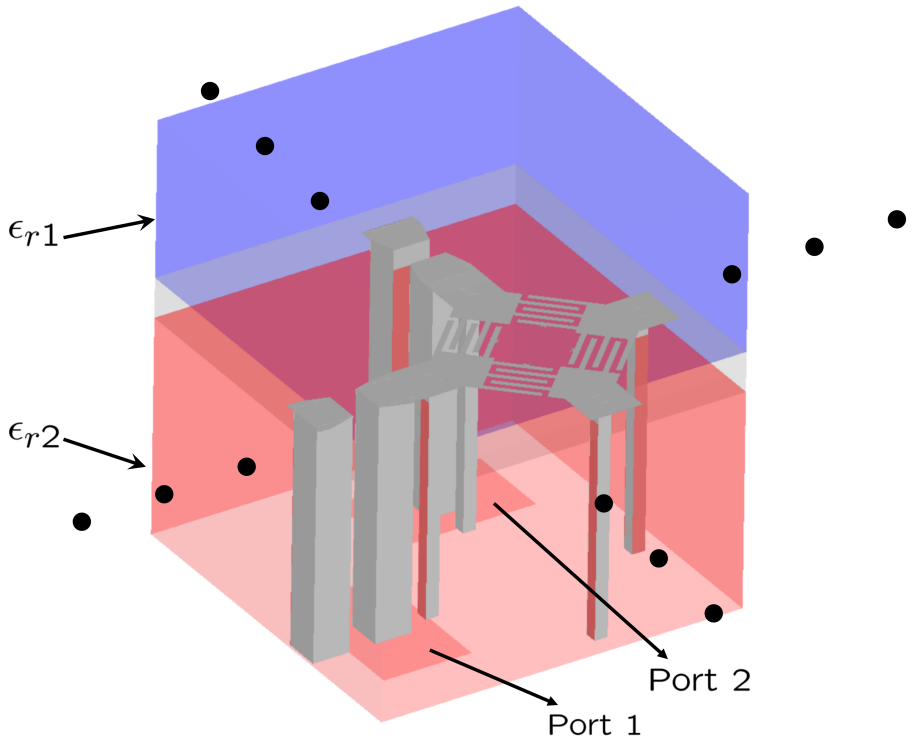

Figure 3.7. Geometry of infinite PUMA array. Material parameter ϵ_{r1} and ϵ_{r2} of the top and bottom dielectrics are used in the multi-parameter BT-POD sweep.

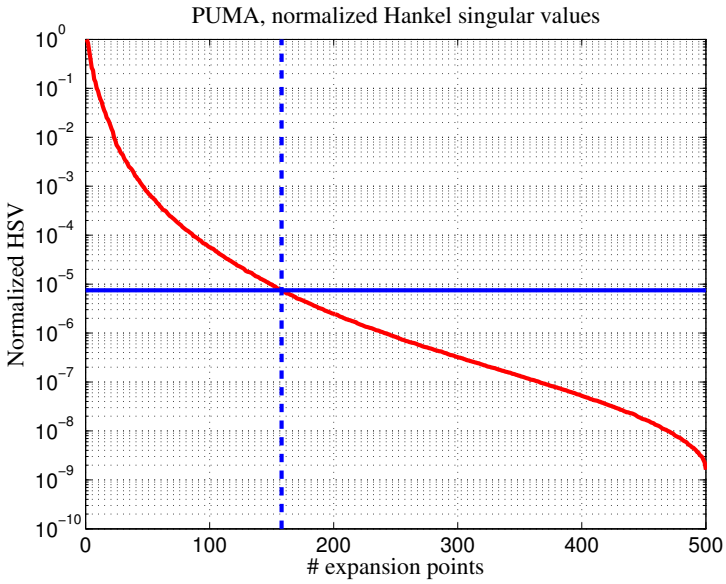

Figure 3.8. Decay of Hankel singular values for the infinite PUMA array example with HSVs truncation tolerence $\varepsilon = 7 \times 10^{-6}$.

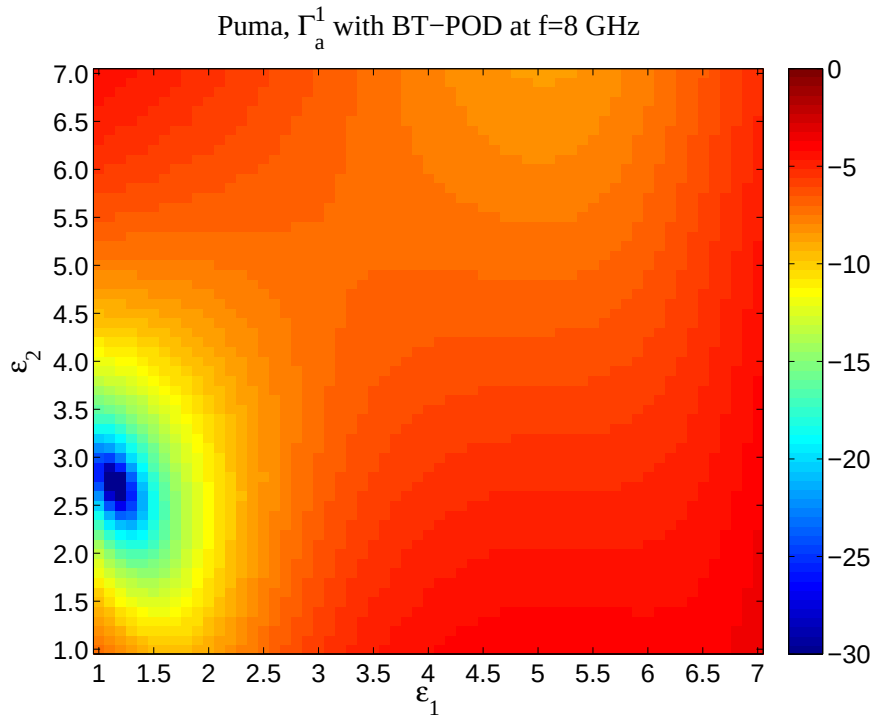

(a)

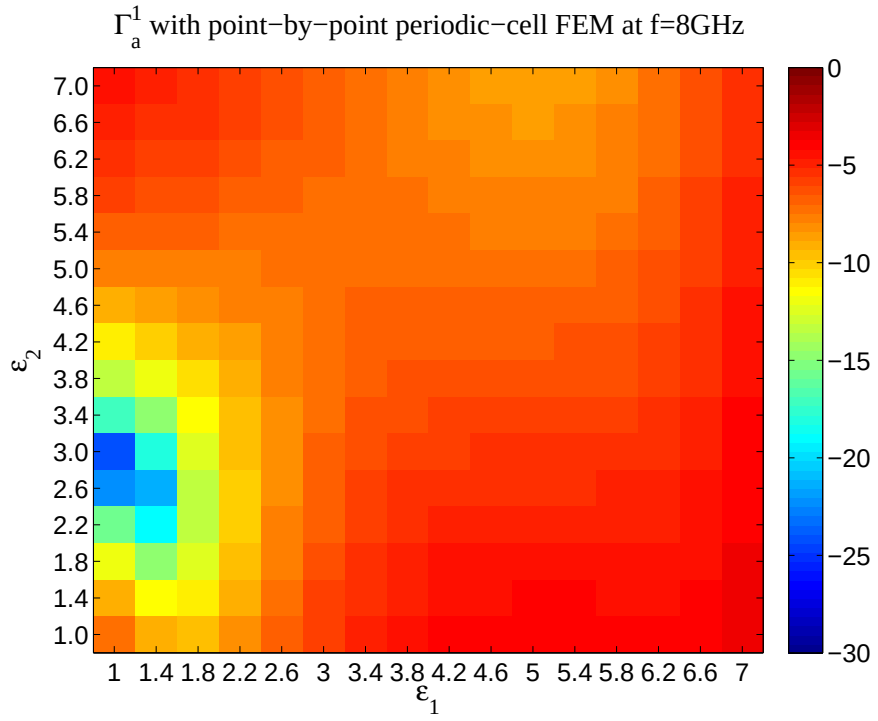

(b)

Figure 3.9. Comparison of multi-parameter BT-POD with point-by-point periodic TVFEM sweep at f=8 GHz; (a) $|\Gamma_a|$ at port 1 vs $(\epsilon_{r1}, \epsilon_{r2})$ via BT-POD; (b) $|\Gamma_a|$ at port 1 vs. $(\epsilon_{r1}, \epsilon_{r2})$ via point-by-point periodic TVFEM.

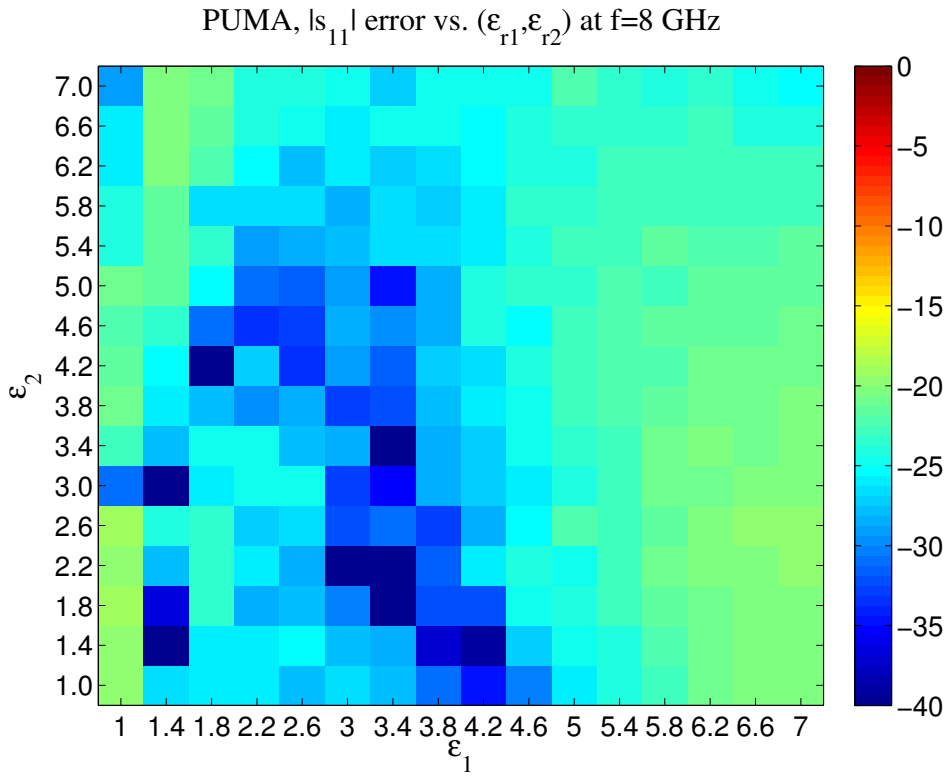

Figure 3.10. Active reflection coefficient $|\Gamma_a|$ (port 1) error [dB] vs. (ϵ_1, ϵ_2) with $\Delta\epsilon$=0.4 on both axies for the infinite PUMA array example.

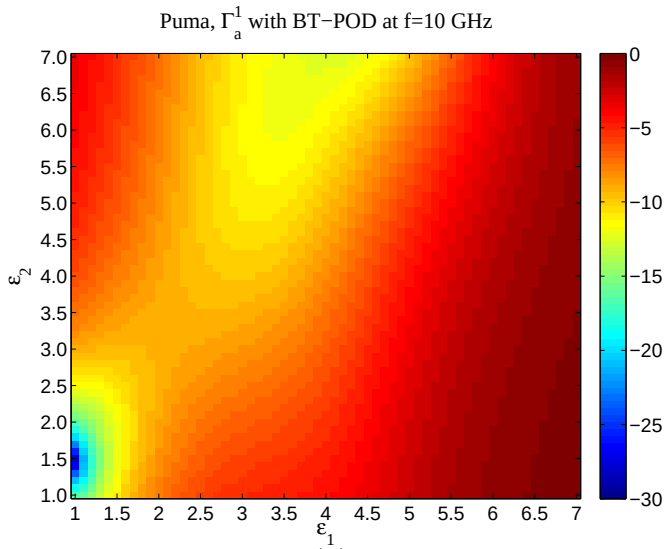

(a)

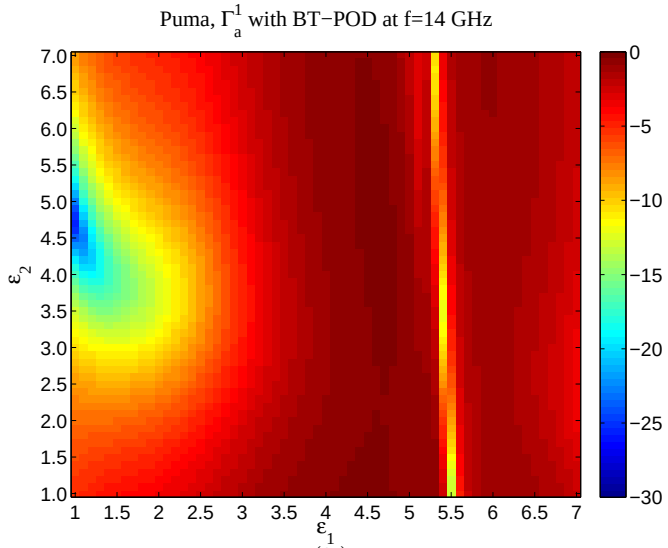

(b)

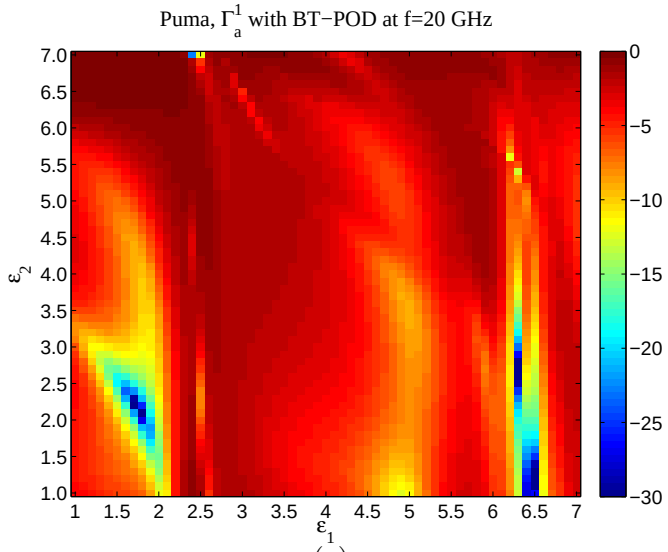

(c)

Figure 3.11. Active reflection coefficient of PUMA at various frequencies versus $(\epsilon_{r1}, \epsilon_{r2})$; (a) $f = 10$GHz; (b) $f = 14$GHz; (c) $f = 20$GHz.

CHAPTER 4

ADAPTIVE BT-POD IN FREQUENCY-DOMAIN

Up to this point, all MOR results have been produced through uniform POD sampling in the parameter space. Although uniform sampling strategies lead to obvious parallelization benefits due to the a-priori knowledge of sampling point number and location, they are less efficient and robust because sampling locations are not optimal. The aim of this chapter is to enhance the reliability and efficiency of the BT-POD algorithm through an adaptive sampling strategy. This goal will be achieved through the development of error estimates and indicators. These goal-oriented residual indicators will be used to guide the adaptive POD sampling process and terminate the iteration. In terms of selecting new frequency expansion points, the proposed approach differs from the adaptive s-parameter interpolation method [42] and adaptive multipoint method [43]. In [42], the authors proposed a simple rational polynomial interpolation model which lacks the error control. In [43], a field recovery scheme was proposed but it leads to prohibitive computations for large-scale problems. Here the goal-oriented estimates give managable size problems and lead to reliable estimates. The final result is a more stable and efficient POD sampling process that leads to more robust reduced models. Numerical results on a large-scale waveguide filter TVFEM model are used to illustrate the performance of the adaptive BT-POD algorithm.

4.1 Local and Global Error Indicators

The goal-oriented error indicators employed here are based on the residual error field reaction with wave-port modal fields, therefore give an estimate of the error on

the output quantity of interest (s-parameter in this case). This is contrary to most traditional indicators that are based on field norms (global field energy), thus they are expected to be more reliable and lead to minimal reduced models. Both local and global goal-oriented indicators will be used. Local indicators are used to find the next POD sample location, while the global indicator is used to terminate the adaptive process.

To determine the accuracy of the reduced solution, the reduced soluton vector $\tilde{\mathbf{e}}(s) = \tilde{\mathbf{A}}(s)^{-1}\,\tilde{\mathbf{f}}(s) \in \mathbb{C}^{n\times 1}$ at frequency s is recovered to full order through (2.36)

$$\tilde{\mathbf{e}}_r(s) = \mathbf{T_R}\,\tilde{\mathbf{e}}(s) \in \mathbb{C}^{N\times 1}, \tag{4.1}$$

where N is the full DoFs. If the full TVFEM system matrix at frequency s is denoted by $\mathbf{A}(s) = s^2\mathbf{M} + s\mathbf{D} + \mathbf{S}$, one can find how close $\tilde{\mathbf{e}}_r(s)$ is to $\tilde{\mathbf{e}}(s)$, the true full solution through the

$$\mathbf{r}(s) = \mathbf{b}(s) - \mathbf{A}(s)\,\tilde{\mathbf{e}}_r(s). \tag{4.2}$$

A residual functional $J(\cdot)$: $\mathbf{H}(\mathbf{div};\Omega) \rightarrow \mathbb{R}$ is used to minimize the error of system scattering parameters,

$$J(\mathbf{r}(s)) = \sum_{i=1}^{P} |\int_{A_i} \mathbf{R}(s)\cdot\mathbf{E}_i^{mode}(s)\,dr^2\,|, \quad i = 1, 2, \cdots, P, \tag{4.3}$$

where

$$\mathbf{R}(s) = \sum_{i}^{N} \mathbf{r}(s)\cdot\mathbf{w}_i,$$

where P is the total number of EM waveports, the electric modal field on ith waveport at frequency s is denoted by $\mathbf{E}_i^{mode}(s)$, A_i is the surface occupied by ith port. However,

(4.3) gives an error estimate with respect to a certain frequency point. Therefore, an error estimate over the frequency bandwidth $[s_i, s_{i+1}]$ is introduced as

$$e_i = \frac{1}{3}\left(J(\mathbf{r}(s_i)) + J(\mathbf{r}(s_i')) + J(\mathbf{r}(s_{i+1}))\right), \tag{4.4}$$

where

$$s_i' = \frac{1}{2}\left(s_i + s_{i+1}\right). \tag{4.5}$$

Such error is defined locally over frequency band $[s_i, s_{i+1}]$, thus it is local error estimate. Meanwhile, a global error estimate over the entire frequency bandwidth of interest can be determined by,

$$E = \|\mathbf{e}\|_{\ell_2} = \frac{1}{K-1}\sqrt{\sum_{i}^{K-1} |e_i|^2}, \tag{4.6}$$

where

$$\mathbf{e} = [e_1, e_2, \cdots, e_{K-1}],$$

K is the number of POD sampling points.

In the adaptive POD sampling procedure, local and global error estimates are evaluated at each adaptive pass. New frequency points, are obtained through ranking all local error indicators and selecting to sampling only at the m frequency segments with the largest estimates. Figure 4.1 briefly illustrates a situation where two new sample points (marked as black arrows) are added in one adaptive pass ($e_1 \gg e_2 \gg e_3$).

The most time consuming part in computing the error indicators is the full solution recovery of (4.1) and matrix-vertor multiplication (4.2), at all the sampling points s_i and candidate sampling points s_i'. Fortunately, the sampling number K is usually quite small ($K < 50$) the computational overhead remains reasonable.

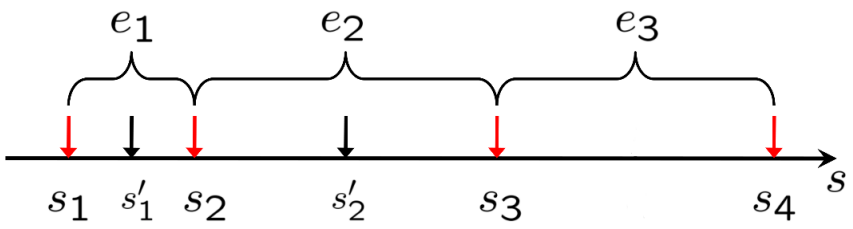

Figure 4.1. Locations of candidate freuqency points and corresponding local error indicators in adaptive BT-POD algorithm.

4.2 Adaptive Construction of Hankel Matrix

As emphasized in previous Chapters, the POD sampling process can be interpreted as a numerical quadrature over the parameter spaces. This perspective of approximating system gramians can be extended to the adaptive BT-POD algorithm, where the adaptive process leads to adaptive gramian quadratures.

The controllability gramian in s-domain is modified as

$$\mathcal{P} \approx \frac{s_{max} - s_{min}}{K\pi} \sum_{s \in \{s_1, s_2, \cdots, s_K\}} \mathbf{H}(s)\, \mathbf{H}^*(s), \tag{4.7}$$

where the sample points $\{s_1, s_2, \cdots, s_K\}$ have been computed by Algorithm 2. Figures 4.2(a)-(b) show the comparison between uniform sampling strategy and adaptive sampling strategy with the same number of sampling points.

Since at each adaptive pass, system gramians are adaptively approximated, thus the Hankel matrix, which is the cross product of the low-rank Choleski factors of system gramians, is also adaptively updated.

Assume a single-port EM device is considered, and a set of sampling frequency after a number of adaptive steps have been obtained, denoted as

$$\{s_1, s_2, \cdots, s_K\}, \tag{4.8}$$

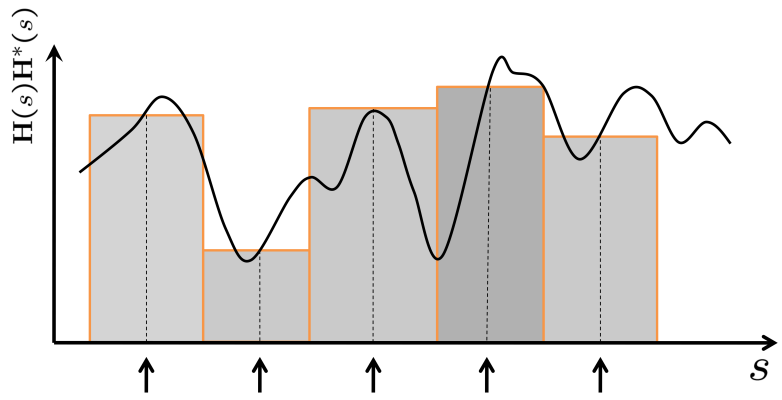

(a)

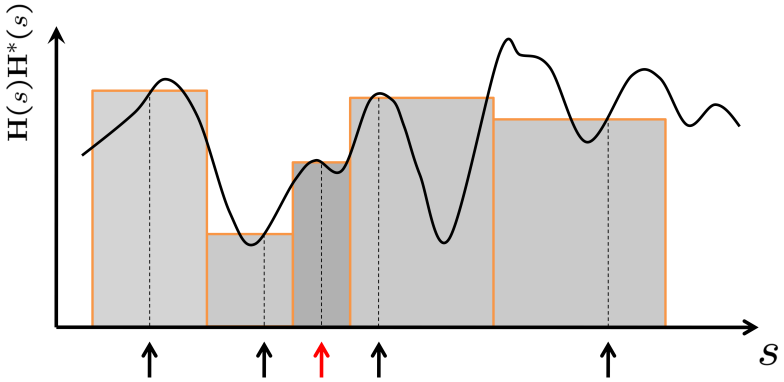

(b)

Figure 4.2. Comparison of numerical integration for system controllability gramian approximation; (a) via uniform frequency sampling; (b) via adaptive frequency sampling.

and the corresponding solution spaces through solving the forward and adjoint form of the original system are given as

$$\begin{aligned} \mathbf{U}_K = &\quad [\mathbf{H}(s_1)\ \mathbf{H}(s_2)\ \cdots\ \mathbf{H}(s_K)], \\ \mathbf{L}_K = &\quad [\mathbf{H}_a(s_1)\ \mathbf{H}_a(s_2)\ \cdots\ \mathbf{H}_a(s_K)], \end{aligned} \tag{4.9}$$

thus the Hankel matrix is constructed as

$$\boldsymbol{\mathcal{H}}_K = \mathbf{U}_K^* \mathbf{L}_K, \tag{4.10}$$

where K indicates the Hankel matrix that is obtained through performing POD sampling with K frequency points in the entire frequency band. After building the reduced-order model and the error estimation process, the error indicator identifies a new sampling point, denoted as s_{K+1}, thus the solution spaces $\mathbf{U}$ and $\mathbf{L}$ read as

$$\begin{aligned} \mathbf{U}_{K+1} = &\quad [\mathbf{H}(s_1)\ \mathbf{H}(s_2), \cdots, \mathbf{H}(s_K)\ \mathbf{H}(s_{K+1})], \\ \mathbf{L}_{K+1} = &\quad [\mathbf{H}_a(s_1)\ \mathbf{H}_a(s_2), \cdots, \mathbf{H}_a(s_K)\ \mathbf{H}_a(s_{K+1})], \end{aligned} \tag{4.11}$$

and its corresponding Hankel matrix yields as

$$\begin{aligned} \boldsymbol{\mathcal{H}}_{K+1} &= \mathbf{U}_{K+1}^* \mathbf{L}_{K+1} = [\mathbf{U}_K^*\ \mathbf{H}(s_{K+1})]\ [\mathbf{L}_K\ \mathbf{H}_a(s_{K+1})] \\ &= \begin{bmatrix} \boldsymbol{\mathcal{H}}_K & \mathbf{U}_K^*\, \mathbf{H}_a(s_{K+1}) \\ \mathbf{H}(s_{K+1})^*\, \mathbf{L}_K & \mathbf{H}(s_{K+1})^*\, \mathbf{H}_a(s_{K+1}). \end{bmatrix} \end{aligned} \tag{4.12}$$

It is noticed that the extra computation cost will only happen while dealing with the new solution vector $\mathbf{H}(s_{K+1})$ and $\mathbf{H}_a(s_{K+1})$, the added computation complexity at each adaptive step for updating the Hankel matrix is approximately $(2K+1)\cdot O(N)$.

4.3 Adaptive BT-POD Algorithm Summary

Algorithm 2 gives the summary of adaptive BT-POD approach. The general strategy goes as follows:

(1) Start with initial POD sampling frequency points that include the lowest, highest and middle point frequencies. Similar to the uniform BT-POD, the algorithm solves the full TVFEM model at these frequencies and proceeds through the truncation and reduction steps to generate an initial reduced model that will be used to find the initial error indicators.

(2) At each adaptive step, a new reduced model is re-generated using the POD samples from the frequencies with the highest error estimates. At every adaptive pass, adaptive BT-POD computes the local s-parameter error indicator e based on every interval frequency band as well as the global error indicator E along the entire freuqnecy bandwidth is computed using (4.6). Out of all these local error indicators, the m intervals with the largest errors are bisected and the newly added points are used for the next step POD sampling. The algorithm terminates when the global error at a given pass is less than a user pre-defined tolerance tol_E.

Algorithm 2 : Adaptive BT-POD MOR for TVFEM.

INPUT:
ϵ: HSVs truncation tolerance
tol_s: FEM iterative solver tolerance
tol_E: Global error residual tolerance
E: Global residual functional tolerance
s_{min} s_{max}: minimum and maximum frequency
M: sweep number

DEFINITIONS:
$s'_i = \frac{1}{2}(s_i + s_{i+1})$

1: Assemble global FEM matrices and excitation coeff. $\mathbf{M}$, $\mathbf{D}$, $\mathbf{S}$ and $\mathbf{C}$

2: Preliminary error estimate
i. POD sampling at s_1, s_2, s_3, concatenate on $\mathbf{U}$ and $\mathbf{L}$, where
$s_1 = s_{min}, s_2 = \frac{1}{2}(s_1 + s_3), s_3 = s_{max}$
ii. construct $\mathbf{H}$ matrix, perform SVD and transform matrices
$\mathbf{H} = \mathbf{U}^*\mathbf{L} = \mathbf{W}\mathbf{\Sigma}\mathbf{V}^*$, $\mathbf{T}_L = \mathbf{V}^*\mathbf{L}^*$, $\mathbf{T}_R = \mathbf{U}\mathbf{W}$
iii. reduction and solve reduced problem at
$s = \{s_1, s'_1, s_2, s'_2, s_3\}$
$\tilde{\mathbf{M}} = \mathbf{T}_L\mathbf{M}\mathbf{T}_R \quad \tilde{\mathbf{D}} = \mathbf{T}_L\mathbf{D}\mathbf{T}_R \quad \tilde{\mathbf{S}} = \mathbf{T}_L\mathbf{S}\mathbf{T}_R \quad \tilde{\mathbf{B}} = \mathbf{T}_L\mathbf{B}$
$(s_i^2\tilde{\mathbf{M}} + s_i\tilde{\mathbf{D}} + \tilde{\mathbf{S}})\tilde{\mathbf{e}} = \tilde{\mathbf{B}}\,\tilde{\mathbf{f}}_i$

3: Adaptive POD Sampling
while $E > tol_E$
i. find $\{s'_{m1}, s'_{m2}, \cdots, s'_{mm}\}$ as new frequency expansion points such that:
$\{e_{m1}, e_{m2}, \cdots, e_{mm}\} = \max_m\{e_i|, i = 1, 2, \cdots, k-1\}$
ii. update $\mathbf{U}' \leftarrow \mathbf{U}$, $\mathbf{L}' \leftarrow \mathbf{L}$, $\mathbf{H}' \leftarrow \mathbf{H}$, $k \leftarrow k + m$
iii. perform SVD on Hankel matrix and construct new transform matrices
$\mathbf{H}' = \mathbf{W}'\Sigma'\mathbf{V}'^*$, $\mathbf{T}_L = \mathbf{V}'^*\mathbf{L}'^*$, $\mathbf{T_R}' = \mathbf{U}'\mathbf{W}'$
iv. reduce system and solve reduced problem at
$s = \{s_1, s'_i, s_2, \cdots, s_{k-1}, s'_{k-1}, s_k\}$
v. compute local residual functional and global error E
$e_i = \frac{1}{3}(J(\mathbf{r}(s_i)) + J(\mathbf{r}(s'_i)) + J(\mathbf{r}(s_{i+1}))), \;\; i = 1, 2, \cdots, k-1$
end while

4: Fast Frequency Sweep
for s_m $(m = 1, 2, \cdots, M)$, solve reduced problem via a direct solver:
$(s_m^2\tilde{\mathbf{M}} + s_m\tilde{\mathbf{D}} + \tilde{\mathbf{S}})\tilde{\mathbf{e}} = \tilde{\mathbf{C}}\,\tilde{\mathbf{f}}_m \quad \{\tilde{\mathbf{M}}, \tilde{\mathbf{S}}, \tilde{\mathbf{D}}\} \in \mathbb{C}^{k\times k}, \tilde{\mathbf{B}} \in \mathbb{C}^{k\times P}$
$\tilde{\mathbf{y}} = \tilde{\mathbf{C}}^T\tilde{\mathbf{e}}$
end for

4.4 Numerical Results

In this section, a microwave waveguide filter problem is presented to validate the proposed adaptive algorithm. All computations are performed on a single Intel Pentium 4 2.4 GHz quad core processer with 4 GB RAM. The adaptive BT-POD algorithm was programmed in C++ and compiled using `gcc` 4.3.3.

The geometry of the waveguide filter under consideration is shown in Figure 4.3. The two-port device is discretized using $145,889$ tetrahedral elements and $901,640$ second-order TVFEM unknowns. The bandwidth of interest for this problem is between 7.8-9 GHz. The decay of Hankel singluar values obtained at each adaptive step is shown in Figure 4.4, the reference HSVs decay is obtained through a uniform POD sampling with 15 points (30 TVFEM solves). The important information from this plot is that 4 adaptive passes (7 samples) are capable of reproducing HSVs that closely resemble those of a much larger uniformly sampled POD. It is also worth noting that a steep drop can be observed when the sampling point number reaches above 6, and this indicates that the minimum frequency sampling number could be 7 which can be verified by the results that follow. To compare the effects of different sampling numbers, the s_{11} and s_{21} via 3 and 4 adaptive passes are shown in Figures 4.5 and 4.6, respectively. To better quantify the error and compare the adaptive versus uniform BT-POD, the $|s_{11}|$ and $|s_{21}|$ error versus frequency are plotted in Figure 4.7. It is observed that the absolute errors on $|s_{11}|$ and $|s_{21}|$ are well below -25dB with 7 adaptive sampling points over most of the frequency band, while the errors obtained through uniform POD sampling reach -5 dB. This adaptive BT-POD behavior could be explained from that fact that each adaptive pass, only the candidate frequency point with maximum corresponding error estimate is sampled. Figure 4.8 shows the error comparison between 7 adaptive sampling points and 8 uniform sampling points. It is observed that adaptive BT-POD achieves almost the same accuracy as uniform BT-POD does with 8 samples. The computational statistics for this numerical exper-

iment are summarized in Table 4.1 where an adaptive and uniform BT-POD of the same of samples number and same s-parameter error are both compared. It should be remarked that the uniform BT-POD sampling takes less time than adaptive sampling process with same number of sampling points, this is due to the extra matrix-vector multiplication in system reduction and recovery at each adaptive pass. However, to obtain the same accuracy as adaptive BT-POD algorithm, more sampling points are needed by uniform BT-POD.

Table 4.1. Computational statistics of waveguide filter by adaptive BT-POD.

Solution Method	Size	Sweep#	Wall Time	Peak Memory	Speedup
Point-by-point Periodic-cell FEM	901,640	100	5h 26m 39s	1350 MB	-
Adaptive BT-POD (7 samples)	14	100	34m 57s	1350 MB	9.34
Uniform BT-POD (8 samples)	16	100	36m 52s	1350 MB	8.86
Uniform BT-POD (7 samples)	14	100	30m 12s	1350 MB	10.81

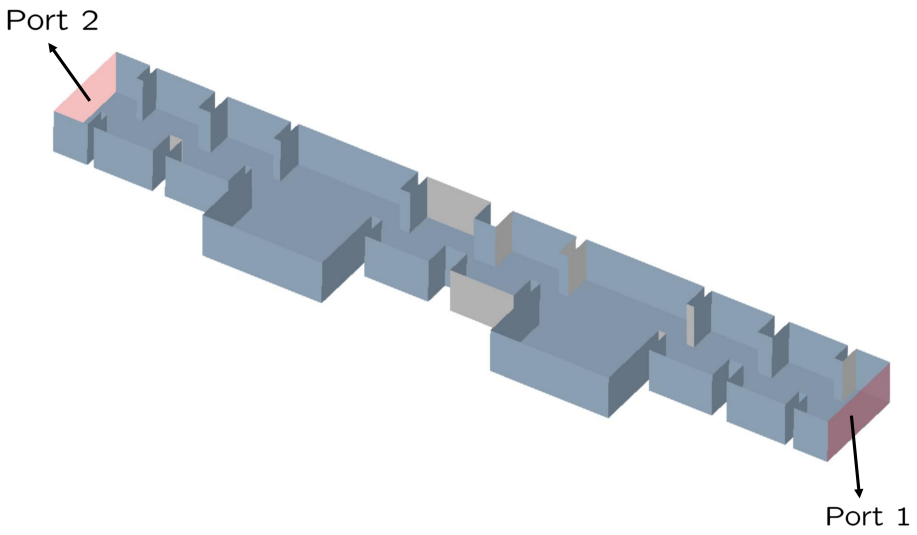

Figure 4.3. 3D geometry of microwave waveguide filter.

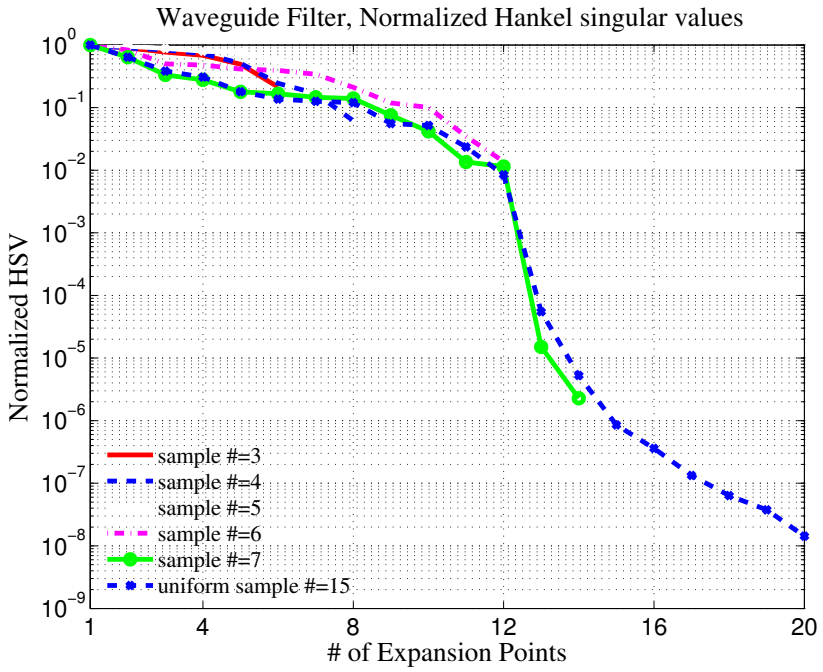

Figure 4.4. Decay of normalized Hankel singular values with various sampling number compared to normalized HSV obtained through uniform sampling with 15 points.

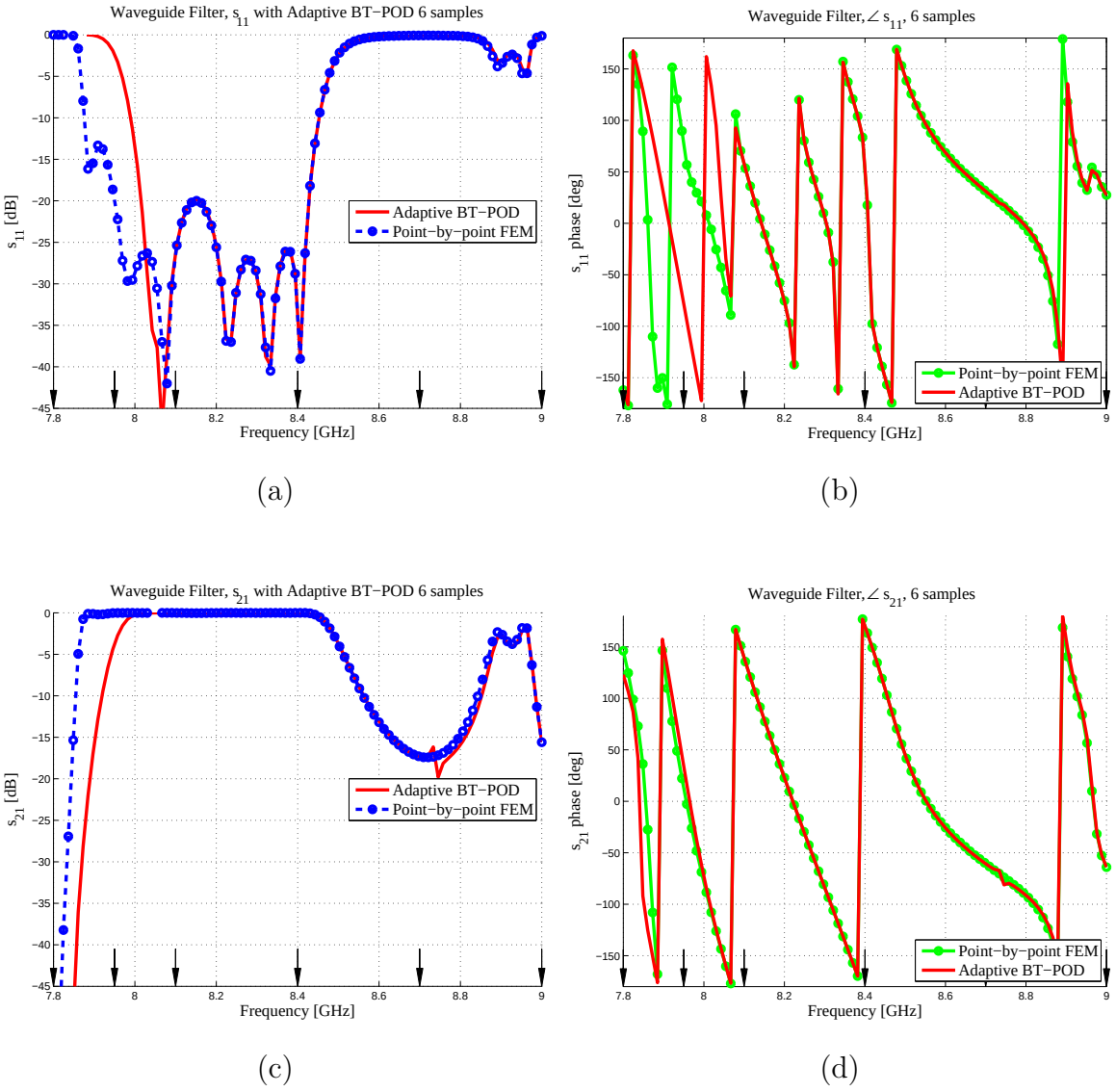

Figure 4.5. Waveguide filter with 6 non-uniform sampling points; (a) $|s_{11}|$ vs. frequency; (b) $\angle s_{11}$ vs. frequency (c) s_{21} vs frquency; (d) $\angle s_{21}$ vs. frequency.

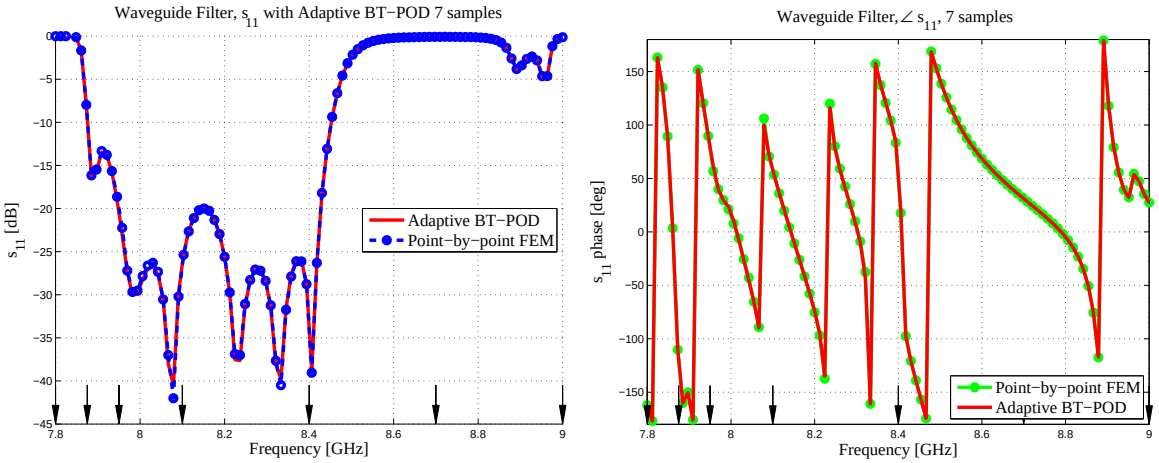

Figure 4.6. Waveguide filter with 7 non-uniform sampling points; (a) $|s_{11}|$ vs. frequency; (b) $\angle s_{11}$ vs. frequency (c) s_{21} vs frquency; (d) $\angle s_{21}$ vs. frequency.

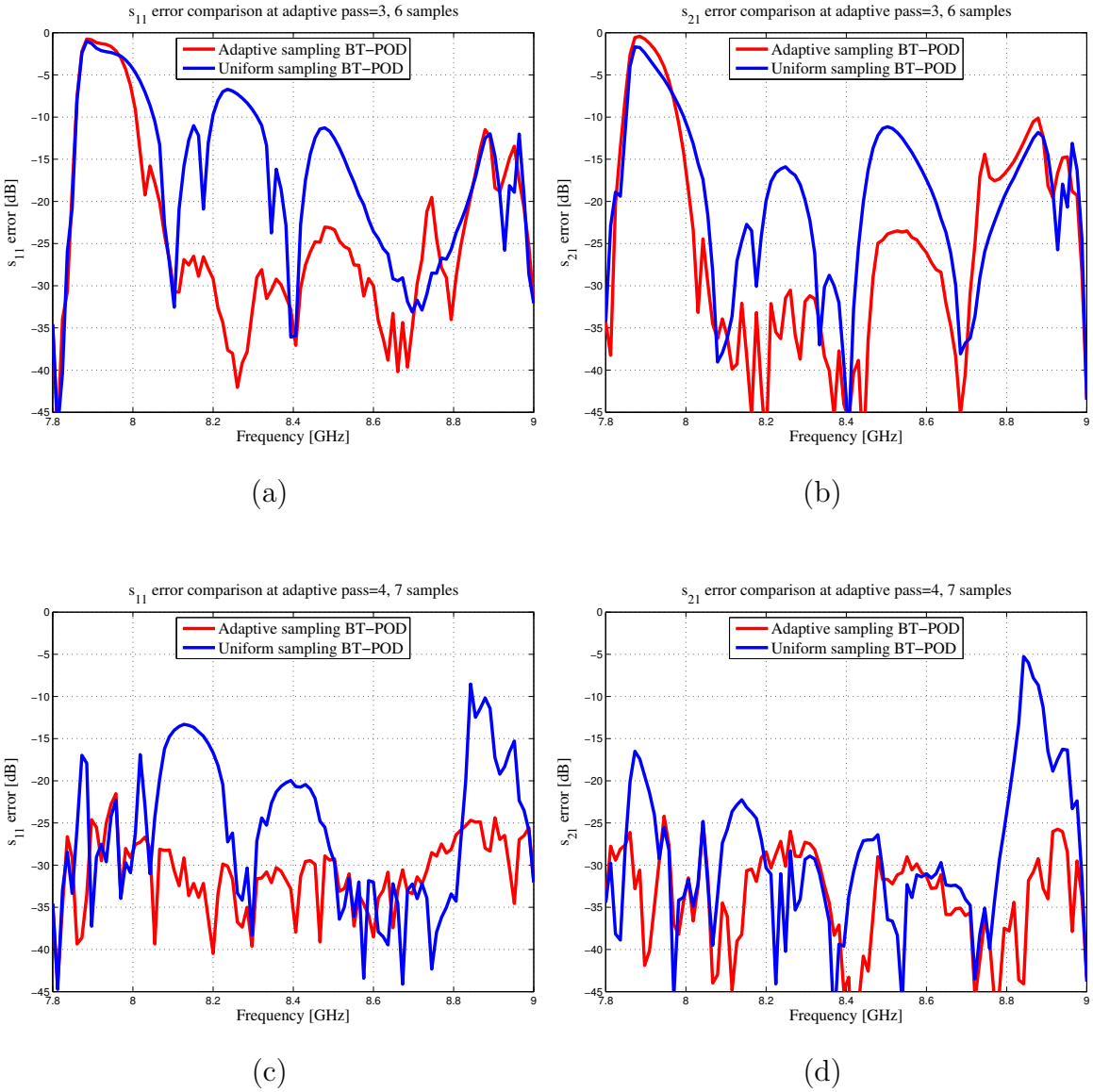

Figure 4.7. Waveguide filter s-parameter error study; (a) $|s_{11}|$ error vs. frequency at adaptive pass=3, sample#=6; (b) s_{21} error vs. frequency at adaptive pass=3, sample #=6; (c) s_{11} error vs. frquency at adaptive pass=4, sample#=7; (d) s_{21} error vs. frequency at adaptive pass=4, sample#=7.

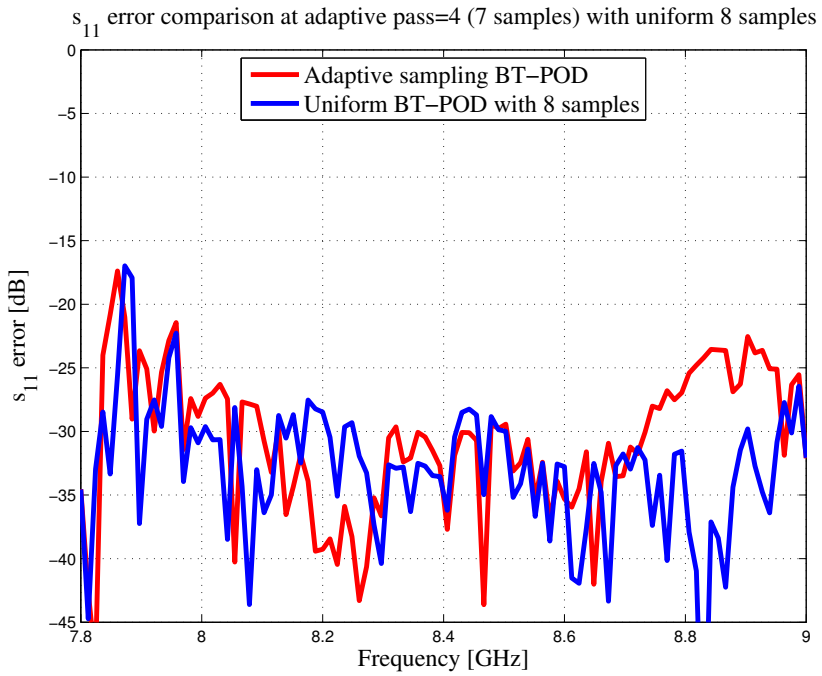

(a)

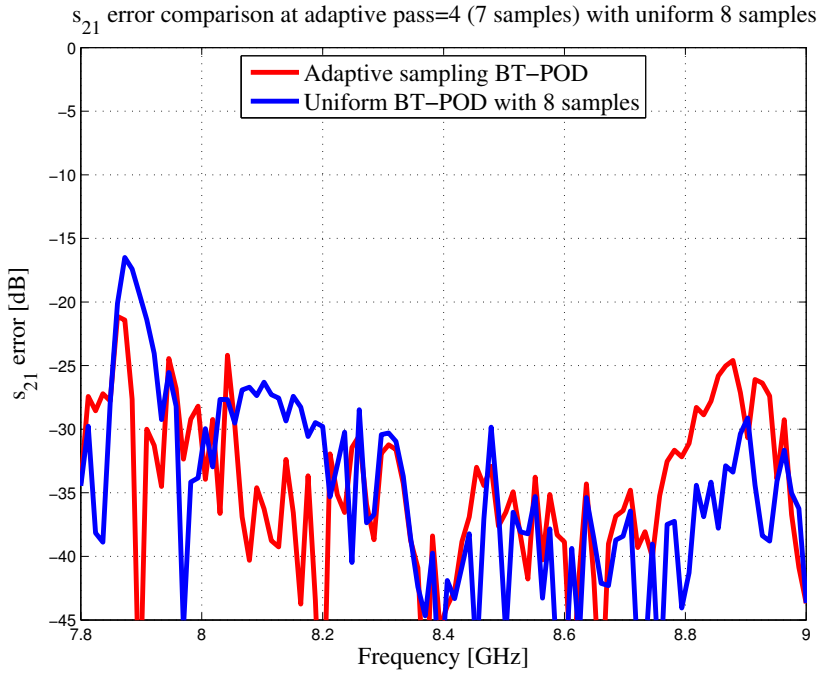

(b)

Figure 4.8. Comparison of error with adaptive BT-POD at pass 3 (7 samples) and uniform BT-POD with 8 samples; (a) $|s_{11}|$ error vs. frequency; (b) $|s_{21}|$ error vs. frequency.

CHAPTER 5

CONCLUSIONS AND FUTURE WORK

5.1 Conclusions

This work proposed an error controllable model-order reduction technique for electromagnetic systems termed balanced truncation and proper orthogonal decomposition (BT-POD). The method was developed in conjunction with the frequency-domain (time-harmonic) TVFEM wideband electromagneti systems. In addition, the method was extended to handle systems that more than one system parameters are varied. This work was limited to parameters such as excitation frequency, multiple material parameters and infinite array scan angles. A number of numerical experiments were used to demonstrate the accuracy, efficiency, robustness and versatility of the proposed method.

Although the BT-POD MOR technique involved in this research is supposed to work with first-order LTI system, it works suprisingly well with the second-order TVFEM model without introducing extra unknown variables [61]. In addition, the BT-POD successfully analyzed the three-dimensional infinite periodic structure problems that are highly dispersive systems [50] and do not comply with the LTI system theory. The BT-POD fast sweep results showed good accuracy and are controlled by the following three algorithm inputs: (1) TVFEM iterative solver tolerance; (2) POD sampling points; (3) Hankel singular values (HSVs) truncation tolerance. The CPU time savings from BT-POD is order-of-magnitude compared to the point-by-point TVFEM simulation. Even more, the parallelization speed up for the POD sampling part significantly reduces the total CPU time.

The multi-parameter space BT-POD offers an efficient and accurate algorithm for realistic system design and optimization. Numerical experiments showed quite good accuracy with -20 to -30 dB error over the entire parameter spaces. Compared to the point-by-point periodic-cell TVFEM, three or four order-of-magnitude CPU time savings were achieved. Despite the considerable speed-up from multi-dimensional BT-POD, its computational effort increases exponentially with respect to the number of parameter spaces due to the uniform POD sampling strategy used. This is a limitation present in all deterministic approximation schemes for high-dimensional sets and is often termed the "curse of dimensionality".

The proposed goal-oriented adaptive BT-POD algorithm is more efficient, robust than uniform sampling BT-POD, while on the other hand the uniform sampling BT-POD is easier and more efficient for parallelize. The proposed adaptive algorithm although shares the similar flavor with [62], it is based on goal-oriented error estimates that lead to closer to the optimal sampling. It should be noted that although the adaptive strategy takes more time than uniform POD of the same number of samples, it leads to more reliable reduced model and more accurate results.

5.2 Future Work

During the course of this thesis, a number of findings generated several research questions, that could potentially lead to promising research directions, these are:

(1) Reformulate the system gramians for the second-order LTI systems that result for realistic TVFEM model [33];

(2) Test the proposed algorithms on challenging problems such as finite antenna arrays where a much larger number of ports and DoFs are present;

(3) Explore advanced multi-dimensional integration techniques such as quasi-Monte-Carlo [59] or sparse-grid integration [60] methods to curb the complexity of MOR for high dimensional (> 6) design parameter spaces;

(4) Integrate the fast parameter-space sweep with optimization algorithms like genetic algorithm (GA) or particle swarm optimization (PSO) [63];

(5) Use the reduced TVFEM macromodel produced by BT-POD to co-simulate realistic engineering systems such as the entire RF front-end on a radar system or the signal integrity effects of mixed signal IC systems;

(6) Extend the proposed methodology to geometrical parameters (length, width) that enter into the TVFEM model as non-linear function parameters. These types of problems, although challenging, are far more useful in optimization of systems than the ones considered here.

BIBLIOGRAPHY

[1] A. van der Schaft and J. Oeloff, "Model Reduction of Linear Conservative Mechanical Systems," *IEEE Trans. Automat. Contr.*, vol. 35, pp. 729–733, Jun. 1990.

[2] A. Giua, "Model Reduction of Finite-State Machines by Contraction," *IEEE Trans. Automat. Contr.*, vol. 46, pp. 797–801, May 2001.

[3] T.-J. Su and R. R. Craig, "Model Reduction and Control of Flexible Structures Using Krylov Vectors," *Journal of Guidance, Control, and Dynamics*, vol. 14, pp. 260–267, Apr 1989.

[4] K. Willcox, *Reduced-Order Aerodynamic Models for Aeroelastic Control of Turbomachines*. PhD thesis, M.I.T., 2000.

[5] K. Willcox, "Controllability and Observability Subspaces in Computational Fluid Dynamics," in *Proceedings of the 2nd International Conference on Computational Fluid Dynamics*, (Sydney, Australia), 2002.

[6] T. Kim, "Frequency-Domain Karhunen-Loeve Method and Its Application to Linear Dynamic Systems," *AIAA Journal*, vol. 36, no. 11, pp. 2117–2123, 1998.

[7] A. Odabasioglu, M. Celik, and L. T. Pileggi, "PRIMA: Passive Reduced-Order Interconnect Macromodeling Algorithm," in *Proceedings of the 1997 IEEE/ACM international conference on Computer-aided design*, (San Jose, CA), pp. 58–65, 1997.

[8] A. Odabasioglu, M. Celik, and L. Pileggi, "Practical considerations for passive reduction of RLC circuits," in *Proceedings of the 1999 IEEE/ACM international conference on Computer-aided design*, (San Jose, CA), 1999.

[9] A. C. Cangellaris, M. Celik, S. Pasha, and L. Zhao, "Electromagnetic Model Order Reduction for System-Level Modeling," *IEEE Trans. Microw. Theory Tech.*, vol. 47, pp. 840–850, Jun. 1999.

[10] D.-K. Sun, J.-F. Lee, and Z. Cendes, "ALPS-A New Fast Frequency-sweep Procedure for Microwave Devices," *IEEE Trans. Microw. Theory Tech.*, vol. 49, pp. 398–402, Feb. 2001.

[11] B. Moore, "Principal Component Analysis in linear systems: Controllability, Observability, and Model Reduction," *IEEE Trans. Automat. Contr.*, vol. AC-26, no. 1, pp. 17–31, 1981.

[12] K. Glover, "All Optimal Hankel-norm Approximations of Linear Multivariable Systems and Their L(∞)-Error Bounds," *International Journal of Control*, vol. 39, no. 6, pp. 1115–1193, 1984.

[13] D. Kosambi, "Statistics in Function Space," *J. Indian Math. Soc.*, vol. 7, pp. 76–88, 1943.

[14] K. Pearson, "On Lines and Planes of Closest Fit to Systems of Points in Space," *Philosophical Magazine*, vol. 2, no. 6, pp. 559–572, 1901.

[15] M. Loeve, *Probability Theory*. Springer, 1977.

[16] L. Sirovich, "Turbulence and the Dynamics of Coherent Structures. Part 1: Coherent Structures," *Quarterly of Applied Mathematics*, vol. 45, no. 3, pp. 561–571, 1987.

[17] B. Feeny and R. Kappagantub, "On the Physical Interpretation of Proper Orthogonal Modes in Vibrations," *J. Sound Vibr.*, vol. 211, pp. 607–611, 1998.

[18] S. X.-D. Tan and L. He, *Adaved Model Order Reduction Techniques in VLSI Design*. Cambridge university Press, 2007.

[19] A. C. Antoulas, *Approximation of Large-Scale Dynamical System*. SIAM, 2005.

[20] "Special Issue on Order Reduction of Large-Scale Systems." Linear Algebra and its Applications, Jun. 2006. Volume 415, Issues 2-3, Pages 231-578.

[21] "Special Issue on Model-Order Reduction Methods for Computer-Aided Design of RF/Microwave and Mixed-Signal Integrated Circuits and Systems." IEEE Trans. Microw. Theory Tech., Sept. 2004. Volume 52 Issue 9.

[22] L. T. Pillage and R. A. Rohrer, "Asymptotic Waveform Evaluation for Timing Analysis," *IEEE Trans. Comput.-Aided Design Integr. Ckts Syst.*, vol. 9, pp. 352–366, Apr. 1990.

[23] P. Feldmann and R. Freund, "Efficient Linear Circuit Analysis by Pade Approximation via the Lanczos Process," *IEEE Trans. Comput.-Aided Design Integr. Ckts Syst.*, vol. 14, pp. 639–649, May 1995.

[24] Y. Saad, *Numerical Methods for Large Eigenvalue Problems*. John Wiley, 1992.

[25] W. E. Arnoldi, "The Principle of Minimized Iterations in the Solution of the Matrix Eigenvalue Problem," *Quarterly of Applied Mathematics*, vol. 9, pp. 17–29, 1951.

[26] I. M. Elfadel and D. L. Ling, "A Block Rational Arnoldi Algorithm for Multipoint Passive Model-order Reduction of Multiport RLC Networks," in *IEEE Proc. Int. Conf. Computer-Aided Design*, (San Jose, CA), Nov. 1997.

[27] T.-J. Su and R. Craig, "Model Reduction and Control of Flexible Structures using Krylov Vectors," *J. Guid. Contr. Dynm.*, vol. 14, pp. 260–267, 1991.

[28] Z. Bai and Y. Su, "SOAR: A Second-Order Arnoldi Method for the Solution of the Quadratic Eigenvalue Problem," *SIAM J. Matrix Anal. Appl.*, vol. 26, no. 3, pp. 640–659, 2005.

[29] T. Penzl, "A Cyclic Low-Rank Smith Method for Large Sparse Lyapunov Equations," *SIAM J. Sci. Comp.*, vol. 21, no. 4, pp. 1401–1418, 2000.

[30] K. Willcox and J. Peraire, "Balanced Model Reduction via the Proper Orthogonal Decomposition," *AIAA Journal*, vol. 40, pp. 2323–2330, Nov. 2002.

[31] J.-R. Li and J. White, "Low Rank Solution of Lyapunov Equations," *SIAM J. Matrix Anal. Appl.*, vol. 24, no. 1, pp. 260–280, 2002.

[32] J. Phillips and L. Silveira, "Poor Man's TBR: A Simple Model Reduction Scheme," *IEEE Trans. Comput.-Aided Design Integr. Ckts Syst.*, vol. 24, pp. 43–55, 2005.

[33] P. Losse and V. Mehrmann, "Controllability and Observability of Second Order Descriptor Systems," *SIAM J. Contr. Optim.*, vol. 47, no. 3, pp. 1351–1379, 2008.

[34] E. Miller, "Model-based Parameter Estimation in Electromagnetics. I. Backgroundand Theoretical Development," *IEEE Antennas and Propag. Magazine*, vol. 40, no. 1, pp. 42–52, 1998.

[35] E. Miller, "Model-based Parameter Estimation in Electromagnetics. II. Applications to EM Observables," *IEEE Antennas and Propag. Magazine*, vol. 40, no. 2, pp. 51–65, 1998.

[36] E. Miller, "Model-based Parameter Estimation in Electromagnetics. III. Applications to EM Integral Equations," *IEEE Antennas and Propag. Magazine*, vol. 40, no. 3, pp. 49–66, 1998.

[37] C. R. Cockrell and F. B. Beck, "Asymptotic Waveform Evaluation (AWE) Technique for Frequency Domain Electromagnetic Analysis," Tech. Rep. 110292, NASA, 1996.

[38] R. Slone, R. Lee, and J.-F. Lee, "Multipoint Galerkin Asymptotic Waveform Evaluation for Model Order Reduction of Frequency domain FEM Electromagnetic Radiation Problems," *IEEE Trans. Antennas Propag.*, vol. 49, pp. 1504–1513, Oct. 2001.

[39] R. Slone, R. Lee, and J.-F. Lee, "Well-conditioned Asymptotic Waveform Evaluation for Finite Elements," *IEEE Trans. Antennas and Propag.*, vol. 51, pp. 2442–2447, Sept. 2003.

[40] D. Weile and E. Michielssen, "Analysis of Frequency Selective Surfaces Through the Blazing Onset Using Rational Krylov Model-order Reduction and Woodbury Singularity Extraction," *IEEE Trans. Antennas Propag.*, vol. 49, pp. 1470–1478, Oct. 2001.

[41] H. Wu and A. Cangellaris, "Model-order Reduction of Finite-element Approximations of Passive Electromagnetic Devices Including Lumped Electrical-circuit Models," *IEEE Trans. Microw. Theory Tech.*, vol. 52, pp. 2305–2313, Sept. 2004.

[42] T. Dhaene, J. Ureel, N. Fache, and D. De Zutter, "Adaptive Frequency Sampling Algorithm for Fast and Accurate S-parameter Modeling of General Planar Structures," in *IEEE MTT-S Int. Microw. Symp. Digest*, pp. 1427–1430, May 1995.

[43] A. Schultschik, O. Farle, and R. Dyczij-Edlinger, "An Adaptive Multi-Point Fast Frequency Sweep for Large-Scale Finite Element Models," *IEEE Trans. Magnetics*, vol. 45, pp. 1108–1111, Mar. 2009.

[44] D. Weile and E. Michielssen, "A Method for Generating Rational Interpolant Reduced Order Models of Two-Parameter Linear System," *Applied Mathematics Letters*, vol. 12, pp. 93–102, Jan 1999.

[45] D. Weile and E. Michielssen, "Analysis of Frequency Selective Surfaces Using Two-parameter Generalized Rational Krylov Model-order Reduction," *IEEE Trans. Antennas Propag.*, vol. 49, pp. 1539–1549, Nov. 2001.

[46] O. Farle, V. Hill, P. Nickel, and R. Dyczij-Edlinger, "Multivariate Finite Element Model Order Reduction for Permittivity or Permeability Estimation," *IEEE Trans. Magnetics*, vol. 42, pp. 623–626, Apr. 2006.

[47] J. Lee, D. Sun, and Z. Cendes, "Tangential Vector Finite Elements for Electromagnetic Field Computation," *IEEE Trans. Magnetics*, vol. 27, pp. 4032–4035, Sept. 1991.

[48] J. Jin, *The Finite Element Method in Electromagnetics*. Wiley-IEEE Press, May 2002.

[49] P.-L. Lions, "On the Schwarz Alternating Method III: A Variant for Nonoverlapping Subdomains," in *Third International Symposium on Domain Decomposition Methods*, (Philadelphia, PA), SIAM, 1989.

[50] M. N. Vouvakis, K. Z. Zhao, and J.-F. Lee, "Finite-Element Analysis of Infinite Periodic Structures With Nonmatching Triangulations," *IEEE Trans. Magnetics*, vol. 42, pp. 691–694, Apr. 2006.

[51] J. Nedelec, "Mixed Finite Elements in R3," *Numer. Math.*, vol. 35, pp. 315–341, 1980.

[52] S. Lang, *Complex Analysis*. Springer, Jul. 2003.

[53] A. Chatterjee, "An Introduction to the Proper Orthogonal Decomposition," *Current Science*, vol. 78, pp. 808–817, Apr. 2000.

[54] I. T. Jolliffe, *Principal Component Analysis*. Springer, Oct. 2002.

[55] J. Lee and D. Sun, "p-Type Multiplicative Schwarz (pMUS) Method with Vector Finite Elements for Modeling Three-Dimensional Waveguide Discontinuities," *IEEE Trans on Microw. Theory Tech.*, vol. 52, no. 3, pp. 864–870, 2004.

[56] D. M. Sheen, S. M. Ali, M. D. Abouzahra, and J. A. Kong, "Application of the Three Dimensional Finite Difference Time-Domain Method to the Analysis of Planar Microstrip Circuits," *IEEE Trans. Microw. Theory and Tech.*, vol. 38, pp. 849–857, Jul. 1990.

[57] D. H. Schaubert, S. Kasturi, A. Boryssenko, and W. Elsallal, "Vivaldi Antenna Arrays for Wide Bandwidth and Electronic Scanning," in *2nd Euro. Conf. on Ant. and Prop.*, Nov. 2007.

[58] D. Schaubert and T. Chio, "Wideband Vivaldi Arrays for Large Aperture Antennas," in *Proceedings of conference at the ASTRON Institute*, pp. 49–57, Apr. 1999.

[59] W. J. Morokoff, R. E. Caflisch, and O. Numbers, "Quasi-monte carlo integration," *Journal of Computational Physics*, vol. 122, pp. 218–230, 1995.

[60] T. Gerstner and M. Griebel, "Numerical integration using sparse grids," *Numer. Algorithms*, vol. 18, pp. 209–232, 1998.

[61] M. Sampath, A. Dounavis, and R. Khazaka, "Parameterized Model Order Reduction Techniques for Finite Element Based Full Wave Analysis," in *IEEE MTT-S Int. Symp. Microw. Digest*, pp. 64–67, Jun. 2006.

[62] A. Schultschik, O. Farle, , and R. Dyczij-Edlinger, "An Adaptive Multi-Point Fast Frequency Sweep for Large-Scale Finite Element Models," *IEEE Trans. Magnetics*, vol. 45, pp. 1108–1111, Mar. 2009.

[63] Y. Rahmat-Samii, "Genetic Algorithm (GA) and Particle Swarm Optimization (PSO) in Engineering Electromagnetics," in *Applied Electromagnetics and Communications, 2003. ICECom 2003. 17th International Conference on*, pp. 1–5, Oct. 2003.